THE GREYBODY FACTOR FOR THE PROCA FIELD IN THE SPHERICALLY SYMMETRIC BLACK HOLE SPACETIMES

SUPANAT BUNJUSUWAN

A Thesis Submitted to Graduate School of Naresuan University
in Partial Fulfillment of the Requirements
for the Master of Science Program in Theoretical Physics
May 2025

Thesis entitled "The greybody factor for the Proca field in the spherically symmetric black hole spacetimes"
by Supanat Bunjusuwan
has been approved by the Graduate School as partial fulfillment of
the requirement for the Master of Science in Theoretical Physics of
Naresuan University

Oral Defense Committee

.... Chair
(Assistant Professor Supakchai Ponglertsakul, Ph.D.)

.... Advisor
(Assistant Professor Chun-Hung Chen, Ph.D.)

.... Co-Advisor
(Associate Professor Pitayuth Wongjun, Ph.D.)

.... Committee
(Associate Professor Khamphee Karwan, Ph.D.)

Approved

....
(Associate Professor Krongkarn Chootip, Ph.D.)
Dean of the Graduate School

22 MAY 2025

ACKNOWLEDGMENTS

First and foremost, I would like to express my deepest gratitude to my supervisor, Assistant Professor Chun-Hung Chen, for his continuous supportand encouragement throughout my research and the writing of this thesis. His advice has been invaluable to me.

Special thanks are extended to Associate Professor Pitayuth Wongjun for his guidance and for providing fundamental theoretical insights into black hole physics, as well as for his thoughtful advice on the development of this thesis. Sincere appreciation is also extended to Assistant Professor Supakchai Ponglertsakul for his careful review and assistance in correcting the shortcomings of this work.

I am also grateful to the faculty members at the Institute for Fundamental Study (IF), who provided me with essential knowledge and training in theoretical physics throughout my master's studies. This work would not have been possible without the academic foundation they helped me build.

Warmest thanks are extended to all my friends at IF for their camaraderie, encouragement, and support. I'm also grateful to my juniors from Silpakorn University for all the great discussions we had, which truly helped me move this thesis forward.

Lastly, I would like to thank my "Little Armadillo", my beloved cats, and my family for sharing this journey with me.

Supanat Bunjusuwan

Title	THE GREYBODY FACTOR FOR THE PROCA FIELD IN THE SPHERICALLY SYMMETRIC BLACK HOLE SPACETIMES
Author	Supanat Bunjusuwan
Advisor	Assistant Professor Chun-Hung Chen, Ph.D.
Co-Advisor	Associate Professor Pitayuth Wongjun, Ph.D.
Academic Paper	M.S. Thesis in Theoretical Physics, Naresuan University, 2024
Keywords	Black holes, Greybody factor, Proca field, Hawking radiation

ABSTRACT

In this work, we study the greybody factor for a massive spin-1 field (Proca field) in the Schwarzschild black hole spacetime. We used vector spherical harmonics (VSH) to separate angular components, and we found a one-dimensional decoupled wave equation for the odd-parity mode and three coupled equations for the even-parity mode, including the monopole modes. For the even-parity case, we apply the Frolov–Krtouš–Kubizňák–Santos (FKKS) method to decouple the equations, which separates the Proca field into the even-parity vector mode and the even-parity scalar mode. We then compute the greybody factor using the rigorous bound method and the WKB approximation. We also compare the results from these two approaches. The results indicate that among the three polarization modes of the Proca field, the even-parity vector mode has the highest transmission probability, followed by the odd-parity mode, with the even-parity scalar mode having the lowest transmission probability. Moreover, the greybody factor for the small mass limit of even-parity vector polarization presented a higher transmission probability than the Maxwell particle, which interests us and requires further studies.

LIST OF CONTENTS

Chapter Page

I INTRODUCTION 1

II THEORITICAL FRAME WORK 5

2.1 Vector and tensors in curved spacetime 5
  2.1.1 Covariant derivatives of a vector 5
  2.1.2 Curvature tensor 7
2.2 Einstein field equation 8
  2.2.1 Energy-Momentum tensor 8
  2.2.2 Derivation of the Einstein field equation 9
2.3 Black hole solution 10

III GREYBODY FACTOR FOR BLACK HOLES 14

3.1 Scattering Problems of a Potential Barrier 14
3.2 The barrier-like effective potentials in the black hole perturbation theory 17
3.3 Bounding the greybody factor 21
  3.3.1 Shabat-Zakharov systems 21
  3.3.2 Bound 23
3.4 WKB approximation 25
  3.4.1 Tunneling near the peaks of potential barries 25

IV PROCA FIELD IN CRUVED SPACE 30

4.1 Proca field in spherically symmetric black hole solution 31
4.2 The vector spherical harmonic(VSH) 33
  4.2.1 Radial equation of odd- parity 37
4.3 The even-parity mode 38
  4.3.1 Frolov–Krtouš–Kubizňák–Santos (FKKS) separation and transformation 38
  4.3.2 Radial equation from Eq. (4.39) 40
  4.3.3 Consistency of Eqs. (4.37) and (4.38) 40
  4.3.4 Reducing the radial equation 42
  4.3.5 The radial equations of even-parity scalar mode 44
  4.3.6 The radial equations of even-parity vector mode 44

LIST OF CONTENTS (CONT.)

Chapter Page

V RIGOROUS BOUND 48
  5.1 The rigorous bound for odd-parity and monopole mode 48
    5.1.1 The greybody for odd-parity mode 48
    5.1.2 The greybody factor of monopole mode 51
  5.2 The rigorous bound for even-parity. 53
    5.2.1 The even-parity scalar mode 54
    5.2.2 The even-parity vector mode 55
  5.3 Discussion of Rigorous bound 59

VI WKB APPROXIMATION 63
  6.1 WKB for the odd-parity mode and monopole mode 63
    6.1.1 WKB for the odd-parity mode 63
    6.1.2 WKB for monopole mode 66
  6.2 WKB for the even-parity mode 69
    6.2.1 WKB for even-parity scalar mode 70
    6.2.2 WKB for the even-parity vector mode 72
  6.3 Discussion of WKB approximation 76

VII DISCUSSION AND CONCLUSION 79
  7.1 Discussion 79
    7.1.1 Comparison between bound and WKB 79
  7.2 Conclusion 82

REFERENCES 86

APPENDIX 91
  APPENDIX A REPRODUCE THE RADIAL EQUATION 92

BIOGRAPHY 98

LIST OF TABLES

Table **Page**

1 Representative values of the $r_{\max}$ at which the odd-parity mode, shown for various Proca masses μ and angular momentum l. 65

2 Sample values of $r_{\max}$ for the monopole mode ($l = 0$) with different values of Proca mass μ 67

3 Values of r for varying magnitudes of the Proca mass μ as it appears in Eq. (6.9)........ 70

4 Positive real tuning points for different values of ω and Proca mass with $l = 2$......... 72

LIST OF FIGURES

Figure **Page**

1 The barrier potential well. 15
2 The potential well of function $Q(x)$ near its peak. 26
3 The effective potential of odd-parity mode when $\mu = 0.1$ and variation l. 37
4 The effective potential of odd-parity mode when $l = 1$ and variation μ. 38
5 (a). The effective potential for the even-parity scalar modes with $\omega = 0.4$, $\mu = 0.1$, and variation l. (b). The effective potential for the even-parity scalar modes with $\omega = 0.4$, $l = 1$ and variation μ. 45
6 (a). The effective potential for the even-parity vector modes with $\omega = 0.4$, $\mu = 0.1$, and variation l. (b). The effective potential for the even-vector modes with $\omega = 0.4$, $= 1$ and variation μ. 46
7 The effective potential for the even-parity vector mode with $\omega = 0.15$, $l = 1$ and variation μ. 47
8 The rigorous bound of the greybody factor for the odd-parity mode with $\mu = 0.1$ and variation l. 50
9 The effective potential of odd-parity mode compared with massless vector field case with fixed $l = 1$. 50
10 The rigorous bound of the greybody factor for the odd-parity mode with $l = 1$ and variation μ, comparison with Maxwell's case. 51
11 The effective potential of monopole mode and comparison with massive scalar with $l = 0$. 52
12 The rigorous bound of the greybody factor for monopole mode and comparison with massive scalar case. 53
13 The rigorous bound for the even-parity scalar mode, by choosing h as the non-strict bound with $l = 1$ and variation μ. 55
14 The rigorous bound for even-parity scalar mode, by choosing h be the strict bound. 56
15 The greybody factor for even-parity vector by chose non-strict bound. The solid lines represent cases where the graph shifts to the left as the mass increases, while the dashed lines indicate that as the mass increases, the graph shifts to the right. 57
16 The rigorous bound for even-parity vector mode, by choosing h as the strict bound. 59
17 The compare of each mode by using rigorous non-strict bound. 60
18 compares the even-parity vector and scalar modes using the strict bound with l=2 and variation of μ. 60
19 Compares the strict-bound and non-strict bound with $l = 2$ and variation of μ. 62
20 The greybody factor for odd-parity with μ=0.1 and change l. 66
21 The greybody factor for odd-parity with $l = 1$ and variation of μ. 66
22 The effective potential of monopole mode and show the real value of r maximum of the peak. 68

LIST OF FIGURES (CONT.)

Figure **Page**

23 The greybody factor for monopole mode as variation of μ. 68

24 The greybody factor for even-parity scalar with $l = 1$ for various Proca mass. 71

25 The greybody factor for even-parity scalar with $\mu = 1$ for various l. 71

26 The greybody factor for even-parity vector mode with $\mu = 0.1$ to 0.5 with l=2. 73

27 The WKB for greybody factor of even-parity vector mode with $l = 1$ and $l = 2$, where the graph shifts to the left as the mass increases, while the dashed lines indicate that as the mass increases, the graph shifts to the right. 74

28 The WKB for greybody factor of even-parity vector mode with $l = 5$ and $l = 10$, where the graph shifts to the left as the mass increases, while the dashed lines indicate that as the mass increases, the graph shifts to the right. 75

29 Comparison of the greybody factors for various modes at $l = 1$ and varying μ. 76

30 Compare even-parity scalar of Proca field with massive scalar with $l = 1$ and varying μ. 77

31 A comparison between the WKB and rigorous bound for odd-parity mode when $l = 2$. The dashed lines represent the result of the WKB approximation, and the solid lines represent the result of the rigorous bound. 80

32 A comparison between the WKB and rigorous bound for even-parity scalar mode when $l = 2$. The dashed lines represent the result of the WKB approximation, the dotted lines represent the result of non-strict bound, and the solid lines represent the result of strict bound. 81

33 a comparison between the WKB and rigorous bound for even-parity vector mode when $l = 2$. The dashed lines represent the result of the WKB approximation, and the solid lines represent the result of the rigorous bound. 82

CHAPTER I

INTRODUCTION

After Albert Einstein formulated the Einstein field equation within his theory of General Relativity in 1915, Karl Schwarzschild discovered the first non-trivial solution to Einstein's field equations [1]. This solution describes the spacetime geometry around a spherically symmetric, non-rotating, and static black hole. This solution is important because it shows how spacetime curved around a massive compact object in the universe, this solution has become the foundation for the theory of black hole physics. After the Schwarzschild solution was discovered, it was extended to include a spherically symmetric black hole with an electric charge. This new solution, which solves the Einstein-Maxwell equations, is now called the Reissner-Nordström solution [2]. In 1963, Roy Patrick Kerr made an important discovery and derived the solution of a rotational black hole [3]. Tt was further extended to include both charge and rotational parameters, which is called the Kerr-Newman solution [4].

In 1957, Tullio Regge and John A. Wheeler conducted a powerful study in perturbation theory, focusing on the dynamics of the Schwarzschild black holes under a small perturbation. Their work is presented in a paper named "Stability of a Schwarzschild Singularity" [5], which introduced a mathematical formalism for first-order perturbation $h_{\mu\nu}$ of the Schwarzschild metric. Their approach began with the separation of variables, expressing each perturbed component of the metric as a product of a spherical harmonic function. This work led to a single ordinary second-order differential equation, which became widely known as the Regge-Wheeler equation.

In 1975, Stephen Hawking introduced the concept of Hawking radiation [6], which explains that black holes are not entirely black but possibly to emit a kind of radiation due to quantum effects near their event horizon. This radiation arises from a pair of particles created near the event horizon, where one particle escapes as radiation, traveling as an outgoing wave and another one falls into the black hole, The spectrum of Hawking radiation is influenced by the surrounding fields through which particles scatter in the vicinity of the black hole. The greybody factor quantifies the possibility of the emitted radiation, as such computing the greybody factor is crucial to accurately understanding and interpreting the observable Hawking radiation spectrum from black holes. Thus, the greybody can also be interpreted as the transmission probability of Hawking radiation.

In this work, we are interested in the greybody factor of the Proca field in the Schwarzschild black hole spacetime. The Proca field describes the behavior of a massive spin-1 particle, one can add the "mass term" to the Lagrangian of the Maxwell field to obtain the Proca equation. The presence of mass breaks gauge invariance explicitly. This leads to three degrees of freedom instead of two, and results in field equations that are no longer invariant under the usual gauge transformations. The perturbations of the massive vector field around the Schwarzschild, the Schwarzschild-de Sitter, and the Schwarzschild-anti-de Sitter black holes were considered by R. A. Konoplya in 2006 [7]. This paper derived the equations of motion for massive vector fields in the Schwarzschild background, and further extended to the Schwarzschild-like spacetimes, they derived the quasinormal spectrum of a massive vector field in such black hole spacetimes. In 2011, a study on the propagation of Hawking radiation for the Proca field in the context of the general dimensional Schwarzschild black holes was conducted by Carlos Herdeiro and Marco O. P. Sampaio, and Mengjie Wang [8]. Due to the mass term of the Proca field, the separated master equations include a coupling between two physical degrees of freedom. The authors numerically solved the resulting system of the separated ordinary differential equations (ODEs) without decoupling individual degrees of freedom. In 2012 [9], João G. Rosa and Sam R. Dolan derived the equations of motion for the massive spin-1 fields in the Schwarzschild black hole spacetime by rewriting the vector potential with a new form of the linear combination of the vector spherical harmonics (VSH). They computed the result of both quasinormal modes and quasibound states by using numerical techniques. In 2018, a new separation method by Frolov–Krtouš–Kubizňák–Santos successfully decoupled the equations of motion for the Proca fields in general dimensional Kerr-like spacetimes [10, 11], which provides researchers to study the coupled degrees of freedom in the static limit of Kerr-like spacetimes. Therefore, the massive vector field perturbations to the spherically symmetric black hole spacetimes have received some attention for the analytical studies as presented in [12, 13]. It is worth noting that most of the previous literature focuses on the quasi-normal mode rather than the greybody factor.

The greybody factor is another famous result of the black hole perturbation theory, which describes the probability of the particle with a given energy transmitting into the spatial infinity. This assumption is analogous to the quantum tunneling effect in the quantum mechanic. In particular, the black hole greybody factor describes the phenomena of the radiative waves emitted by the black hole spacetimes, which have been studied further in various types of black hole solutions.

In the study of greybody factor, there are several techniques to compute the greybody factor for various black hole solutions. In this thesis, we imposed the rigorous bound [14] and the third-order Wentzel-Kramers-Brillouin (WKB) approximation [15, 16] for the semi-analytical studies. The rigorous bound is based on a mathematical approach for studying the greybody factors without solving the full wave equation. Instead, it provides lower limits for the greybody factor, which ensures the actual value is within a specific range. Further evaluations can be found in the following literature [17, 18, 19, 20, 21, 22]. The WKB approximation provides sufficient studies in black hole perturbation theory, and the higher order corrections were presented in [23, 24, 25]. Nevertheless, the conclusion of these articles presented that the fundamental WKB provides sufficiently accurate results when compared to the higher-order one. Therefore, we follow the third-order formula in this thesis because of the complicated mathematical form of our even-parity polarizations, which will be presented in the later chapters.

This thesis is organized as follows. In Ch. 2, we summarize the fundamental knowledge of general relativity. We review the basic knowledge of the quantum scattering in Ch. 3, where, we show how to determine the transmission and reflection probabilities when a particle encounters a barrier potential in Ch. 3.1. Additionally, we provide an example of deriving the radial equation and effective potential for the Klein-Gordon equation in Schwarzschild spacetime, which provides the idea of analogizing the black hole perturbation to the quantum tunnel problem in Ch. 3.2. In Ch. 3.3 and Ch. 3.4, we introduce two approaches to investigating the greybody factor, which are the rigorous bound method and the WKB approximation. In Ch. 4.1 and Ch. 4.2, we present the separable formulation of the Proca field equation in Schwarzschild spacetime by using the ansatz of vector potential, expressed as a linear combination of vector spherical harmonics (VSH). We then derive the radial equation for the Proca field in this background. In Ch. 4.3, we introduce the Frolov–Krtouš–Kubizňák–Santos (FKKS) method to reduce the coupled radial equations and present the effective potential for each mode. We present the result of our investigation of the greybody factor by using Rigorous bound and WKB in Ch. 5 and Ch. 6 respectively. Some of the results presented in Ch. 5, including the odd-parity and monopole modes, were published in the conference proceedings of the Siam Physics Congress 2023 [22]. Lastly, we provide a discussion and conclusion regarding the greybody factor of the Proca field in Schwarzschild spacetime in Ch. 7.

CHAPTER II

THEORITICAL FRAME WORK

In this chapter, we introduce the fundamental background knowledge of Einstein's General relativity. We start with the covariant derivative, write down the Christoffel symbol, Riemann curvature tensor, Ricci tensor, and present the Einstein field equation. In the last section of this chapter, we introduce the Schwarzschild solution, which is the black hole spacetime that we mainly focus on throughout this thesis.

2.1 Vector and tensors in curved spacetime

2.1.1 Covariant derivatives of a vector

Suppose that a vector field $\mathbf{V}(x)$ can be defined over some region of a manifold and consider the partial derivative of a vector field $\mathbf{V}(x) = V^{\mu}e_{\mu}$. We thus obtain

$$\partial_{\nu}\mathbf{V} = \left(\partial_{\nu}V^{\mu}\right)e_{\mu} + V^{\mu}\left(\partial_{\nu}e_{\mu}\right). \tag{2.1}$$

We may write the covariant derivative of a vector field $\mathbf{V}(x)$ as

$$\begin{aligned} \partial_{\nu}\mathbf{V} &= \left(\partial_{\nu}V^{\mu}\right)e_{\mu} + V^{\mu}\Gamma^{\gamma}{}_{\mu\nu}e_{\gamma}, && (2.2)\\ &= \left(\partial_{\nu}V^{\mu} + V^{\gamma}\Gamma^{\mu}{}_{\gamma\nu}\right)e_{\mu}, && (2.3) \end{aligned}$$

where $\Gamma^{\gamma}{}_{\mu\nu}$ is the connection. The quantity in brackets is called the covariant derivative of the vector components, we define

$$\nabla_{\nu}V^{\mu} \equiv \partial_{\nu}V^{\mu} + \Gamma^{\nu}{}_{\gamma\mu}V^{\gamma}. \tag{2.4}$$

The covariant derivative of a scalar function is the ordinary derivative, which means

$$\partial_{\mu}\phi = \nabla_{\mu}\phi = \nabla_{\mu}\left(A_{\nu}B^{\nu}\right). \tag{2.5}$$

Replacing the covariant derivative part with Eq.(2.4), we may obtain the contravariant derivative as

$$\nabla_\nu V_\mu \;=\; \partial_\nu V_\mu - \Gamma^\gamma{}_{\mu\nu} V_\gamma. \tag{2.6}$$

Furthermore, we may introduce the torsionless condition and the matric compatibility as

$$\Gamma^\gamma{}_{\mu\nu} = \Gamma^\gamma{}_{\nu\mu}, \tag{2.7}$$

$$\nabla_\mu g_{\nu\rho} = 0, \tag{2.8}$$

and the differentiation to the metric tensor $g_{\mu\nu}$ can be obtained

$$\partial_\rho g_{\mu\nu} \;=\; \Gamma^\gamma{}_{\mu\rho} g_{\gamma\nu} + \Gamma^\gamma{}_{\nu\rho} g_{\mu\gamma}. \tag{2.9}$$

$$\partial_\nu g_{\rho\mu} \;=\; \Gamma^\gamma{}_{\rho\nu} g_{\gamma\mu} + \Gamma^\gamma{}_{\mu\nu} g_{\rho\gamma}, \tag{2.10}$$

$$\partial_\mu g_{\nu\rho} \;=\; \Gamma^\gamma{}_{\nu\mu} g_{\gamma\rho} + \Gamma^\gamma{}_{\rho\mu} g_{\nu\gamma}. \tag{2.11}$$

Using these three expressions, we now form the combination

$$\partial_\rho g_{\mu\nu} + \partial_\nu g_{\rho\mu} - \partial_\mu g_{\nu\rho} = 2\Gamma^\gamma{}_{\rho\nu} g_{\mu\gamma}. \tag{2.12}$$

Now, we finally obtain

$$\Gamma^\lambda{}_{\rho\nu} = \frac{1}{2} g^{\mu\lambda} \left(\partial_\rho g_{\mu\nu} + \partial_\nu g_{\rho\mu} - \partial_\mu g_{\nu\rho}\right) \tag{2.13}$$

This connection is called Christoffel symbols. Note that the connection $\Gamma^\mu{}_{\nu\rho}$ does not transform as the components of a tensor.

2.1.2 Curvature tensor

Considering the commutator of two covariant derivatives of a vector field V^ρ, we obtain

$$\begin{aligned}
[\nabla_\mu, \nabla_\nu]V^\rho &= \nabla_\mu\nabla_\nu V^\rho - \nabla_\nu\nabla_\mu V^\rho, \\
&= \partial_\mu\partial_\nu V^\rho + \left(\partial_\mu \Gamma^\rho{}_{\nu\sigma}\right) V^\sigma + \Gamma^\rho{}_{\nu\sigma}\partial_\mu V^\sigma - \Gamma^\lambda{}_{\mu\nu}\partial_\lambda V^\rho - \Gamma^\lambda{}_{\mu\nu}\Gamma^\rho{}_{\lambda\sigma}V^\sigma \\
&\quad + \Gamma^\rho{}_{\mu\sigma}\partial_\nu V^\sigma + \Gamma^\rho{}_{\mu\sigma}\Gamma^\sigma{}_{\nu\lambda}V^\lambda - (\mu \leftrightarrow \nu), \\
&= \left(\partial_\mu \Gamma^\rho{}_{\nu\sigma} - \partial_\nu \Gamma^\rho{}_{\mu\sigma} + \Gamma^\rho{}_{\mu\lambda}\Gamma^\lambda{}_{\nu\sigma} - \Gamma^\rho{}_{\nu\lambda}\Gamma^\lambda_{\mu\sigma}\right) V^\sigma - 2\Gamma^\lambda_{[\mu\nu]}\nabla_\lambda V^\rho.
\end{aligned} \tag{2.14}$$

We assume that our manifolds are torsionless as in Eq(2.7). Then, we may define the Riemann curvature tensor as

$$R^\rho{}_{\sigma\mu\nu} = \partial_\mu \Gamma^\rho{}_{\nu\sigma} - \partial_\nu \Gamma^\rho{}_{\mu\sigma} + \Gamma^\rho{}_{\mu\lambda}\Gamma^\lambda{}_{\nu\sigma} - \Gamma^\rho{}_{\nu\lambda}\Gamma^\lambda{}_{\mu\sigma}. \tag{2.15}$$

2.1.2.1 Properties of the Riemann tensor.

The Riemann tensor has four indices and describes the curvature of spacetime. To better analyze its symmetry properties, we express it with all indices in the lower (covariant) position. This is done by using the metric tensor to lower the upper index through contraction

$$R_{\rho\sigma\mu\nu} = g_{\rho\lambda}R^\lambda{}_{\sigma\mu\nu}. \tag{2.16}$$

The symmetry properties of the Riemann tensor can be written as, antisymmetric for the first two indices

$$R_{\rho\sigma\mu\nu} = -R_{\sigma\rho\mu\nu}, \tag{2.17}$$

and for the last two indices

$$R_{\rho\sigma\mu\nu} = -R_{\rho\sigma\nu\mu}. \tag{2.18}$$

It is symmetric under the interchange of the first pair of indices with the second pair

$$R_{\rho\sigma\mu\nu} = R_{\mu\nu\rho\sigma}. \tag{2.19}$$

Furthermore, the sum of the cyclic permutation of the last three indices vanishes

$$R_{\rho\sigma\mu\nu} + R_{\rho\sigma\mu\nu} + R_{\rho\sigma\mu\nu} = 0, \tag{2.20}$$

and the Bianchi identity is given by

$$\nabla_{[\lambda} R_{\rho\sigma]\mu\nu} = 0. \tag{2.21}$$

Next, the self-contraction for the first and third indies of the Riemann tensor defines of the Ricci tensor.

$$R^{\lambda}{}_{\mu\lambda\nu} = R_{\mu\nu}. \tag{2.22}$$

Obviously, with the torsionless Christoffel symbols and Eq.(2.18), the Ricci tensor is automatically symmetric

$$R_{\mu\nu} \equiv R_{\nu\mu}, \tag{2.23}$$

Lastly, the self-contraction of the Ricci tensor gives the Ricci scalar

$$R = R^{\mu}_{\mu} = g^{\mu\nu} R_{\nu\mu}. \tag{2.24}$$

2.2 Einstein field equation

2.2.1 Energy-Momentum tensor

The Einstein field equation describes the relationship between matter and spacetime curvature. The spacetime becomes flat when the matter is absent, hence, the Einstein field equation is reduced to Newtonian gravity in this limit.

The gravitational field in the Newtonian limit comes from the distribution of matter ρ in the considered area, which gives rise to the gravitational potential ϕ if the matter density increases. The relation between the gravitational potential and matter density can be described by the Poisson's equation

$$\nabla^2\phi = 4\pi G\rho, \tag{2.25}$$

where G is Newton's constant.

The energy-momentum tensor describes the distribution of matter and energy in spacetime. As an example of a perfect-fluid source, the energy-momentum can be written in the form

$$T_{\mu\nu} = (\rho + p)\, U_\mu U_\nu + p g_{\mu\nu}, \tag{2.26}$$

where U^μ is the fluid four-velocity, ρ is matter density in Eq.(2.25) and p is pressure of the fluid. In the rest frame, the four-velocity may write as

$$U^\mu = \left(U^0, 0, 0, 0\right). \tag{2.27}$$

The law of energy-momentum conservation in flat spacetime is given by

$$\partial_\mu T^{\mu\nu} = 0, \tag{2.28}$$

therefore, one appropriate generalization to curved spacetime is given by

$$\nabla_\mu T^{\mu\nu} = 0. \tag{2.29}$$

2.2.2 Derivation of the Einstein field equation

As described in the previous subsection, we discussed the energy-momentum tensor. This tensor describes the distribution of matter. As such, we need a rank-two tensor to describe gravity on the other side of the equation. The equation can be written as follows

$$R_{\mu\nu} \sim \kappa T_{\mu\nu}, \tag{2.30}$$

where κ is constant. As we discussed in Eq. (2.29), the energy-momentum tensor satisfies the conservation law, but the Ricci tensor does not satisfy it in general.

Hence, we must replace the Ricci tensor with another tensor that satisfies the conservation law.

By considering Bianchi identity of Riemann tensor, we obtain

$$\begin{aligned} g^{\nu\sigma}g^{\mu\lambda}\left(\nabla_\lambda R_{\rho\sigma\mu\nu} + \nabla_\rho R_{\sigma\lambda\mu\nu} + \nabla_\sigma R_{\lambda\rho\mu\nu}\right) &= 0, \\ \nabla^\mu R_{\rho\mu} - \nabla_\rho R + \nabla^\nu R_{\rho\nu} &= 0. \end{aligned} \tag{2.31}$$

Thus, we get

$$\nabla^\mu R_{\rho\mu} = \frac{1}{2}\nabla_\rho R. \tag{2.32}$$

Then we can define a new quantity

$$G_{\mu\nu} \equiv R_{\mu\nu} - \frac{1}{2}Rg_{\mu\nu}, \tag{2.33}$$

where $G_{\mu\nu}$ is named as Einstein tensor and satisfies the conservation law

$$\nabla^\mu G_{\mu\nu} = 0. \tag{2.34}$$

Together with Eq.(2.29) , Eq.(2.30) and Eq.(2.34), we have

$$G_{\mu\nu} = \kappa T_{\mu\nu}. \tag{2.35}$$

In the Newtonian limit, we can find the constant κ by comparing with the Possion equation in Eq.(2.25), and Einstein's equation can be obtained

$$G_{\mu\nu} = 8\pi G T_{\mu\nu}. \tag{2.36}$$

2.3 Black hole solution

As described in the previous section, Einstein's equation explains the relationship between matter and spacetime curvature. Since this equation is non-linear, we should impose some assumptions to solve an exact solution. In 1916, Karl Schwarzschild found the first solution to Einstein's equation by assuming that spacetime is empty, stationary, and spherically symmetric.

To impose spherical symmetry, we will write the metric of spacetime in spherical coordinate $x^\mu = (t, r, \theta, \phi)$. In this coordinate, the metric can be written in terms of exponential functions, which means

$$ds^2 = -e^{2\alpha(r)}dt^2 + e^{2\beta(r)}dr^2 + r^2\left(d\theta^2 + \sin^2\theta d\phi^2\right). \tag{2.37}$$

We can compute the non-vanishing components of the Christoffel symbol as

$$\begin{aligned}
&\Gamma^t{}_{tr} = \Gamma^t{}_{rt} = \partial_r\alpha, && \Gamma^r{}_{rr} = \partial_r\beta, && \Gamma^r{}_{tt} = e^{2(\alpha-\beta)}\partial_r\alpha,\\
&\Gamma^r{}_{\theta\theta} = -re^{-2\beta}, && \Gamma^\theta{}_{r\theta} = \Gamma^\theta{}_{\theta r} = \frac{1}{r}, && \Gamma^r{}_{\phi\phi} = -re^{-2\beta}\sin^2\theta,\\
&\Gamma^\phi{}_{\theta\phi} = \Gamma^\phi{}_{\phi\theta} = \cot\theta, && \Gamma^\theta{}_{\phi\phi} = -\sin\theta\cos\theta, && \Gamma^\phi{}_{r\phi} = \Gamma^\phi{}_{\phi r} = \frac{1}{r}.
\end{aligned} \tag{2.38}$$

From the Christoffel symbol in Eq.(2.38), we get the following non-vanishing components of the Riemann tensor

$$\begin{aligned}
R^t{}_{rtr} &= \partial_r\alpha\partial_r\beta - \partial_r^2\alpha - (\partial_r\alpha)^2,\\
R^t{}_{\theta t\theta} &= -re^{-2\beta}\partial_r\alpha,\\
R^t{}_{\phi t\phi} &= -re^{-2\beta}\sin^2\theta\partial_r\alpha,\\
R^r{}_{\theta r\theta} &= re^{-2\beta}\partial_r\beta,\\
R^r{}_{\phi r\phi} &= re^{-2\beta}\sin^2\theta\partial_r\beta,\\
R^\theta{}_{\phi\theta\phi} &= \left(1 - e^{-2\beta}\right)\sin^2\theta.
\end{aligned} \tag{2.39}$$

The non-zero components of the Ricci tensor for the Schwarzschild metric are

$$\begin{aligned}
R_{tt} &= e^{2(\alpha-\beta)}\left[\partial_r^2\alpha + (\partial_r\alpha)^2 - \partial_r\alpha\partial_r\beta + \frac{2}{r}\partial_r\alpha\right],\\
R_{rr} &= -\partial_r^2\alpha - (\partial_r\alpha)^2 + \partial_r\alpha\partial_r\beta + \frac{2}{r}\partial_r\alpha,\\
R_{\theta\theta} &= e^{-2\beta}\left[r\left(\partial_r\beta - \partial_r\alpha\right) - 1\right] + 1,\\
R_{\phi\phi} &= \sin^2\theta R_{\theta\theta}.
\end{aligned} \tag{2.40}$$

The Ricci scalar is given by

$$R = -2e^{-2\beta}\left[\partial_r^2\alpha + (\partial_r\alpha)^2 - \partial_r\alpha\partial_r\beta + \frac{2}{r}\left(\partial_r\alpha - \partial_r\beta + \frac{1}{2r}\left(1-e^{2\beta}\right)\right)\right]. \quad (2.41)$$

Since we are interested in the solution outside a spherical body. This equivalents to Einstein equation in vacuum

$$R_{\mu\nu} = 0. \quad (2.42)$$

Then, we obtain

$$0 = e^{2(\beta-\alpha)}R_{tt} + R_{rr} = \frac{2}{r}\left(\partial_r\alpha + \partial_r\beta\right), \quad (2.43)$$

Eq. (2.43) implies $\alpha = -\beta + c$, where c is some constant. By considering the spacetime very far from this object, the spacetime must be flat. Then the line element must be

$$ds^2 = -dt^2 + dr^2 + r^2\left(d\theta^2 + \sin^2\theta d\phi^2\right). \quad (2.44)$$

So, the constant c must to be zero i.e.,

$$\alpha = -\beta. \quad (2.45)$$

By substituting Eq. (2.45) to $R_{\theta\theta}$ in Eq. (2.40), we obtain

$$\begin{aligned} e^{2\alpha}\left(2r\partial_r\alpha + 1\right) &= 1, \\ \partial_r\left(re^{2\alpha}\right) &= 1. \quad (2.46) \end{aligned}$$

Then we can solve this differential equation to obtain

$$e^{2\alpha} = 1 - \frac{R_s}{r}, \quad (2.47)$$

where R_s is an undetermined constant. Thus, we write the line element from Eq.(2.37

$$ds^2 = -\left(1-\frac{R_s}{r}\right)dt^2 + \left(1-\frac{R_s}{r}\right)^{-1}dr^2 + r^2\left(d\theta^2 + \sin^2\theta d\phi^2\right). \quad (2.48)$$

In the weak-field limit, the time-time component of the metric is given by

$$g_{tt} = -\left(1 + 2\phi\right), \tag{2.49}$$

where "ϕ" is the Newtonian gravitational potential. For a point mass "M" , the Newtonian potential is

$$\phi = -\frac{GM}{r}. \tag{2.50}$$

Substituting this into the expression for "g_{tt}", we obtain

$$g_{tt} = -\left(1 - \frac{2GM}{r}\right). \tag{2.51}$$

Comparing this with the time-time component of the Schwarzschild metric, we identify that

$$\frac{R_s}{r} = \frac{2GM}{r}, \tag{2.52}$$

which leads to the conclusion that the Schwarzschild radius is

$$R_s = 2GM. \tag{2.53}$$

This result represents the radius of a black hole with mass "M", and if an object's radius becomes smaller than "R_s," it will form a black hole. Therefore, we can obtain the Schwarzschild solution as

$$ds^2 = -\left(1 - \frac{2GM}{r}\right) dt^2 + \left(1 - \frac{2GM}{r}\right)^{-1} dr^2 + r^2 \left(d\theta^2 + \sin^2\theta d\phi^2\right). \tag{2.54}$$

The Schwarzschild solution describes the geometry of spacetime outside a non-rotating, spherically symmetric object, such as a star or planet. However, when the object is very massive and compact, it can undergo gravitational collapse, and the resulting object is called a black hole. The Schwarzschild solution can then be used to describe the geometry of spacetime outside the black hole as well. For the convenience of our later works, we take $c = G = M = 1$ as a unit.

CHAPTER III

GREYBODY FACTOR FOR BLACK HOLES

In this chapter, we present the methodology for deriving the greybody factor in black hole spacetimes by delving into the study of quantum scattering and black hole scattering theories. In this sense, considering a test particle field around a black hole geometry, the master equation depends on an effective potential at the exterior region of the black hole event horizon, which dominated the behaviors of the test particles in such areas. Studying the scattering properties of a test particle with the black hole effective potential is analogous to a quantum scattering problem. Specifically, the greybody factor is the transmission probability that quantifies the likelihood of particle emissions escaping a black hole.

This chapter is organized as follows. In Ch. 3.1, we review the standard quantum scattering problem with potential barrier. In Ch. 3.2, we present an example of deriving the master equation and the effective potential for the Klein-Gordon equation in the Schwarzschild black hole spacetime, which allows us to link the black hole scattering problem with the quantum scattering one. Lastly, we introduce two approaches to our investigation of the black hole greybody factor i.e., the rigorous bound method and the WKB approximation, which shall be presented in Ch. 3.3 and Ch. 3.4, respectively.

3.1 Scattering Problems of a Potential Barrier

In quantum mechanics, the Schrödinger equation stands as a quiddity, providing a fundamental description of how the quantum state of a physical system evolves. This equation was named after the Austrian physicist Erwin Schrödinger who formulated it in 1926 [26]. The time-independent Schrödinger equation can

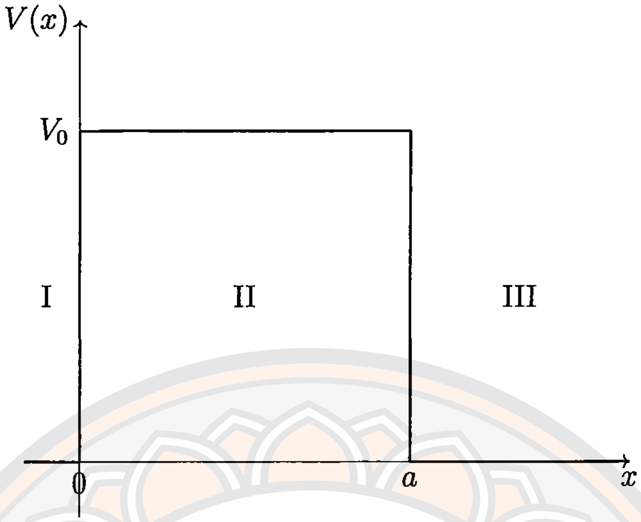

Figure 1 The barrier potential well.

be expressed as

$$-\frac{\hbar^2}{2m}\frac{d^2}{dx^2}\psi(x) + V(x)\psi(x) = E\psi(x), \tag{3.1}$$

where "$\hbar$" denotes the Planck constant, "m" is the mass of the particle, "$V(x)$" represents the potential, and "$\psi(x)$" is the wave function. This equation holds particular significance in the Quantum Scattering Problem, where it is utilized to analyze how quantum particles scatter when encountering a potential energy barrier or well. To explore the scattering process, we often assume a solution of the form

$$\psi(x,t) = \psi(x)\exp\left(\frac{iEt}{\hbar}\right). \tag{3.2}$$

The example of a rectangular 1-dimensional potential barrier $V(x)$ of height V_0 and with width a [27] is given by

$$V(x) = \begin{cases} 0 & \text{for } x < 0 \quad \text{, Region I} \\ V_0 & \text{for } 0 \leq x \leq a \quad \text{, Region II} \\ 0 & \text{for } x > a \quad \text{, Region III} \end{cases} \cdot \tag{3.3}$$

as shown in Fig. 1. In one dimension, two distinct directions are possible for the propagation of waves, which can be expressed as e^{+ikx} for the right moving waves and e^{-ikx} for the left moving one. The general solution of Eq. (3.1) can be expressed as

$$\psi(x) = \begin{cases} \mathrm{A}e^{ikx} + Be^{-ikx} & \text{for } \mathrm{x} < 0, \quad \text{Region I} \\ \mathrm{C}e^{iqx} + De^{-iqx} & \text{for } 0 < \mathrm{x} < \mathrm{a}, \quad \text{Region II} \\ \mathrm{F}e^{ikx} & \text{for } \mathrm{x} > \mathrm{a}, \quad \text{Region III} \end{cases} , \tag{3.4}$$

where

$$k^2 = \frac{2mE}{\hbar} \;\; ; \;\; q^2 = \frac{2m(E - V_0)}{\hbar}. \tag{3.5}$$

In this case, the incident particle comes from $x = -\infty$. We can solve the coefficients by considering the boundary conditions. To determine the coefficients A, B, C, D, and F. The coefficients B and F correspond to the reflection and transmission amplitudes, respectively. We apply the continuity of the wave function and its first derivative at the boundaries $x = 0$ and $x = a$.

The boundary at $x = 0$

1. Continuity of the Wave Function

$$\psi_I(0) = \psi_{II}(0) \implies A + B = C + D. \tag{3.6}$$

2. Continuity of the First Derivative

$$\psi_I{\prime}(0) = \psi_{II}{\prime}(0) \implies ik(A - B) = iq(C - D). \tag{3.7}$$

The Boundary at $x = a$

1. Continuity of the Wave Function

$$\psi_{II}(a) = \psi_{III}(a) \implies Ce^{iqa} + De^{-iqa} = Fe^{ika}. \tag{3.8}$$

2. Continuity of the First Derivative as

$$\psi_{II}{\prime}(a) = \psi_{III}{\prime}(a) \implies iq(Ce^{iqa} - De^{-iqa}) = ikFe^{ika}. \tag{3.9}$$

Thus the solutions for the transmission and reflection coefficients as

1. Transmission Coefficient (F)

$$F = \frac{4kqe^{-ika}}{2kq\cos(qa) - i(k+q)\sin(qa)}A. \tag{3.10}$$

2. Reflection Coefficient (B)

$$B = \frac{-i(k^2 - q^2)\sin(qa)}{2kq\cos(qa) - i(k^2+q^2)\sin(qa)}A. \tag{3.11}$$

Therefore, the transmission and reflection probability are

$$T = \left|\frac{F}{A}\right|^2 \quad ; \quad R = \left|\frac{B}{A}\right|^2, \tag{3.12}$$

and the sum of the probabilities of these two mutually exclusive is

$$R + T = 1. \tag{3.13}$$

This equation is a direct consequence of the conservation of probability in quantum mechanics. It ensures that when summed over all the possible outcomes (reflection and transmission), the total probability of finding the particle remains one.

3.2 The barrier-like effective potentials in the black hole perturbation theory

Black holes were known as compact objects described by the classical gravitational theories, General Relativity(GR), or modified GR. If we consider the behavior of particles around the black hole geometry, the effective potentials can usually be derived by the study of the black hole perturbation theory. The structure of the effective potentials varies depending on the perturbative fields and the different types of black hole spacetimes, and one of the common shapes is the barrier-like one. The effective potential refers to the energy profile that describes the motion of an object or particle around a black hole under the influence of gravity potential. For the barrier-like effective potentials, the behavior of particles can be analogous to quantum tunneling with the boundary conditions of ingoing and outgoing waves to the black hole event horizon, and purely outgoing waves to the spatial infinity. We presented the summary of the massless scalar perturbation in the Schwarzschild black hole spacetime as an example to explain how similar the black hole perturbation to the Quantum scattering problem in this subsection.

First of all, we consider the Schwarzschild black hole in the coordinates (t, r, θ, ϕ)

$$ds^2 = -f(r)dt^2 + f(r)^{-1}dr^2 + r^2\left(d\theta^2 + \sin^2\theta d\phi^2\right), \tag{3.14}$$

where $f(r) = 1 - \frac{2}{r}$. We examine the black-hole perturbations by introducing a scalar (Klein–Gordon) field, and the Klein-Gordon equation can be written as

$$\nabla_\mu \nabla^\mu \Phi = 0, \tag{3.15}$$

where Φ is the wave function. We use the separation of variables for the Klein-Gordon equation,

$$\Phi(t, r, \theta, \phi) \;=\; e^{-i\omega t} R(r)\, Y^{\ell m}(\theta, \phi), \tag{3.16}$$

where $Y^{\ell m}(\theta, \phi)$ are spherical harmonics (in four-dimensional spacetime), and ω is the wave frequency. We write

$$R(r) \;=\; A(r)\, u_{\ell m}(r), \tag{3.17}$$

which is a general technique allowing one to recast the radial equation into a more convenient form. Here, $A(r)$ is a nonzero arbitrary function, and $u_{lm}(r)$ is the remaining radial function. We can write the eigenvalue of the spherical harmonics as

$$\left(\frac{1}{r^2}\partial_\theta^2 + \frac{1}{r^2}\cot\theta\partial_\theta + \frac{1}{r^2\sin^2\theta}\partial_\phi^2\right) Y^{lm} = -\frac{l(l+1)}{r^2} Y^{lm}, \tag{3.18}$$

where define the tortoise coordinate r_*

$$\frac{dr_*}{dr} = \left(1 - \frac{2}{r}\right)^{-1}. \tag{3.19}$$

By substituting Eqs. (3.16)-(3.18) in to Eq. (3.15), we can solve $A(r)$ through

$$\frac{(\partial_{r_*} A(r))}{A(r)} = \frac{-2}{r}, \tag{3.20}$$

and the radial equation can be obtained as

$$\frac{d^2 u_{lm}}{dr_*^2} + \left[\omega^2 - V_{eff}(r)\right] u_{lm} = 0, \tag{3.21}$$

where

$$V_{eff}(r) = \left(1 - \frac{2}{r}\right)\left(\frac{l(l+1)}{r^2} + \frac{1}{r}\frac{df}{dr}\right). \tag{3.22}$$

The Eq. (3.21) is called the Regge-Wheeler equation for a scalar field perturbation in Schwarzhild spacetime, the solution of this equation helps determine how black holes interact with a scalar field. The effective potential $V_{eff}(r)$ in Eq. (3.22) plays an important role in the analysis of scalar field perturbation around Schwarzschild spacetime. The effective potential is frequently barrier-like and allows us to analogize to the quantum scattering for solving the transmission and reflection problems.

We examine the asymptotic forms of solution of $u_{lm}(r)$ far from the black hole $r_* \to \infty$ and near the event horizon of black holes $r_* \to -\infty$,

$$u_{lm}(r) = \begin{cases} e^{\pm i\omega r_*} & \text{for } r_* \to -\infty \\ e^{\pm i\omega r_*} & \text{for } r_* \to +\infty \end{cases}, \tag{3.23}$$

To solve the equation, appropriate boundary conditions must have "Ingoing Mode" and "Outgoing mode". These two modes refer to specific types of wave solutions to the Regge-Wheller equation subjected to the boundary conditions Eq. (3.23).

In classical physics, there are no outgoing waves from the event horizon. Therefore, we consider the linear combination of ingoing and outgoing waves at spatial infinity and a purely ingoing wave at the event horizon. This case is referred to as the "Ingoing mode" and the wave function is given by

$$u^{in}_{lm}(r) = \begin{cases} e^{-i\omega r_*} & \text{for } r_* \to -\infty \\ A_{out}(\omega)e^{+ikr_*} + A_{in}(\omega)e^{-ikr_*} & \text{for } r_* \to +\infty \end{cases}, \tag{3.24}$$

The complex conjugate of Eq. (3.24) is called an "Outgoing mode". The coefficients $A_{out}(\omega)$ and $A_{in}(\omega)$ represent the amplitude of the ongoing and outgoing wave, respectively.

In the scattering process, an incoming wave from spatial infinity interacts with the potential barrier. This interaction results in a portion of the wave being transmitted through the barrier and absorbed by the black hole. We can define the transmission coefficients by considering the Wronskian $W(u_1, u_2)$ of two functions u_1 and u_2 that satisfy the Regge-Wheeler equation for scalar field

$$W(u_1, u_2) = u_1 \frac{du_2}{dr_*} - u_2 \frac{du_1}{dr_*}. \tag{3.25}$$

The Wronskian of incoming and outcoming solutions near the event horizon as $r_* \to -\infty$ is given by

$$\begin{aligned} W(u^{in}_{lm}, u^{out}_{lm}) &= u^{in}_{lm} \frac{du^{out}_{lm}}{dr_*} - u^{out}_{lm} \frac{du^{in}_{lm}}{dr_*}, \\ &= i\omega \left(e^{-i\omega r_*} e^{i\omega r_*} + e^{i\omega r_*} e^{-i\omega r_*}\right), \\ &= 2i\omega, \end{aligned} \tag{3.26}$$

and the spatial infinity for $r_* \to \infty$ is

$$W(u^{in}_{lm}, u^{out}_{lm}) = 2i\omega \left(|A_{in}|^2 - |A_{out}|^2\right). \tag{3.27}$$

Any solutions of Eq. 3.21 need to have a constant Wronskian $W(u^{in}_{lm}, u^{out}_{lm})$, thus

$$1 = (|A_{in}|^2 - |A_{out}|^2). \tag{3.28}$$

We divided $|A_{in}|^2$ for both sides of the equation and together with the conservation law, the transmission coefficient $\mathcal{T}$ and reflection coefficient $\mathcal{R}$ are given by

$$|\mathcal{T}|^2 = 1 - |\mathcal{R}|^2, \tag{3.29}$$

where

$$\mathcal{T} = \frac{1}{A_{in}} \quad , \quad \mathcal{R} = \frac{A_{out}}{A_{in}}. \tag{3.30}$$

In addition, the mathematical structure of “ Outgoing modes” is exactly the same as the “Ingoing mode”. The “Outgoing modes” are closely linked to the Hawking radiation, which arises from quantum effects near the event horizon.

3.3.2 Bound

In this subsection, we derive the bounds on the greybody factor by using the Bogoliubov coefficients. The details shall refer to the paper [28], [30]. The Bogoliubov transformation relates the coefficients of the incoming and outgoing wave function, which helps in understanding the transmission and reflection probabilities.

We follow the definition similar to the previous section in Eq. (3.24). In this case, to obtain the bounds on the Bogoliubov coefficients, we start by considering the probability current

$$\mathscr{J} = Im\{\psi^* \frac{d\psi}{dx}\} = |b|^2 - |a|^2. \tag{3.41}$$

Unifying the total probability, we have

$$|b|^2 - |a|^2 = 1. \tag{3.42}$$

This relation implies that the probability current is a conserved quantity for all x, and the relation of the derivative of complex numbers can written as

$$\frac{d|a|}{dx} = \frac{1}{2|a|}\left(a^* \frac{da}{dx} + a\frac{da^*}{dx}\right). \tag{3.43}$$

Applying this relation to the Eq. (3.39), we have

$$\begin{aligned} \frac{d|a|}{dx} &= \frac{1}{2|a|}\frac{1}{2\varphi'}\Big(\varphi''[a^* b \exp(-2i\varphi) + ab^* \exp(+2i\varphi)] \\ &+ i[k^2 - \varphi'^2][a^* b \exp(-2i\varphi) - ab^* \exp(+2i\varphi)]\Big). \end{aligned} \tag{3.44}$$

Since $ab^* e^{(2i\varphi)} = (a^* b e^{(-2i\varphi)})^*$, considering the property of the real part of a complex number, $Z + \bar{Z} = 2Re(Z)$, we obtain

$$\frac{d|a|}{dx} = \frac{1}{2|a|}\frac{1}{\varphi'} Re\Big((\varphi'' + i[k^2 - (\varphi')^2]ab^* \exp(-2i\varphi)\Big). \tag{3.45}$$

We next impose a general relation of complex numbers as

$$Re(AB) \leq |A||B|, \tag{3.46}$$

Therefore, Eq. (3.45) can be rewrite as

$$\frac{d|a|}{dx} \leq \frac{\sqrt{\varphi''^2 + (k^2 - \varphi'^2)^2}}{2|\varphi'|}|b||e^{-2i\varphi}|. \tag{3.47}$$

Since $|e^{-2i\varphi}| = 1$, we define the non-negative quantity by

$$\vartheta(\varphi(x), k(x)) \equiv \frac{\sqrt{\varphi''^2 + (k^2 - \varphi'^2)^2}}{2|\varphi'|}, \tag{3.48}$$

together with Eqs. (3.42) and (3.47), we can write

$$\frac{d|a|}{dx} \leq \vartheta(\varphi(x), k(x))\sqrt{|a|^2 + 1}. \tag{3.49}$$

We next solve $|a|$ by integrating both sides of the inequality

$$\begin{aligned} \int_{-\infty}^{\infty} \frac{1}{\sqrt{|a|^2+1}} d|a| &\leq \int_{-\infty}^{\infty} \vartheta(\varphi(x), k(x))dx, \\ \sinh^{-1}|a|\Big|_{x\to-\infty}^{x\to\infty} &\leq \int_{-\infty}^{\infty} \vartheta(\varphi(x), k(x))dx, \\ |a|\Big|_{x\to-\infty}^{x\to\infty} &\leq \sinh\left(\int_{-\infty}^{\infty} \vartheta(\varphi(x), k(x))dx\right). \end{aligned} \tag{3.50}$$

By comparing Eq. (3.31) with Eq. (3.24), we impose the boundary conditions

$$a(\infty) \equiv \alpha \quad , \quad a(-\infty) \equiv 0. \tag{3.51}$$

From these conditions, we deduce

$$|\alpha| \leq \sinh\left(\int_{-\infty}^{\infty} \vartheta(\varphi(x), k(x))dx\right). \tag{3.52}$$

To solve for "b", we substitute Eq. (3.52) into the Eq. (3.42)

$$\begin{aligned} |a|^2\big|_{x\to\infty} = |b|^2\big|_{x\to\infty} - 1 &\leq \sinh^2\left(\int_{-\infty}^{\infty} \vartheta(\varphi(x), k(x))dx\right), \\ |b|^2\big|_{x\to\infty} &\leq \cosh^2\left(\int_{-\infty}^{\infty} \vartheta(\varphi(x), k(x))dx\right), \end{aligned} \tag{3.53}$$

We impose the boundary conditions $|b|\big|_{x\to\infty} \equiv |\beta|$, we obtain

$$|\beta| \leq \cosh\left(\int_{-\infty}^{\infty} \vartheta(\varphi(x), k(x))dx\right). \tag{3.54}$$

Comparing with Eqs. (3.24),(3.31)and (3.42).

$$A_{in} \sim |\beta| \quad , \quad A_{out} \sim |\alpha|. \tag{3.55}$$

Therefore, we may write the transmission and reflection probabilities as

$$T = |\frac{1}{A_{in}}|^2 = \frac{1}{|\beta|^2} \geq \operatorname{sech}^2\left(\int_{-\infty}^{+\infty} \vartheta(\varphi(x), k(x))dx\right), \tag{3.56}$$

$$R = |\frac{A_{out}}{A_{in}}|^2 = \frac{|\beta|^2}{|\alpha|^2} \leq \tanh^2\left(\int_{\infty}^{+\infty} \vartheta(\varphi(x), k(x))dx\right). \tag{3.57}$$

We will use these the rigorous bound to calculate the greybody factor in the next chapter.

3.4 WKB approximation

Another powerful method to analyze black hole perturbation is the Wentzel-Kramers-Brillouin (WKB) approximation [15]. This method approximates solutions to the wave equation for black hole perturbations. By matching solutions across turning points, the transmission and reflection coefficients can be determined. Clifford M. Will and James W.Guinn detail the application of the WKB approximation for the transmission probability (greybody factor) in 1988 [16]. In this section, a brief introduction of this method will be summarized.

3.4.1 Tunneling near the peaks of potential barries

The WKB approximation, originally developed in the context of quantum mechanics to solve the Schrödinger equation with a varying potential, was applied by Clifford M. Will and James W. Guinn to the study of black hole perturbations. The Schrödinger equation and the Regge-Wheeler equation share a similar mathematical form, which allows techniques from quantum mechanics to be adapted to gravitational systems.

$$\frac{d^2\psi}{dx^2} + Q(x)\psi = 0, \tag{3.58}$$

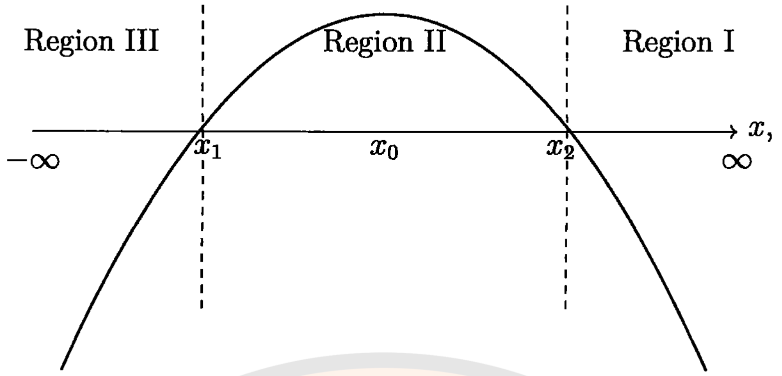

Figure 2 The potential well of function $Q(x)$ near its peak.

in quantum mechanics $-Q = (2m/\hbar^2)(V - E)$, while for black hole pertubation cases, Q depends on the field pertubations which known as the effective potentials and usually be barrier-like as Fig. 2 . In the Schwarschild black hole case, x is the trotoise coordinate varries from $-\infty$ to $+\infty$, which represents the event horizon and radial infinity respectively. The radial equation for the general form as

$$\epsilon^2 \frac{d^2\psi}{dx^2} + Q(x)\psi(x) = 0, \tag{3.59}$$

where ϵ is a small pertubation parameter to keep track of order in the WKB approximation. We then define the asymptotic approximation as

$$\psi(r) \sim e^{S(x)/\epsilon}, \tag{3.60}$$

where $S(x)$ is a complex function. We can expand the function $S(x)$ as

$$S(x) = \sum_{n=0}^{\infty} \epsilon^n S_n(x), \tag{3.61}$$

where ϵ is a small parameter representing the order of this method. We obtain the third-order WKB approximation. This series expansion allows us to systematically solve the wave functions order by order and improve the accuracy of the approximation represented by the "matching area" as shown in Fig. 2. We then insert this expasion into the Eq. (3.59), collecting terms order by order in ϵ, and solve sequentially for S

$$S_0(x) = \pm \int^x [Q(\eta)]^{1/2}\, d\eta, \tag{3.62}$$

$$S_1(x) = -\frac{1}{4} \ln Q(x), \tag{3.63}$$

$$S_2(x) = \mp\frac{1}{8} \int^x \left[\frac{Q''}{Q^{3/2}} - \frac{5}{4}\frac{Q'^2}{Q^{5/2}}\right] d\eta, \tag{3.64}$$

$$S_3(x) = \frac{1}{16}\left[\frac{Q''}{Q^2} - \frac{5}{4}\frac{Q'^2}{Q^3}\right]. \tag{3.65}$$

Note that, as $x \to \infty$, the positive or upper sign in Eq. (3.62) corresponds to the outgoing wave (right going to spatial infinity), while the negative or lower sign corresponds to the incoming wave (left going to the barrier). As $x \to -\infty$, the positive or upper sign corresponds to waves coming from $-\infty$ (right going to the barrier), while the negative or lower sign corresponds to waves going toward $-\infty$ (left going to event horizon). We can write the general solution of exterior regions I and III as shown in Fig. 2,

$$\psi \sim Z_{\text{in}}^{(I)} \psi_-^{(I)} + Z_{\text{out}}^{(I)} \psi_+^{(I)} \quad \text{region I}, \tag{3.66}$$

$$\psi \sim Z_{\text{in}}^{(III)} \psi_+^{(III)} + Z_{\text{out}}^{(III)} \psi_-^{(III)} \quad \text{region III}, \tag{3.67}$$

here, $Z_{\text{in}}^{(I)}$ and $Z_{\text{out}}^{(I)}$ represent the components of the wave traveling to the right going to spatial infinity and the left going to the barrier, respectively. Likewise $Z_{\text{in}}^{(III)}$ and $Z_{\text{out}}^{(III)}$ represent wave components going to the left going to the event horizon, and the right going to the barrier, respectively.

Now we consider an incident wave coming from the right($x = \infty$). The boundary condition for the wave function ψ will be given by ensuring that there is no incoming wave from the left at the event horizon $Z_{in}^{III} = 0$. The outgoing wave at spatial infinity is the same wave that was generated at the event horizon $Z_{out}^{III} = Z_{hole}$.

The modification of usual WKB procedure involves matching the two WKB solutions of Eq. (3.59), We investigated this problem by expanding Q near its peak at x_0 in a Taylor series of the form

$$
\begin{aligned}
Q(x) &= Q_0 + \frac{1}{2}Q_0'' + \sum_{n=3} \frac{1}{n!}\left(d^nQ/dx^n\right)_0 z^n, \\
&= Q_0 + \frac{1}{2}Q_0''z^2 + \frac{1}{6}Q_0''z^3 + \frac{1}{24}Q_0^{(4)}z^4 + \frac{1}{120}Q_0^{(5)}z^5 + \frac{1}{170}Q_0^{(6)}z^6, \quad (3.68)
\end{aligned}
$$

Eq. 3.59 can then be written

$$
\epsilon^2\frac{d^2\psi}{dz^2} + k(-z_0^2 + z^2 + bz^3 + cz^4 + dz^5 + fz^6)\psi = 0, \tag{3.69}
$$

where

$$
\begin{aligned}
z = x - x_0 \quad &, \quad z_0^2 = -2\frac{Q_0}{Q_0''}, \\
k = \frac{1}{2}Q_0'' \quad &, \quad b = \frac{1}{3}Q_0'''/Q_0'', \\
d \equiv \frac{1}{60}Q_0^{(5)}/Q_0''' \quad &, \quad f = \frac{1}{360}Q_0^{(6)}/Q_0''.
\end{aligned} \tag{3.70}
$$

Note that, primes denoted derivative to x, the upper number in the bracket represented the order of the derivatives, and subscript zero denoting evaluation $z = 0 (x = x_0)$. At the peak$(x = x_0)$ of $Q(x)$, the first derivative Q_0' must be zero. For express the asymptotic solution of the interior barrier, we need to define a new variable. That will correspond to finite overlap regions outside the turning point where the solution may be matched asymptotically to the WKB. Along with a transformation on the "z" parameter, one may observe that the leading-orders terms are in the form of the ordinary differential equation of parabolic cylinder function. For the higher-order terms, additional modifications are required to solve the corresponding higher-order parabolic cylinder equations. Lastly, we need to match the exterior wave function with the higher order parabolic cylinder functions around the turning point x_1 and x_2 order by order. The technical details shall refer to the original paper [15], and the result expression is then given by

$$\begin{aligned} S(x) &= \pi k^{1/2}\left[\frac{1}{2}z_0^2+\left(\frac{15}{64}b_3^2-\frac{3}{16}b_4\right)z_0^4\right] \\ &\quad +\pi k^{1/2}\left[\frac{1155}{2048}b_3^4-\frac{315}{256}b_3^2b_4+\frac{35}{64}b_3b_5-\frac{5}{32}b_6\right]z_0^6+\pi k^{-1/2}\left[\frac{3}{16}b_4-\frac{7}{64}b_3^2\right] \\ &\quad -\pi k^{-1/2}\left[\frac{1365}{2048}b_3^4-\frac{525}{256}b_3^2b_4+\frac{85}{128}b_4^2+\frac{95}{64}b_3b_5-\frac{25}{32}b_6\right]z_0^2+\mathcal{O}(x), \end{aligned} \tag{3.71}$$

and the transmission coefficient of a barrier-like potential can be expressed as

$$\mathcal{T}=\frac{1}{1+e^{2S}}. \tag{3.72}$$

In this work, we will calculate the greybody factor for the Proca field in the Schwarzschild background using the WKB approach outlined above.

CHAPTER IV

PROCA FIELD IN CRUVED SPACE

In black hole physics, greybody factors quantify the deviation of Hawking radiation from a perfect blackbody spectrum due to the scattering of particles by the curved spacetime geometry. While many studies have focused on scalar, fermionic, or electromagnetic fields, the behavior of massive vector fields—described by the Proca equation—remains less explored. The Proca field is particularly interesting because, unlike massless vector fields (such as the electromagnetic field), it lacks gauge symmetry, leading to a richer and more complex interaction with curved spacetime, also contributes to the broader effort to understand how different types of field behave near black hole. This chapter encompasses an examination of vector fields in the spherically symmetric black hole spacetimes and later delves into the analysis of the radial equation for the computation of the greybody factor in the Schwarzschild black hole background. The line element for the spherically symmetric black hole solution is expressed in terms of the coordinates $x^\nu = \{t, r, \theta, \phi\}$, therefore, four equations of motion shall be obtained for the Proca field.

To achieve master equation, we utilize vector spherical harmonics (VSH) [9] to separate the angular part of the vector potential components of the Proca field equations, and four radial equations will be derived. These equations encompass a full separated odd-parity equation and the coupled even-parity equations. To solve the coupled equations of the even-parity solutions, we employ Frolov–Krtouš–Kubizňák–Santos (FKKS) [11] ansatz, which allows us to obtain one single radius equation for the even-parity mode. Lastly in this chapter, we check the properties of the effective potentials for both modes, as well as the consistency of coupled equations.

4.1 Proca field in spherically symmetric black hole solution

The line element for the spherical symmetric black hole solution can be described by coordinates $x^\nu = \{t, r, \theta, \phi\}$ and takes the form

$$ds^2 = -f(r)dt^2 + f(r)^{-1}dr^2 + r^2(d\theta^2 + \sin^2\theta d\phi^2). \tag{4.1}$$

where $f(r)$ in the line elements is the function depends on the black hole radius. The non-vanishing components of the Christoffel symbols are computed as

$$\begin{aligned}
&\Gamma^t{}_{tr} = \Gamma^t{}_{rt} = \frac{f'(r)}{2f(r)}, && \Gamma^r{}_{rr} = -\frac{f'(r)}{2f(r)},\\
&\Gamma^r{}_{tt} = \frac{f'(r)f(r)}{2}, && \Gamma^r{}_{\theta\theta} = -rf(r),\\
&\Gamma^\theta{}_{r\theta} = \Gamma^\theta{}_{\theta r} = \frac{1}{r}, && \Gamma^r{}_{\phi\phi} = -r\sin^2\theta f(r),\\
&\Gamma^\phi{}_{\theta\phi} = \Gamma^\phi{}_{\phi\theta} = \cot\theta, && \Gamma^\theta{}_{\phi\phi} = -\sin\theta\cos\theta,\\
&\Gamma^\phi{}_{r\theta} = \Gamma^\phi{}_{\phi r} = \frac{1}{r},
\end{aligned} \tag{4.2}$$

where $f'(r) = \partial_r f(r)$. The non-vanishing components of the Ricci tensor are

$$\begin{aligned}
R_{tt} &= f\left(\tfrac{f''}{2} + \tfrac{f'}{r}\right), & R_{rr} &= -\frac{1}{f}\left(\frac{f''}{2} + \frac{f'}{r}\right),\\
R_{\theta\theta} &= -rf' - f + 1, & R_{\phi\phi} &= -(rf' + f - 1)\sin^2\theta.
\end{aligned} \tag{4.3}$$

The field strength tensor $F_{\mu\nu}$ in curved spacetime is defined in terms of the vector potential A_ν as

$$F_{\mu\nu} = \nabla_\mu A_\nu - \nabla_\nu A_\mu, \tag{4.4}$$

the Proca field equation in curved spacetime is written as

$$\nabla_\mu F^{\mu\nu} = \mu^2 A^\nu, \tag{4.5}$$

where μ is Proca's mass. Taking the covariant derivative ∇_ν of the field equation Eq. (4.5) yields

$$\begin{aligned}
\nabla_\nu\nabla_\mu F^{\mu\nu} &= \mu^2\nabla_\nu A^\nu,\\
0 &= \mu^2\nabla_\nu A^\nu,
\end{aligned} \tag{4.6}$$

which implies the Lorenz condition $\nabla_\mu A^\mu = 0$. We next substitute $F_{\mu\nu}$ to Eq. (4.5), one get

$$\nabla_\mu \nabla^\mu A^\nu - \nabla_\mu \nabla^\nu A^\mu - \mu^2 A^\nu = 0. \tag{4.7}$$

Firstly, we consider the second term in Eq. (4.7), with the definition of covariant and contravariant derivatives in Eq. (2.4) and Eq. (2.6), this term becomes

$$\begin{aligned} \nabla_\mu \nabla^\nu A^\mu &= g^{\nu\rho}\{\partial_\rho(\nabla_\mu A^\mu) - (\partial_\rho \Gamma^\mu_{\mu\sigma})A^\sigma + (\partial_\sigma \Gamma^\sigma_{\rho\mu})A^\mu \\ &\quad + \Gamma^\mu_{\mu\sigma}\Gamma^\sigma_{\rho\beta}A^\beta - \Gamma^\sigma_{\rho\mu}\Gamma^\mu_{\sigma\beta}A^\beta\}. \end{aligned} \tag{4.8}$$

Proca's field equation admits the Lorenz condition by considering the commutator of the field strength tensor

$$[\nabla_\mu, \nabla_\nu]F^{\mu\nu} = R^\mu_{\lambda\mu\nu}F^{\lambda\nu} + R^\nu_{\lambda\mu\nu}F^{\lambda\mu}, \tag{4.9}$$

$$= R_{\lambda\nu}F^{\lambda\nu} + R_{\mu\lambda}F^{\mu\lambda}. \tag{4.10}$$

Since $F^{\mu\nu}$ is antisymmetric, and Schwarzschild spacetime is a vacuum solution, we can impose the Lorenz condition $\nabla_\mu A^\mu = 0$ into Eq. (4.8) to simplify the equation of motion as follows

$$\begin{aligned} \nabla_\mu \nabla^\nu A^\mu &= g^{\nu\rho} R^\sigma{}_{\mu\sigma\rho} A^\mu, \\ &= R_\mu{}^\nu A^\mu, \end{aligned} \tag{4.11}$$

this equation relates to the Ricci tensor. Then the Proca field equation can be written as

$$\nabla_\mu \nabla^\mu A^\nu - \mu^2 A^\nu - R_\mu{}^\nu A^\mu = 0. \tag{4.12}$$

Next,the first term in Eq. (4.12) is evaluated as

$$\begin{aligned} \nabla_\mu \nabla^\mu A^\nu &= g^{\mu\rho}\big[\partial_\mu \partial_\rho A^\nu + \partial_\mu \left(\Gamma^\nu{}_{\rho\sigma} A^\sigma\right) - \Gamma^\sigma{}_{\mu\rho}\partial_\sigma A^\nu \\ &\quad - \Gamma^\beta{}_{\mu\rho}\Gamma^\nu{}_{\beta\sigma}A^\sigma + \Gamma^\nu{}_{\mu\sigma}\partial_\rho A^\sigma + \Gamma^\nu{}_{\mu\beta}\Gamma^\beta{}_{\rho\sigma}A^\sigma\big]. \end{aligned} \tag{4.13}$$

By combining Eqs. (4.12) and (4.13), the equations of motion for the Proca field in curved spacetime is derived.

4.2 The vector spherical harmonic(VSH)

To solve the Eq. (4.12), we separate the angular components by employing the ansatz for the vector potential introduced in [9] , based on the following decomposition

$$A_\mu(t,r,\theta,\phi) = \frac{1}{r}\sum_{i=1}^{4}\sum_{lm} c_i u_{(i)}^{lm}(t,r) Z_\mu^{(i)lm}(\theta,\phi), \tag{4.14}$$

where $c_1 = c_2 = 1, c_3 = c_4 = (l(l+1))^{-1/2}$ and $Z_\mu^{(i)lm}(\theta,\phi)$ is four vector spherical harmonics. This expression represents the vector potential that can be decomposed into a series of angular basis functions. The coefficients c_i determint the amplitude of each mode, and the functions $u_{(i)}^{lm}(t,r)$ and $Z_\mu^{(i)lm}(\theta,\phi)$ represent time-radial and angular dependencies, respectively. We further defined the angular dependence as follows

$$\begin{aligned}
Z_\mu^{(1)lm} &= [1,0,0,0]Y^{lm}(\theta,\phi), && (4.15)\\
Z_\mu^{(2)lm} &= [0,f^{-1},0,0]Y^{lm}(\theta,\phi), && (4.16)\\
Z_\mu^{(3)lm} &= \frac{r}{\sqrt{l(l+1)}}[0,0,\partial_\theta,\partial_\phi]Y^{lm}(\theta,\phi), && (4.17)\\
Z_\mu^{(4)lm} &= \frac{r}{\sqrt{l(l+1)}}[0,0,\frac{1}{\sin\theta}\partial_\phi,-\sin\theta\partial_\theta]Y^{lm}(\theta,\phi). && (4.18)
\end{aligned}$$

From the decompose the vector potential we can write down

$$\begin{aligned}
A_t &= \frac{1}{r}\sum_{lm} u_{(1)}^{lm}(t,r)Y^{lm}(\theta,\phi), && (4.19)\\
A_r &= \frac{1}{fr}\sum_{lm} u_{(2)}^{lm}(t,r)Y^{lm}(\theta,\phi), && (4.20)\\
A_\theta &= \sum_{lm}\frac{1}{l(l+1)}\{u_{(3)}^{lm}(t,r)\partial_\theta + u_{(4)}^{lm}(t,r)\frac{1}{\sin\theta}\partial_\phi\}Y^{lm}(\theta,\phi), && (4.21)\\
A_\phi &= \sum_{lm}\frac{1}{l(l+1)}\{u_{(3)}^{lm}(t,r)\partial_\phi - u_{(4)}^{lm}(t,r)\sin\theta\partial_\theta\}Y^{lm}(\theta,\phi), && (4.22)
\end{aligned}$$

and the corresponding covariant form

$$A^t = -\frac{1}{rf}\sum_{lm} u^{lm}_{(1)}(t,r)Y^{lm}(\theta,\phi), \tag{4.23}$$

$$A^r = \frac{1}{r}\sum_{lm} u^{lm}_{(2)}(t,r)Y^{lm}(\theta,\phi), \tag{4.24}$$

$$A^\theta = \sum_{lm}\frac{1}{r^2 l(l+1)}\left(u^{lm}_{(3)}(t,r)\partial_\theta Y^{lm}(\theta,\phi) + \frac{u^{lm}_{(4)}(t,r)}{\sin\theta}\partial_\phi Y^{lm}(\theta,\phi)\right), \tag{4.25}$$

$$A^\phi = \sum_{lm}\frac{1}{r^2 l(l+1)\sin^2\theta}\left(u^{lm}_{(3)}(t,r)\partial_\phi Y^{lm}(\theta,\phi) - u^{lm}_{(4)}(t,r)\sin\theta\partial_\theta Y^{lm}(\theta,\phi)\right). \tag{4.26}$$

To simplify the notations, we denote $u^{lm}_{(i)}(t,r)$ and $Y^{lm}(\theta,\phi)$ with $u^{lm}_{(i)}$ and Y^{lm} in the later sections. By substituting $\nu = t$ into the Eq. (4.12) and combining it with the non-vanishing Christoffel symbols, we start with considering the first two terms

$$\begin{aligned}
\nabla_\mu\nabla^\mu A^t - \mu^2 A^t &= g^{tt}\left(\partial_t^2 A^t + \Gamma^t{}_{tr}\partial_t A^r - \Gamma^r{}_{tt}\partial_r A^t\right) \\
&\quad + g^{rr}\left(\partial_r^2 A^t + \partial_r(\Gamma^t{}_{rt}A^t) - \Gamma^r{}_{rr}\partial_r A^t - \Gamma^r{}_{rr}\Gamma^t{}_{rt}A^t\right. \\
&\quad \left. + \Gamma^t{}_{rt}\partial_r A^t + \Gamma^t{}_{rt}\Gamma^t{}_{rt}A^t\right) \\
&\quad + g^{\theta\theta}\left(\partial_\theta^2 A^t - \Gamma^r{}_{\theta\theta}\partial_r A^t - \Gamma^r{}_{\theta\theta}\Gamma^t{}_{\theta t}A^t\right) \\
&\quad + g^{\phi\phi}\left(\partial_\phi^2 A^t - \Gamma^r{}_{\theta\theta}\partial_r A^t - \partial_\phi^\theta\partial_\theta A^t - \Gamma^r_{\phi\phi}\Gamma^t{}_{rt}A^t\right) - \mu^2 A^t.
\end{aligned} \tag{4.27}$$

Replacing the value of the non-vanishing Christoffel symbols, Eq. (4.2), then simplify Eq. (4.27) is simplified as

$$\begin{aligned}
\nabla_\mu\nabla^\mu A^t - \mu^2 A^t &= -\frac{1}{f}\partial_t^2 A^t - \frac{f'}{f^2}\partial_t A^r + \frac{1}{2}f'\partial_r A^t + f\partial_r^2 A^t + \frac{f''}{2}A^t + \frac{3}{2}f'\partial_r A^t \\
&\quad + \frac{f'}{r}A^t + \frac{1}{r^2}\partial_\theta^2 A^t + \frac{2}{r}f\partial_r A^t + \frac{1}{r^2}\cot\theta\partial_\theta A^t \\
&\quad + \frac{1}{r^2\sin^2\theta}\partial_\phi^2 A^t - \mu^2 A^t.
\end{aligned} \tag{4.28}$$

To separate the angular part of the vector potential components, out Eqs. (4.23) and (4.24) in Eq. (4.28), we have

$$\begin{aligned}\nabla_\mu\nabla^\mu A^t-\mu^2A^t &= -\frac{1}{f}\partial_t^2(-\frac{1}{rf}u^{lm}_{(1)}Y^{lm})-\frac{f'}{f^2}\partial_t(\frac{1}{r}u^{lm}_{(2)}Y^{lm})\\ &+\frac{1}{2}f'\partial_r(-\frac{1}{rf}u^{lm}_{(1)}Y^{lm})+f\partial_r^2(-\frac{1}{rf}u^{lm}_{(1)}Y^{lm})\\ &+\frac{2}{r}f\partial_r(-\frac{1}{rf}u^{lm}_{(1)}Y^{lm})+\frac{f''}{2}(-\frac{1}{rf}u^{lm}_{(1)}Y^{lm})\\ &+\frac{1}{r^2}\partial_\theta^2(-\frac{1}{rf}u^{lm}_{(1)}Y^{lm})+\frac{1}{r^2}\cot\theta\partial_\theta(-\frac{1}{rf}u^{lm}_{(1)}Y^{lm})\\ &+\frac{1}{r^2\sin^2\theta}\partial\phi^2(-\frac{1}{rf}u^{lm}_{(1)}Y^{lm})-\mu^2(-\frac{1}{rf}u^{lm}_{(1)}Y^{lm}).\\ &+\frac{3}{2}f'\partial_r(-\frac{1}{rf}u^{lm}_{(1)}Y^{lm})+\frac{f'}{r}(-\frac{1}{rf}u^{lm}_{(1)}Y^{lm}) \qquad (4.29)\end{aligned}$$

We can write the eigenvalue of the spherical harmonics as

$$(\frac{1}{r^2}\partial_\theta^2+\frac{1}{r^2}\cot\theta\partial_\theta+\frac{1}{r^2\sin^2\theta}\partial_\phi^2)Y^{lm}=-\frac{l(l+1)}{r^2}Y^{lm}. \qquad (4.30)$$

One may simplify Eq. (4.29) as

$$\begin{aligned}\nabla_\mu\nabla^\mu A^t-\mu^2A^t &= \Big[\frac{1}{rf}\frac{l(l+1)}{r^2}u^{lm}_{(1)}+\frac{\mu^2}{rf}u^{lm}_{(1)}+\frac{1}{rf^2}\partial_t^2u^{lm}_{(1)}-\frac{f'}{rf^2}\partial_tu^{lm}_{(2)}\\ &-\frac{f'}{2}(\partial_r\frac{1}{rf})u^{lm}_{(1)}-\frac{f'}{2rf}\partial_ru^{lm}_{(1)}-\frac{1}{r}\partial_r^2u^{lm}_{(1)}-2f(\partial_r\frac{1}{rf})\partial_ru^{lm}_{(1)}\\ &-f(\partial_r^2\frac{1}{rf})u^{lm}_{(1)}-\frac{3}{2}\frac{f'}{rf}\partial_ru^{lm}_{(1)}-\frac{3}{2}f'(\partial_r\frac{1}{rf})u^{lm}_{(1)}-\frac{2}{r^2f}f\partial_ru^{lm}_{(1)}\\ &-\frac{2}{r}f(\partial_r\frac{1}{rf})u^{lm}_{(1)}-\frac{f''}{2rf}u^{lm}_{(1)}-\frac{f'}{r^2f}u^{lm}_{(1)}\Big]Y^{lm}=0. \qquad (4.31)\end{aligned}$$

Multiping $(\frac{rf^2}{Y^{lm}})$ on Eq. (4.31), we have

$$\left(\partial_t^2-\partial_{r_*}^2+f\left(\frac{l(l+1)}{r^2}+\mu^2\right)\right)u^{lm}_{(1)}-f'\left(\dot{u}^{lm}_{(2)}-\partial_{r_*}u^{lm}_{(1)}\right)+\left(\frac{f''}{2}+\frac{f'}{r}\right)fu^{lm}_{(1)}=0, \qquad (4.32)$$

where $\dot{u}^{lm}_{(i)}=\frac{\partial u^{lm}_{(i)}}{\partial t}$. The tortoise coordinate r_* is defined via $dr_*=f^{-1}dr$. Next, we consider the third term in Eq. (4.12), ${R_t}^t$ is the only non-vanishing Ricci tensor in this case, as such

$$\begin{aligned}-{R_t}^tA^t &= -g^{tt}R_{tt}A^t\\ &= -\frac{1}{rf}\left(\frac{f''}{2}+\frac{f'}{r}\right)u^{lm}_{(1)}Y^{lm}. \qquad (4.33)\end{aligned}$$

Again, we multiply $(\frac{rf^2}{Y^{lm}})$ and put it back to Eq. (4.12), together with Eq. (4.32), the last term of Eq. (4.32) cancels out. Then, we set radial equation for $\nu = t$

$$\left(-\partial_t^2 + \partial_{r_*}^2 - f\left(\frac{l(l+1)}{r^2} + \mu^2\right)\right) u^{lm}_{(1)} + f'\left(\dot{u}^{lm}_{(2)} - \partial_{r_*} u^{lm}_{(1)}\right) = 0. \tag{4.34}$$

For the other parts $\nu = \{r, \theta, \phi\}$, one can follow a similar calculation as in (Appendix APPENDIX A). As a remark, to solve the radial equations for $\nu = \theta$ and ϕ, it is more convenient to assume the linear-combination as

$$(\partial_\theta + \cot\theta) \times (\nu = \theta) + \partial_\phi (\nu = \phi) = 0, \tag{4.35}$$

$$(2\cos\theta + \sin\theta\partial_\theta) \times (\nu = \phi) - \frac{1}{\sin\theta}\partial_\phi (\nu = \theta) = 0, \tag{4.36}$$

the details also presented in Appendix APPENDIX A .

Therefore, the radial equation for general static spherically symmetric black holes spacetimes can be written as

$$\left[-\partial_t^2 + \partial_{r_*}^2 - f\left(\frac{l(l+1)}{r^2} + \mu^2\right)\right] u^{lm}_{(1)} + f'(\dot{u}^{lm}_{(2)} - \partial_{r_*} u^{lm}_{(1)}) = 0, \tag{4.37}$$

$$\left[-\partial_t^2 + \partial_{r_*}^2 - f[\frac{l(l+1)}{r^2} + \mu^2]\right] u^{lm}_{(2)} + f'\left(\dot{u}_1 - \partial_{r_*} u^{lm}_{(2)}\right) - \frac{2f^2}{r^2}\left(u^{lm}_{(2)} - u^{lm}_{(3)}\right) = 0, \tag{4.38}$$

$$\left[-\partial_t^2 + \partial_{r_*}^2 - f\left(\frac{l(l+1)}{r^2} + \mu^2\right)\right] u^{lm}_{(3)} + \frac{2f}{r^2} l(l+1) u^{lm}_{(2)} = 0, \tag{4.39}$$

$$\left[-\partial_t^2 + \partial_{r_*}^2 - f\left(\frac{l(l+1)}{r^2} + \mu^2\right)\right] u^{lm}_{(4)} = 0. \tag{4.40}$$

We obtain Eqs. (4.37)-(4.40), which agree with thse derive in [9], in which Eq. (4.40) describes the odd-parity sector, and the Eqs. (4.37)-(4.39) describe the even-parity modes. The even-parity equations are coupled between $u_{(1)}, u_{(2)}$ and $u_{(3)}$, which cannot simplify to the Reege-wheeler form for the Proca field (massive vector field) [13]. In the later sections, we will introduce the Frolov-Krotous-Kubiznak ansatz for simplifying these coupled equations.

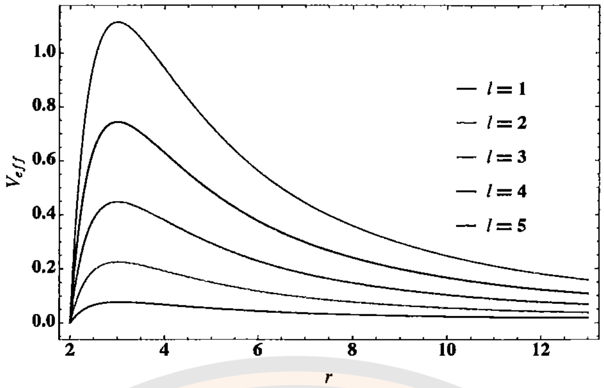

Figure 3 **The effective potential of odd-parity mode when $\mu = 0.1$ and variation l.**

4.2.1 Radial equation of odd- parity

Firstly, for the odd-parity modes in Eq. (4.40), we consider $u_4(t,r) = u_{\text{odd}}(r)e^{-i\omega t}$ in odd-parity radial equation, where ω represents the energy parameter for massive spin-1 particles. This configuration leads to the derivation of the radial equation.

$$\left[\partial^2_{r_*} + \omega^2 - f\left(\frac{l(l+1)}{r^2} + \mu^2\right)\right] u_{odd}(r) = 0, \tag{4.41}$$

for this radial equation, the effective potential can written as

$$V_{eff(odd)} = f\left(\frac{l(l+1)}{r^2} + \mu^2\right). \tag{4.42}$$

In the massless case of this mode, Eq.(4.41) reduces to the vector form of the Regge–Wheeler equation. In Fig. 3, We shown the variations of the potential for the Proca field for odd-pariy mode with different angular momentum quantum numbers, $l = 1 \rightarrow 5$. The horizontal axis shows the radial distance r, while the vertical axis represents the effective potential profile V_{eff}. As the angular momentum l increases, the height of the potential barrier also increases, which implies that waves with large l are more likely to be reflected and less likely to be absorbed by the black hole.

Furthermore, we examine the shape of the effective potential for the odd-parity mode with different Proca masses in Fig. 4. The shape of the potential

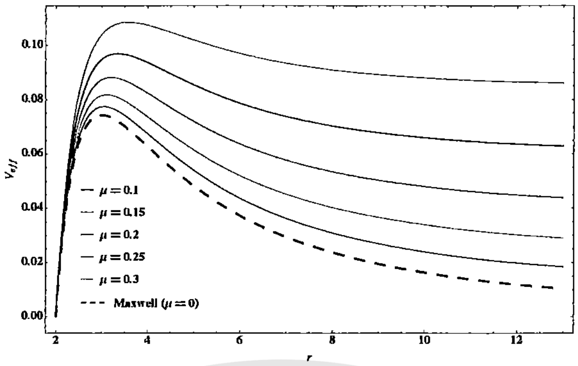

Figure 4 **The effective potential of odd-parity mode when $l = 1$ and variation μ.**

barrier increases as the Proca mass increases. We compare these results with the massless case (Maxwell's field). The massless case has a lower peak and a different overall shape, indicating that massless fields encounter a weaker potential barrier, represented by the dashed line in the figure. In the next chapter, we will investigate the greybody factor for this mode, by using the rigorous bound and WKB method.

In the next section, we explore an alternative method for reducing the even-parity radial equation to a single equation describing the even-parity mode.

4.3 The even-parity mode

4.3.1 Frolov–Krtouš–Kubizňák–Santos (FKKS) separation and transformation

In our prior investigation, we examine the odd-parity mode of radial equation Eq. (4.40), taking consideration into the pertinent Eqs. (4.37)-(4.39) shall naturally be the process of exploring the even-parity modes for massless case. We observed that the system of equations involving the functions $u_{(2)}$ and $u_{(3)}$ can be decoupled. This technique was previously demonstrated in the case of the Schwarzschild black hole (see [13] for details). The basic idea is to express $u_{(2)}$ in terms of $u_{(3)}$, substitute it back into the radial equation $u_{(3)}$. Although this method simplifies even-parity radial equations, it leads to a more mathematically complex equation, specifically, a higher-order partial differential equation.

However, for the massive case, this approach is not suitable because the radial equation included a mass parameter μ that makes an analytical decoupling fails.

To solve the decoupled problems, we need to introduce the Frolov–Krtouš–Kubizňák–Santos (FKKS) method, which separates the radial and angular equations of the spin-1 field from the equations of motion in a general higher-dimensional Kerr–NUT–(A)dS black hole spacetime. The process was initiated by employing a novel ansatz equation for separate variables done in 2018 [10][31]. In this work, we consider the Proca field in the Schwarzschild spacetime, which arises as a special case of the fully general Kerr–NUT–(A)dS black hole. The relation may obtained by setting all rotational parameters and NUT charges to zero and vanishing the cosmological constant. The standard Schwarzschild form is thus the simplest representative of the broader FKKS class, illustrating how rotating or NUT-charged solutions collapse to a static, spherically symmetric black hole when all additional parameters vanish.

The FKKS framework provides a way to decouple the even-parity equations for the massive field, and the transformation between the functions $u_{(i)}^{lm}$ from the VSH formalism to the FKKS approach was given by [12] and [13]. The function $u_{(i)}^{lm}$ for the FKKS method can thus be written as follows

$$\begin{aligned} u_{(1)}^{lm}(r) &= -\frac{ifr(\nu r\partial_r + \omega/f)R}{q_r}, && (4.43) \\ u_{(2)}^{lm}(r) &= \frac{fr(\partial_r - \omega\nu r/f)R}{q_r}, && (4.44) \\ u_{(3)}^{lm}(r) &= \Lambda R, && (4.45) \\ u_{(4)}^{lm}(r) &= 0, && (4.46) \end{aligned}$$

where $\Lambda = \mu^2/\nu^2 - \omega/\nu = l(l+1)$, $q_r = 1 + \nu^2 r^2$, and $R = R(r)$ is radial function.

Note that the relation of $\mu^2/\nu^2 - \omega/\nu = l(l+1)$ is introduced by matching the angular equation in Kerr-like spacetimes to the spherical harmonic in the static limit. We obtain two possible value for ν, which are

$$\nu = \frac{-\omega}{l(l+1)} \frac{1 \pm \sqrt{1+4l(l+1)\mu^2/\omega^2}}{2}. \tag{4.47}$$

The lower sign corresponds to the even-parity scalar mode, and the upper sign corresponds to the even-parity vector mode. Taking the massless limit of Eq. 4.47, the value for ν reduces to $\nu_0 = -\frac{\omega}{l(l+1)}$. In summary, the relation between VSH and FKKS separation methods is given by the transformation of the wave function in Eqs. (4.43)-(4.46). In later subsections, we will write down the radial equation and check the consistency of the even-parity mode.

4.3.2 Radial equation from Eq. (4.39)

Firstly, we consider Eq. (4.39), which involves terms $u^{lm}_{(2)}$ and $u^{lm}_{(3)}$. By substituting Eq. (4.44) and Eq. (4.45) into radial equations Eq. (4.39) we have

$$\begin{aligned} \hat{\mathcal{D}} u^{lm}_{(3)} + \frac{2f}{r^2} l(l+1) u^{lm}_{(2)} &= 0, \\ \Rightarrow l(l+1)\hat{\mathcal{D}} R + \frac{2f}{r^2} l(l+1) \left[\frac{fr(\partial_r - \omega\nu r/f)R}{q_r} \right] &= 0, \\ \Rightarrow \hat{\mathcal{D}} R + \frac{2f}{rq_r}\partial_{r_*} R - \frac{2f\omega\nu}{q_r} R &= 0, \end{aligned} \tag{4.48}$$

where $\hat{\mathcal{D}} = \left(-\partial_t^2 + \partial_{r_*} - f\left(\frac{l(l+1)}{r^2} + \mu^2\right)\right)$. To provide further clarification, when substituting "$R(r)$" into the differential operator $\hat{\mathcal{D}}$, we obtain the following expressions

$$\partial^2_{r_*} R + \left(\omega^2 - f\left(\frac{l(l+1)}{r^2} + \mu^2\right)\right) R + \frac{2f}{rq_r}\partial_{r_*} R - \frac{2f\omega\nu}{q_r} R = 0. \tag{4.49}$$

This equation is identified as the Radial equation and shares resemblances with the Regge-Wheeler equation, a foundational element in our research. This is important to emphasize in our work.

4.3.3 Consistency of Eqs. (4.37) and (4.38)

From the previous section, we obtain the radial equation Eq. (4.37) from Eq. (4.38) only. Therefore, the consistency checking for Eqs. (4.37) and (4.38) are necessarily, To consider Eq.({Ra1}), we start by imposing the Lorenz condition $-\dot{u}^{lm}_{(1)} + \partial r_* u_2 + \frac{f}{r}\left(u^{lm}_{(2)} - u^{lm}_{(3)}\right) = 0$ to Eq. (4.37) reduce $u^{lm}_{(3)}$ as

$$\hat{\mathcal{D}} u^{lm}_{(2)} + \left(f' - \frac{2f}{r}\right)\left(\dot{u}^{lm}_{(1)} - \partial r_* u^{lm}_{(2)}\right) = 0. \tag{4.50}$$

Now, Eqs. (4.37)and (4.50) are coupled radial equations with $u_1$andu_2 only.

We substitu Eqs. 4.43 and 4.44 in Eq. (4.37), we obtain

$$\begin{aligned}
&\Bigg(-\frac{8ir^3\nu^4\omega f^2}{(1+r^2\nu^2)^3} + \frac{6ir\nu^2\omega f^2}{(1+r^2\nu^2)^2} + \frac{ir^2\nu\omega^2 f'}{1+r^2\nu^2}\Bigg) + \Bigg(\frac{4ir^2\nu^2\omega f^2}{(1+r^2\nu^2)^2}\\
&+\frac{2i\omega f^2}{1+r^2\nu^2} - \frac{8ir^4\nu^5 f^3}{(1+r^2\nu^2)^3} + \frac{10ir^2\nu^3 f^3}{(1+r^2\nu^2)^2} - \frac{2i\nu f^3}{1+r^2\nu^2} - \frac{ir\omega f f'}{1+r^2\nu^2}\\
&+\frac{4ir^3\nu^3 f^2 f'}{(1+r^2\nu^2)^2} - \frac{4ir\nu f^2 f'}{1+r^2\nu^2} - \frac{ir^2\nu f^2 f''}{1+r^2\nu^2}\Bigg) R'\\
&+\Bigg(-\frac{ir\omega f^2}{1+r^2\nu^2} + \frac{4ir^3\nu^3 f^3}{(1+r^2\nu^2)^2} - \frac{4ir\nu f^3}{1+r^2\nu^2} - \frac{2ir^2\nu f^2 f'}{1+r^2\nu^2}\Bigg) R''\\
&-\frac{ir^2\nu f^3}{1+r^2\nu^2} R''' + \left(\omega^2 - f\frac{l(l+1)}{r^2} + \mu^2\right)\left(-\frac{ifr(\nu r\partial_r + \omega/r)}{q_r}\right) R = 0.
\end{aligned} \tag{4.51}$$

Similarly, upon substituting the wave function into Eq. (4.50), we obtain

$$\begin{aligned}
&\Bigg(-\frac{8r^4\nu^5\omega f^2}{(1+r^2\nu^2)^3} + \frac{10r^2\nu^3\omega f^2}{(1+r^2\nu^2)^2} - \frac{2\nu\omega f^2}{1+r^2\nu^2} + \frac{2r^3\nu^3\omega f f'}{(1+r^2\nu^2)^2}\\
&-\frac{2r\nu\omega f f'}{1+r^2\nu^2} - \frac{r\omega^2\left(-\frac{2f}{r}+f'\right)}{1+r^2\nu^2} - \frac{2r^3\nu^3\omega f\left(-\frac{2f}{r}+f'\right)}{(1+r^2\nu^2)^2} + \frac{2r\nu\omega f\left(-\frac{2f}{r}+f'\right)}{1+r^2\nu^2}\Bigg) R\\
&+\Bigg(\frac{4r^3\nu^3\omega f^2}{(1+r^2\nu^2)^2} - \frac{4r\nu\omega f^2}{1+r^2\nu^2} + \frac{8r^3\nu^4 f^3}{(1+r^2\nu^2)^3} - \frac{6r\nu^2 f^3}{(1+r^2\nu^2)^2}\\
&-\frac{r^2\nu\omega f f'}{1+r^2\nu^2} - \frac{6r^2\nu^2 f^2 f'}{(1+r^2\nu^2)^2} + \frac{3f^2 f'}{1+r^2\nu^2} + \frac{r f f'^2}{1+r^2\nu^2}\\
&+\frac{2r^2\nu^2 f^2\left(-\frac{2f}{r}+f'\right)}{(1+r^2\nu^2)^2} - \frac{f^2\left(-\frac{2f}{r}+f'\right)}{1+r^2\nu^2} - \frac{r f f'\left(-\frac{2f}{r}+f'\right)}{1+r^2\nu^2} + \frac{r f^2 f''}{1+r^2\nu^2}\Bigg) R'\\
&+\Bigg(-\frac{r^2\nu\omega f^2}{1+r^2\nu^2} - \frac{4r^2\nu^2 f^3}{(1+r^2\nu^2)^2} + \frac{2f^3}{1+r^2\nu^2} + \frac{3r f^2 f'}{1+r^2\nu^2} - \frac{r f^2\left(-\frac{2f}{r}+f'\right)}{1+r^2\nu^2}\Bigg) R''\\
&+\frac{r f^3}{1+r^2\nu^2} R''' + \left(\omega^2 - f\frac{l(l+1)}{r^2} + \mu^2\right)\left(\frac{fr\left((\partial_r - \omega\nu r/f)\right)}{q_r}\right) R = 0.
\end{aligned} \tag{4.52}$$

In our analysis of the first two radial equations for even-parity, a third-order derivative emerged. However, considering the Regge-Wheeler equation does not involve third derivatives, we rectify this incongruity by implementing a judicious linear combination between Eqs. (4.37 and 4.50) or Eqs. (4.51and (4.52) as follows

$$\frac{1}{ir\omega} \times \left(\left(\hat{\mathcal{D}} u^{lm}_{(1)} + f' \left(\dot{u}^{lm}_{(2)} - \partial_{r_*} u^{lm}_{(1)} \right) \right) \right.$$
$$\left. + i\nu r \left(\hat{\mathcal{D}} u^{lm}_{(3)} + \left(f' - \frac{2f}{r} \right) \left(\dot{u}^{lm}_{(1)} - \partial_{r_*} u^{lm}_{(2)} \right) \right) = 0, \quad (4.53)\right.$$

$$\left(\frac{2r\nu\omega f}{r + r^3\nu^2} \right) R - \frac{r(1 + r^2\nu^2)f^2}{r + r^3\nu^2} R'' - \frac{f(2f + r(1 + r^2\nu^2)\frac{\partial f}{\partial r})}{r + r^3\nu^2} R' = 0. \qquad (4.54)$$

By simplifying this equation and incorporating the operator "$\hat{\mathcal{D}}$", we obtain:

$$\partial^2_{r_*} R + \left(\omega^2 - f \left(\frac{l(l+1)}{r^2} + \mu^2 \right) \right) R + \frac{2f}{rq_r} \partial_{r_*} R - \frac{2f\omega\nu}{q_r} R = 0. \qquad (4.55)$$

This equation takes the same form as Eq. (4.49), which means the radial equation of even-parity Eqs. (4.37)-(4.39) are consistent. In the next subsection, we will show the details for reducing the radial equations of even-parity to a single radial equation.

4.3.4 Reducing the radial equation

In the previous subsection, we established the transformation and check the consistency of Eqs. (4.37)-(4.39), and now the coupled even-parity radial equations are reduced to a single one. The radial equation in this form already allows us to study the greybody factor, however, one may notice that a first-order partial derivative term in Eq. (4.55) prevents the radial equation from being in the Schrödinger-like form. For convenience to our later studies, a further simplification on Eq. (4.55) to a Schrödinger-like form will be presented in this sub-section. To do this, the solution for the radial function, denoted as "R(r)" is assumed to be expressed as $R(r) = A\bar{R}$, where "A" and "$\bar{R}$" are functions of "r". By substituting this into Eq. (4.55), we obtain the following expressions

$$[\partial^2_{r_*} A\bar{R} + 2\left(\partial r_* A\right)\left(\partial_{r_*}\bar{R}\right) + A(\partial^2_{r_*}\bar{R})] + \left(\omega^2 - f\left(\frac{l(l+1)}{r} + \mu^2\right)\right)(A\bar{R}) \\ + \frac{2f}{rq_r}\left[(\partial_{r_*}A)\bar{R} + A\partial_{r_*}\bar{R}\right] - \frac{2f\omega\nu}{q_r}(A\bar{R}) = 0. \quad (4.56)$$

To fit the Schrödinger-like form, we require that the $2\left(\partial_{r_*}A\right)\left(\partial_{r_*}\bar{R}\right)$ and $\frac{2f}{rq_r}A\left(\partial_{r_*}\bar{R}\right)$, must be mutually cancel out. Ths leads to

$$(\partial_{r_*}A) + \frac{f}{rq_r}A = 0, \quad (4.57)$$

Subsequently, the radial equation becomes:

$$(A)\bar{R} + A\bar{R} + \left(\omega^2 - f\left(\frac{l(l+1)}{r} + \mu^2\right)\right)A\bar{R} + \frac{2f}{rq_r}(A)\bar{R} - \frac{2f\omega\nu}{q_r}A\bar{R} = 0. \quad (4.58)$$

From Eq. 4.57, we can deduce the solution for the function "A" as

$$A = \exp\left(-\int dr\frac{1}{rq_r}\right). \quad (4.59)$$

Furthermore, we may simplify Eq. (4.58) by following relations

$$\begin{aligned} \frac{\partial_{r_*}A}{A} &= -\frac{f}{rq_r}, \\ \frac{1}{A}\partial_{r_*}\left(\partial_{r_*}A\right) &= \partial_{r_*}\left(-\frac{f}{rq_r}A\right), \\ &= \frac{1}{A}\left(\frac{Af^2}{r^2q_r} - \frac{f^2\partial_r A}{rq_r} - \frac{Aff'}{rq_r} + \frac{Af^2q_r'}{rq_r^2}\right), \\ &= -\left(\frac{f}{rq_r}\right) + \left(\frac{f}{rq_r}\right)^2. \end{aligned} \quad (4.60)$$

Ultimately, we arrive at the radial equation that will be utilized for even parity calculations

$$\left[\partial^2_{r_*} + \omega^2 - \left(f\left(\frac{l(l+1)}{r^2} + \mu^2\right) + \left(\partial_{r_*}\frac{f}{rq_r}\right) + \left(\frac{f}{rq_r}\right)^2 + \frac{2f\omega\nu}{q_r}\right)\right]\bar{R} = 0.$$

Therefore, the effective potential of the even-parity can be written as

$$V_{eff(even)} = f\left(\frac{l(l+1)}{r^2} + \mu^2\right) + \partial_{r_*}\left(\frac{f}{rq_r}\right) + \left(\frac{f}{rq_r}\right)^2 + \frac{2f\omega\nu}{q_r}. \quad (4.61)$$

This effective potential includes the two modes of even-parity from the parameter ν , which correspond to the scalar mode and vector mode from Eq. (4.47). This equation represents the single radial equation for even parity and can be used to calculate the greybody factor in the subsequent chapter.

4.3.5 The radial equations of even-parity scalar mode

From the previous section, we investigate the single radial equation for even-parity mode. The radial equation of even-parity scalar mode as

$$\left[\partial_{r_*}^2 + \omega^2 - \left(f\left(\frac{l(l+1)}{r^2} + \mu^2\right) + \partial_{r_*}\left(\frac{f}{rq_r}\right) + \left(\frac{f}{rq_r}\right)^2 + \frac{2f\omega\nu_-}{q_r}\right)\right]\bar{R} = 0, \tag{4.62}$$

where $\nu_- = \frac{-\omega}{l(l+1)}\left(\frac{1-\sqrt{1+4l(l+1)\mu^2/\omega^2}}{2}\right)$. We examine the effective potential in this scenario by considering the radial equation in Fig. 5.

For checking the behavior of the effective potential, we take $f = 1 - \frac{2}{r}$, which is the metric function of the Schwarzchild black hole with unit black hole mass $M = 1$. Next, this effective potential depends on the value of ω, it is difficult to plot the exact potential without specifying ω and plotting the potential for each specific value as shown in Fig. 5. The effective potential for the even-parity scalar modes is similar to the odd-parity modes when ω is fixed. The potential also rises with an increasing in angular momentum l , where it is shown from the plot in Fig. 5a. This behavior shows that higher angular momentum states correspond to a higher potential barrier. As the mass μ of the Proca particle increases, the effective potential also increases, as shown in Fig. 5b. This appears that more massive Proca fields will given a higher potential barrier, which can influence the dynamics of the field around the black hole, this affects the transmission and reflection properties of the waves associated with these fields as shown in the next chapter.

4.3.6 The radial equations of even-parity vector mode

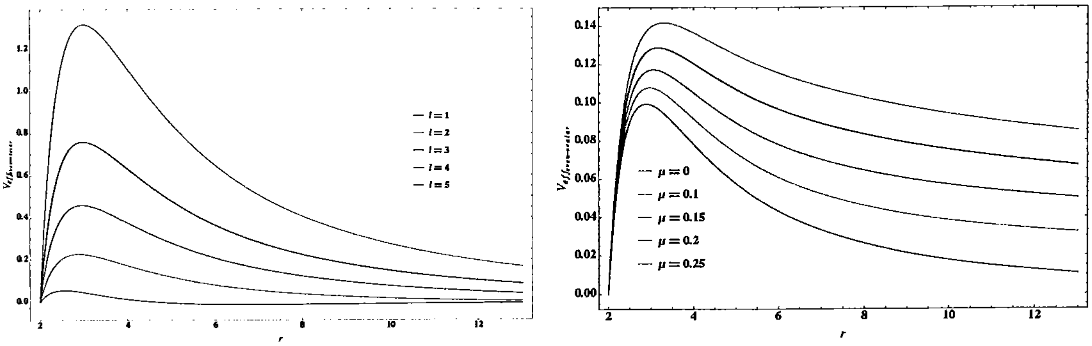

(a) (b)

Figure 5 (a). The effective potential for the even-parity scalar modes with $\omega = 0.4$, $\mu = 0.1$, and variation l. (b). The effective potential for the even-parity scalar modes with $\omega = 0.4$, $l = 1$ and variation μ.

The effective potential in this scenario is

$$V_{eff_{even-vector}} = f(r)\left(\frac{l(l+1)}{r^2} + \mu^2\right) + \partial_{r_*}\left(\frac{f}{rq_r}\right) + \left(\frac{f(r)}{rq_r}\right)^2 + \frac{2f(r)\omega\nu_+}{q_r}, \quad (4.63)$$

where $\nu_+ = \frac{-\omega}{l(l+1)}\left(\frac{1+\sqrt{1+4l(l+1)\mu^2/\omega^2}}{2}\right)$. Similar to the even-parity scalar case, this potential depends on the value of ω. The effective potential is plotted for different values of l in Fig. 6a, also higher with an increase in μ as shown in Fig. 6b with setting $f = 1 - \frac{2}{r}$.

For the even-parity vector mode, as the Proca mass increases, the effective potential initially decreases. However, beyond a certain value, the trend reverses, causing the effective potential to increase instead, as shown in Fig. 7 when $l = 1$ and $\omega = 0.15$. Specifically, when the Proca mass increases from 0.1 to 0.2, the peak of the effective potential tends to decrease. However, once the mass of Proca particle exceeds 0.2, the effective potential begins to increase instead.

To summeris this chapter, we presented the VSH method for separating the equation of motion of Proca field in spherically symmetric black hole spqcetimes, and the transformation betwwen VSH and FKKS to decoupled the equations were

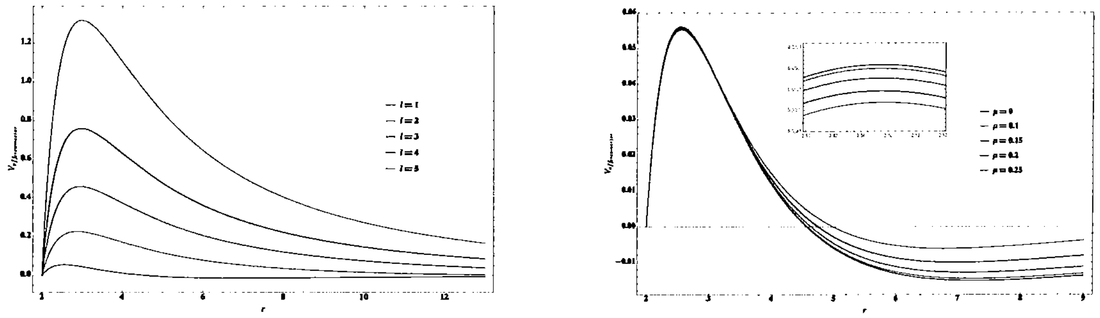

(a) (b)

Figure 6 **(a). The effective potential for the even-parity vector modes with $\omega = 0.4$, $\mu = 0.1$, and variation l. (b). The effective potential for the even-vector modes with $\omega = 0.4$, $= 1$ and variation μ.**

obtained, the even-parity scalar, even-parity vector, and odd-parity equation, which shall be our master equations in the later studies.

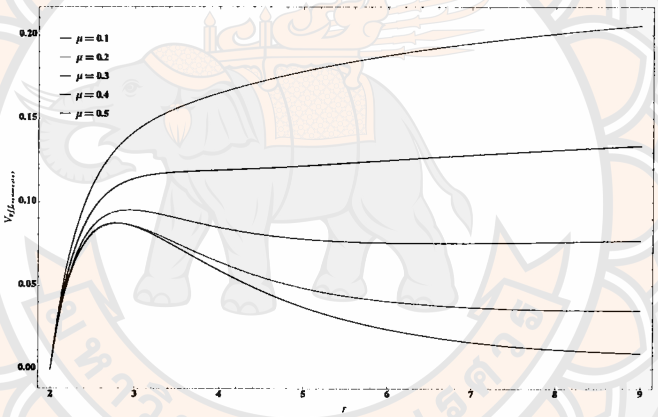

t!

Figure 7 The effective potential for the even-parity vector mode with $\omega = 0.15$, $l = 1$ and variation μ.

CHAPTER V

RIGOROUS BOUND

In this chapter, we analyze the greybody factor by determining Rigorous Bounds techniques for both odd-parity and even-parity modes. The odd-parity modes represent distinct types of radial equations within the Proca field in the Schwarzschild background, and the formulation of an even-parity mode involves a system of coupled equations. To simplify this, we utilize the LFKK ansatz to unify the radial equations of the even-parity mode into a single Schrödinger-like form. Subsequently, we employ this equation to compute the greybody factor for the specific case presented in this chapter.

5.1 The rigorous bound for odd-parity and monopole mode

In this section, our primary focus is on two distinct cases the odd-parity and monopole modes. The radial equation of these modes is fully decoupled in the Regge-Wheeler form. Subsequently, we can utilize the potential derived in the previous chapter to establish the rigorous bounds. The results in this section are based on our conference proceeding in 2023 [22].

5.1.1 The greybody for odd-parity mode

From the previous chapter, we investigate the radial equation for odd-parity mode as

$$\left[\partial_{r_*}^2 + \omega^2 - f\left(\frac{l(l+1)}{r^2} + \mu^2\right)\right] u_{odd}(r) = 0, \tag{5.1}$$

for this radial equation, the effective potential can be written as

$$V_{eff(odd)} = f\left(\frac{l(l+1)}{r^2} + \mu^2\right). \tag{5.2}$$

The rigorous bound method as we described in the previous chapter can be summarized as

$$T \geq \operatorname{sech}^2 \int_{-\infty}^{\infty} \frac{\sqrt{[\partial_{r_*} h(r_*)]^2 + [\omega^2 - V_{eff(odd)}(r_*) - h^2(r_*)]^2}}{2h(r_*)} dr_*, \tag{5.3}$$

In this scenario, we select the function $h = \sqrt{\omega^2 - f\mu^2}$ for the odd-parity modes. The function here does not follow the standard form of the rigorous bound presented in the previous chapter because the mass parameter "μ" dominated the behavior of the effective potential at the spatial infinity. Therefore, the integration diverges with non-vanishing "μ". The mass squared term in the h function would converge our result, however, the choice of h function must satisfy the small mass condition $h(-\infty) = h(\infty) \sim \omega$, and the effective area requires $\omega^2 > \mu^2$. By evaluating the integral in Eq. (5.3), it can be expressed as

$$\begin{aligned} T \geq \operatorname{sech}^2 \Bigg(& \frac{1}{2l(1+l)(-2+r)\mu^2 \sqrt{1 + \frac{r\mu^4}{l^2(1+l)^2(-((-2+r)\mu^2)+r\omega^2)}}} \\ & \times \left[r^3 \sqrt{\frac{(-2+r)^2 \left(l^2(1+l)^2 + \frac{r\mu^4}{-((-2+r)\mu^2)+r\omega^2} \right)}{r^6}} \right. \\ & \times \left(-l(1+l)\sqrt{(-1+\frac{2}{r})\mu^2 + \omega^2} \sqrt{1 + \frac{r\mu^4}{l^2(1+l)^2(-((-2+r)\mu^2)+r\omega^2)}} \right) \\ & \left. + \mu^2 \operatorname{ArcCsch}\left(\frac{l(1+l)\sqrt{(-1+\frac{2}{r})\mu^2+\omega^2}}{\mu^2} \right) \right] \Bigg|_2^{\infty} \Bigg) \end{aligned} \tag{5.4}$$

By substituting the integration limits into Eq. (5.4), we find that the integral becomes undefined at $r = 2$ due to the expression becoming indeterminate. Therefore, we resort to numerical integration to evaluate it.

The greybody factor of this mode is presented in Fig. 8 and Fig. 10. In Fig. 8 we show the results of the greybody factor for the odd-parity mode with "$\mu = 0.1$" for varying l. The trend of transmission probability decreases when "l" increases (the graph shifts to the right). This result is consistent with the trend of effective potential as we shown in Fig. 3. In Fig. 9 and Fig. 10, we present comparisons of the effective potential and the rigorous bound between massless

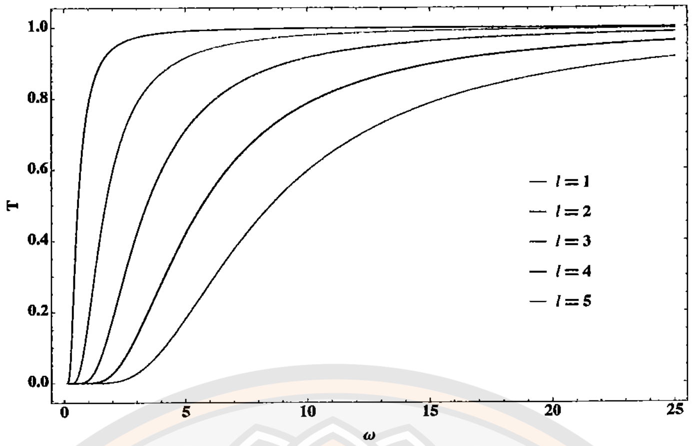

Figure 8 The rigorous bound of the greybody factor for the odd-parity mode with $\mu = 0.1$ and variation l.

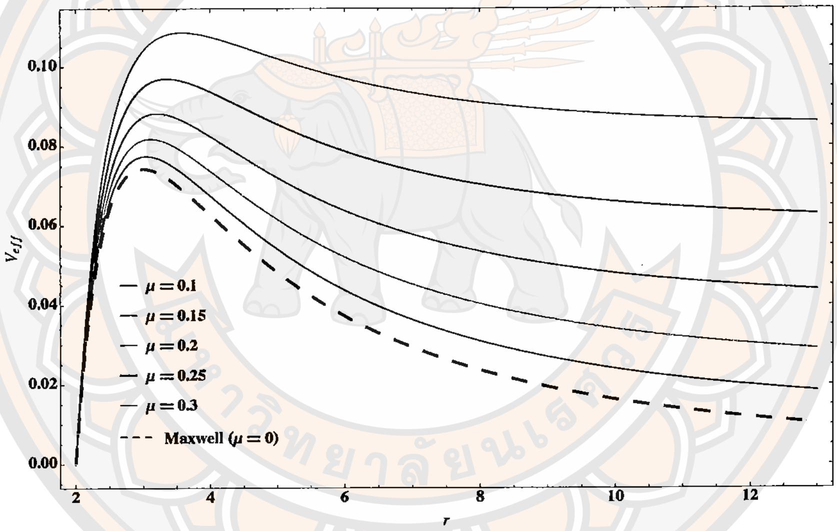

Figure 9 The effective potential of odd-parity mode compared with massless vector field case with fixed $l = 1$.

spin-1 and Proca fields, where the dash line represents the massless spin-1 field. In these comparisons, we take "$l = 1$" and vary "μ". We find that the Proca field exhibits a similar behavior of effective potential with massless spin-1 field, and with "μ" increase, the maximum of the effective potential increase as in Fig. 8. Moreover, we obtain the greybody factor of the massless spin-1 field as

$$T \geq \operatorname{sech}^2 \int_{-\infty}^{\infty} \frac{f\left(l(l+1)\right)}{2r^2\omega} dr_*, \tag{5.5}$$

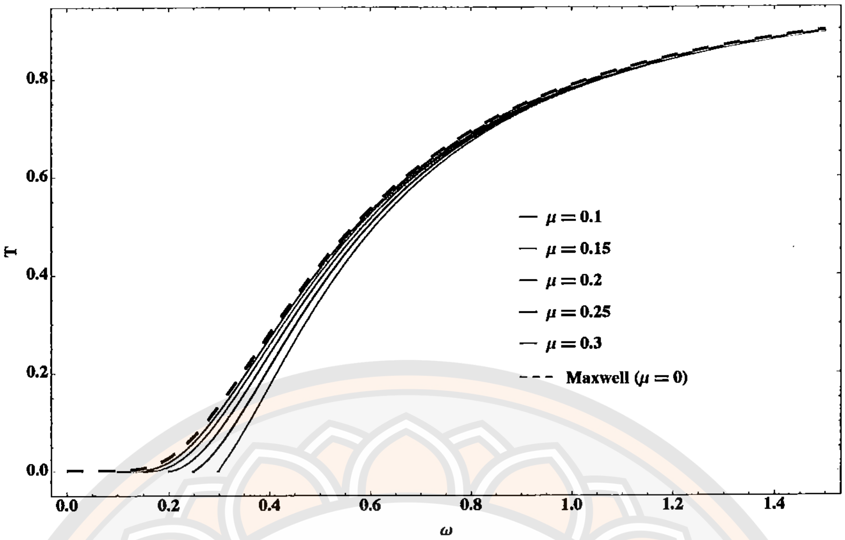

Figure 10 **The rigorous bound of the greybody factor for the odd-parity mode with $l = 1$ and variation μ, comparison with Maxwell's case.**

where the function of h for massless spin-1 field is defined as $h(r) = \sqrt{\omega^2}$.

In Fig. 10, we present the result for fixing $l = 1$ and variation μ, and the massless spin-1 field (dash line) is also depicted. The massless limit of the Proca field can be reduced to the massless spin-1 field (Maxwell's field), and with "μ" increase, the rigorous bound decreases and shifts to the right-hand side.

5.1.2 The greybody factor of monopole mode

For the monopole modes, we impose the conditions $u_3(t,r) = 0$, $l = 0$, and $u_2(t,r) = u_m(r)e^{-i\omega t}$ to Eqs. (4.37)-(4.39). The Lorenz condition implies that $\dot{u_{(1)}} = \frac{f}{r}\partial_r = \left(ru_{(2)}\right)$ .Using this relation, the even-parity Proca equations can be simplified into a single radial equation governing the monopole mode (see in [7])

$$\left[\partial^2_{r_*} + \omega^2 - f\left(\frac{2\,(r-3)}{r^3} + \mu^2\right)\right] u_{lm}(r) = 0. \tag{5.6}$$

The effective potential is expressed as

$$V_{eff(mono)} = f\left(\frac{2\,(r-3)}{r^3} + \mu^2\right). \tag{5.7}$$

In addition, we consider the monopole mode for massive scalar cases as

$$V_{massivescalar} = f\left(\frac{2}{r^3} + \mu^2\right). \tag{5.8}$$

The graph in Fig. 11 depicts the form of the effective potential corresponding

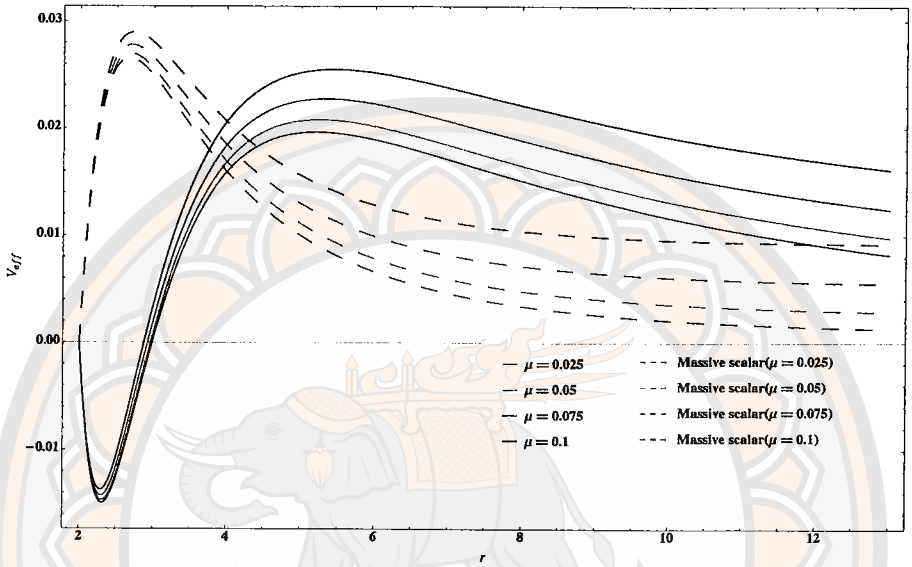

Figure 11 The effective potential of monopole mode and comparison with massive scalar with $l = 0$.

to the monopole mode with a massive scalar and Proca fields when $l = 0$. The shapes of the effective potential in both cases differ significantly, which is due to the theoretical differences between vector and scalar fields. However, both exhibit similar potential barriers and as the particle's mass increases, the potential barrier height also increases. Similar to the approach for odd-parity modes, we can derive the greybody factor as follows

$$T \geq \operatorname{sech}^2 \int_{-\infty}^{\infty} \frac{\sqrt{[\partial_{r_*} h]^2 + [\omega^2 - V_{eff(odd)} - h^2]^2}}{2h} dr_*, \tag{5.9}$$

in this scenario, we choose the "h" function as $h(r) = \sqrt{\omega^2 - f\mu^2}$.

In Fig. 12, we present the comparisons for the rigorous bound of the Proca field with the massive scalar field for the monopole mode, depicted with solid lines and dashed lines respectively. We found that the transmission amplitude for the

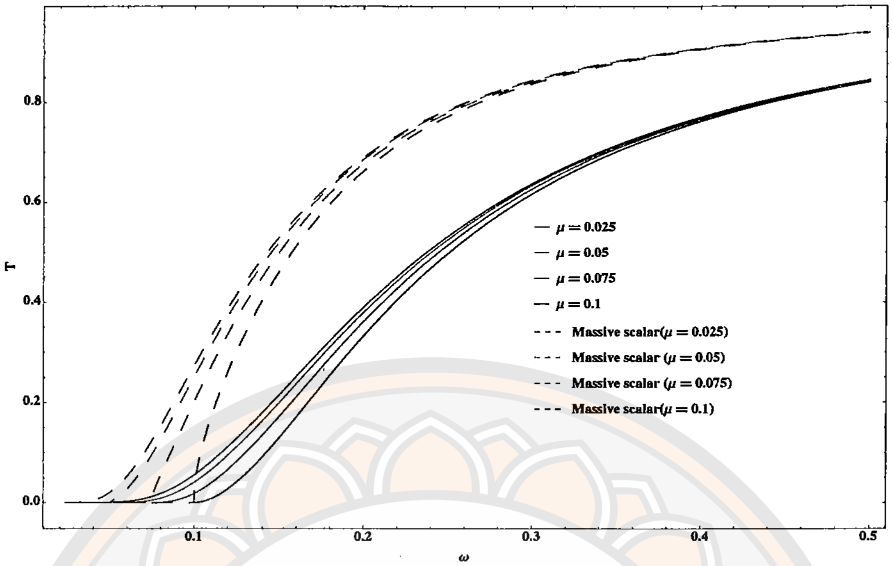

Figure 12 **The rigorous bound of the greybody factor for monopole mode and comparison with massive scalar case.**

monopoly mode of a massive scalar differs from the one of the Proca field. The transmission probability of the monopole mode of the massive scalar perturbation is higher than the monopole mode of the massive vector field in general, and with "μ" increase, both of them shift to the right-hand side.

5.2 The rigorous bound for even-parity.

In previous chapters, the unified radial equation for the even-parity case is expressed as follows

$$\left[\partial^2_{r_*} + \left(\omega^2 - V(r) - \left(\frac{2f\omega\nu}{q_r} + (\partial_{r_*}\frac{f}{rq_r}) + (\frac{f}{rq_r})^2\right)\right)\right]\bar{R} = 0, \tag{5.10}$$

then the effective potential of even parity can be written as

$$V_{eff-even} = f\left(\frac{l\,(l+1)}{r^2} + \mu^2\right) + \left(\frac{2f\omega\nu}{q_r} + \partial_{r_*}(\frac{f}{rq_r}) + (\frac{f}{rq_r})^2\right). \tag{5.11}$$

From the FKKS ansatz, two distinct modes emerge for even parity, each revealing unique behaviors. The even-parity scalar mode is distinguished from the even vector mode by ν parameter, and the parameter ν can be written as

$$\nu_{\pm} = \frac{-\omega}{l(l+1)} \left(\frac{1 \pm (1 + 4(l+1)\frac{\mu^2}{\omega^2})^{1/2}}{2} \right), \tag{5.12}$$

where the "+" sign corresponds to the even-parity vector mode and the "$-$" sign to the even-parity scalar mode. In this section, we will present the results of rigorous bounds for these cases.

In this section, we consider two bounds for each mode of the greybody factor. The first is the strict bound, which corresponds to the higher bound derived in the original paper [14], In this case, the function h is chosen as $h(r_*) = \sqrt{\omega^2 - f\mu}$. The second is the non-strict bound, which provides a lower bound for the greybody factor. For this case, h can be chosen as $h(r_*) = \sqrt{\omega^2 - V_{eff}}$.

5.2.1 The even-parity scalar mode

In this case, the even-parity scalar mode is essentialy different from the odd-parity mode, and thus, we cannot directly use the same "h" function as in the odd-parity case. Instead, we seek to find an appropriate "h" function to manage the divergent terms arising after integration. However, this "h" function as must still satisfy the condition $h(-\infty) = h(\infty) \sim \omega$. Moreover, the behavior of the greybody factor should remain physically reasonable and consistent with the expected transmission probabilities.

First, we choose the "h" function to test bound, the non-strict bound as

$$h(r_*) = \sqrt{\omega^2 - \left(1 - \frac{2}{r}\right)\mu^2 - \frac{2(1-\frac{2}{r})}{1+\nu_-^2 r^2}\mu^2} \tag{5.13}$$

This bound still satisfies the small mass condition $h(-\infty) = h(\infty) \sim \omega$. In Fig. 13, we plotred the greybody factor by using rigorous bound and "h" function as defined in Eq. (5.13). The trend of transmission amplitude is inaccuracy. it is because we have shown the effective potential of this case in the previous chapter the trend of transmission probability should shift to the right when the Proca's mass increases.

We choose the h function for the strict bound in the form

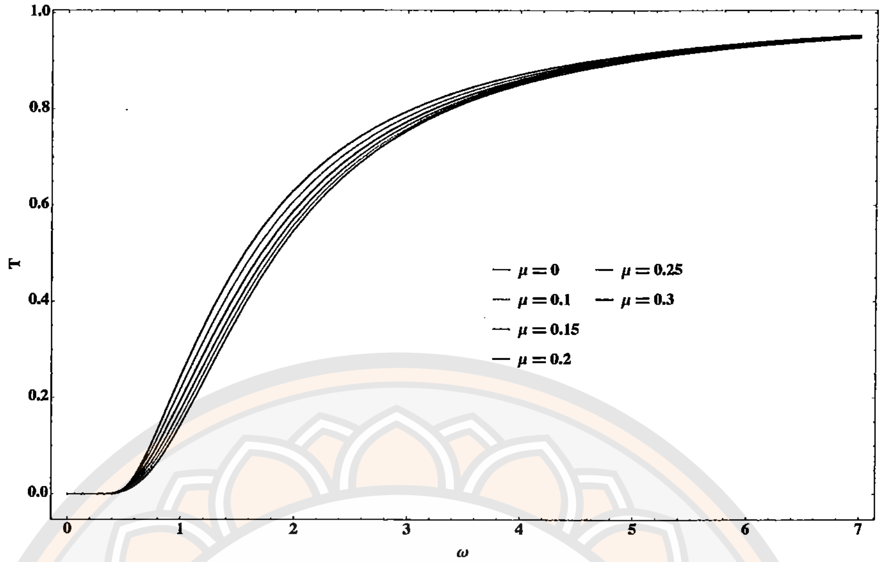

Figure 13 **The rigorous bound for the even-parity scalar mode, by choosing h as the non-strict bound with $l = 1$ and variation μ.**

$$h(r_*) = \sqrt{\omega^2 - V(r)_{eff-evenscalar}}, \tag{5.14}$$

where $V(r)_{eff-evenscalar}$ is the effective potential of the even-parity scalar mode, this presents a sufficient condition for evaluating the bounds in the region of $\omega^2 > V|_{peak}$ and it becomes trivial if $\omega^2 < V|_{peak}$ [14]. Since this function also satisfies the condition $h(-\infty) = h(\infty) \sim \omega$, we obtain the greybody factor by using rigorous bound as

$$T \geq \operatorname{sech}^2 \int_{-\infty}^{\infty} \frac{\sqrt{\left(\partial_{r_*} \sqrt{\omega^2 - V_{eff_{even-scalar}}}\right)^2}}{2\left(\omega^2 - V_{eff_{even-scalar}}\right)^{1/2}} dr_*. \tag{5.15}$$

We plot the greybody factor in Fig. 14 by using rigorous bound and "h" function as defined in Eq.(5.14) while varying μ with $l = 1$. The behavior of the greybody factor appears reasonable when we compare it with the plot of the effective potential in Figs. 5a and 5b. As the mass of the Proca particle increases, the effective potential increases, leading to a lower transmission probability. That means lower potential barriers allow waves to pass through more easily, thus the greybody factor increases.

5.2.2 The even-parity vector mode

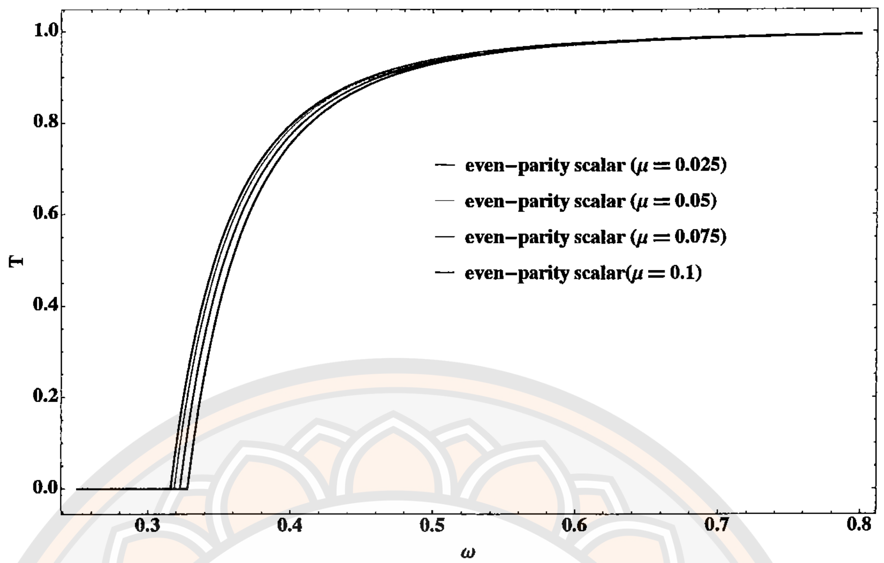

(a) **Vriation of $\mu = 0.025$ to $\mu = 0.1$ with $l = 1$.**

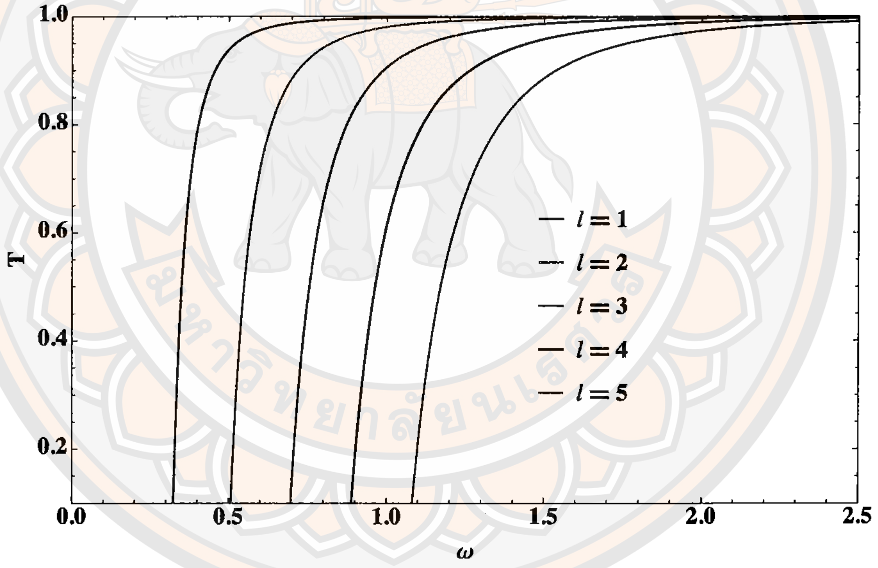

(b) **vriation of $l = 1$ to $l = 5$ with $\mu = 0.1$.**

Figure 14 The rigorous bound for even-parity scalar mode, by choosing h be the strict bound.

In this subsection, we have discussed the even-parity vector mode by considering the rigorous bound, the effective potential shown in Eq. (4.62). Similarly, in even-parity scalar, we chose the “h” function for non-strict bound first in the form as

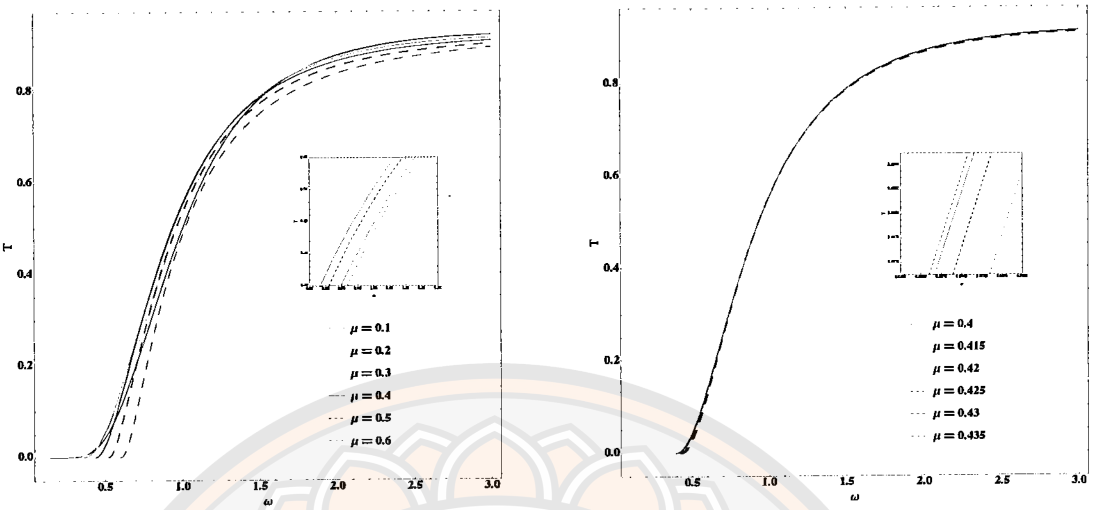

(a) Variation of Proca mass 0.3 - 0.6.

(b) Variation of Proca mass 0.4 - 0.435.

Figure 15 The greybody factor for even-parity vector by chose non-strict bound. The solid lines represent cases where the graph shifts to the left as the mass increases, while the dashed lines indicate that as the mass increases, the graph shifts to the right.

$$h(r_*) = \sqrt{\omega^2 - f\mu^2 - \frac{2f\mu^2}{(1+\nu_+^2 r^2)}}, \tag{5.16}$$

where ν_+ for even-parity vector mode. This function also satisfies the condition $h(-\infty) = h(\infty) \sim \omega$. Therefore, the greybody factor can written as

$$T \geq \operatorname{sech}^2 \int_{-\infty}^{\infty} \frac{\sqrt{[\partial_{r_*} h(r_*)]^2 + [\omega^2 - V_{eff_{even-vector}}(r_*) - h^2(r_*)]^2}}{2h(r_*)} dr_*. \tag{5.17}$$

In the Fig. 15a, we increased the mass from 0.1 to 0.6. the graph starts to shift less from the line of $\mu = 0.3$, and the overall trend moves to the right when the mass exceeds 0.4. Therefore, in Fig. 15b, we examine the mass in more detail, which revealed that the actual turning point of the graph occurs approximately between 0.42 and 0.425. Beyond this range, the behavior of the greybody factor in the even-parity vector mode resembles that of the previous modes.

We next discuss the behavior of the even-parity vector mode, this mode shows significant differences compared to the odd-parity mode and the even-parity scalar mode. In this mode, the transmission probability increases as the Proca's mass"μ" increases, which is evident from the graph shifting to the left, indicating that the transmission probability becomes significant at lower frequencies as shown in Fig. 15. However, an unusual behavior is observed when the Proca mass increases beyond a certain point, the graph shifts back to the right, resulting in a decreased transmission probability as the mass continues to increase beyond this threshold.

Next, we set "h" function as

$$h(r_*) = \sqrt{\omega^2 - V_{eff_{even-scalar}}} \tag{5.18}$$

this h function represent the strict bound. This choice simply means that we are not permitting any classically forbidden region, where the effective potential as shown is Eq. (3.22), then

$$T \geq \operatorname{sech}^2\left(\frac{1}{2}\int_{-\infty}^{\infty}\frac{|\partial_{r_*}h|}{h}dr_*\right). \tag{5.19}$$

The rigorous bound on the greybody factor for the strict bound is shown in Fig. 16. Similar to the previous result in Fig. 15, when the Proca mass increases beyond a certain point the graph shifts back to the right. In Fig. 16, we set $l = 2$ and explore the variation of the Proca mass ranging from 0.1 to 0.5 to observe how the transmission probability behaves as the mass increases. In Fig. 16b, We vary the mass in smaller steps to find the exact turning value of μ where the graph shifts back to the right, which is approximately between $\mu = 0.3$ and $\mu = 0.325$. This difference in the "turning point" may be due to the choosing of the "h" function which the non-strict bound causes the transmission probability to be less accurate than the "h" chosen as the strict bound. In the last chapter, we will further compare

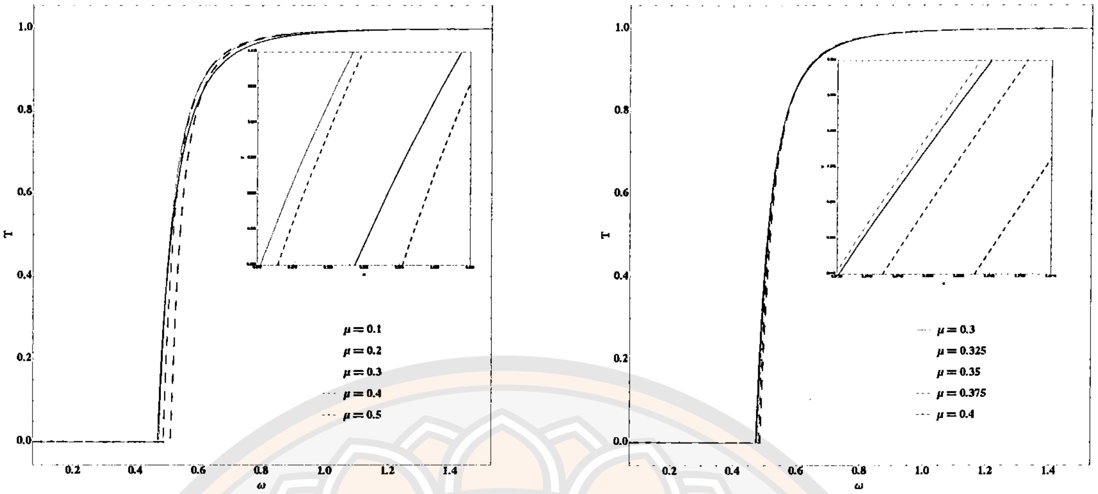

(a) vriation of $\mu = 0.1$ to $\mu = 0.5$ with $l = 2$.

(b) vriation of $\mu = 0.3$ to $\mu = 0.4$ with $l = 2$.

Figure 16 The rigorous bound for even-parity vector mode, by choosing h as the strict bound.

the differences between these bounds and the WKB approximation to determine which bound choice yields results that best align with WKB approximation.

5.3 Discussion of Rigorous bound

In this section, we compare the greybody factors for odd-parity and even-parity modes by fixing $l = 2$ and varrying "μ" with the rigorous bound method. We first present the results for the non-strict bounds in Fig. 17. Three points are required to be summarised here. Firstly, we find that for fixing "ω" and "μ", the even-parity scalar mode shows the lowest transmission probability, the result for the odd-parity mode is a slightly higher but nearly overlaps with the even-parity scalar one, and the even-parity vector mode presents the highest transmission probability. The order for the transmission probabilities of these three modes is reasonable when we compare the results with the maximum of the effective potentials presented in Ch. 4.

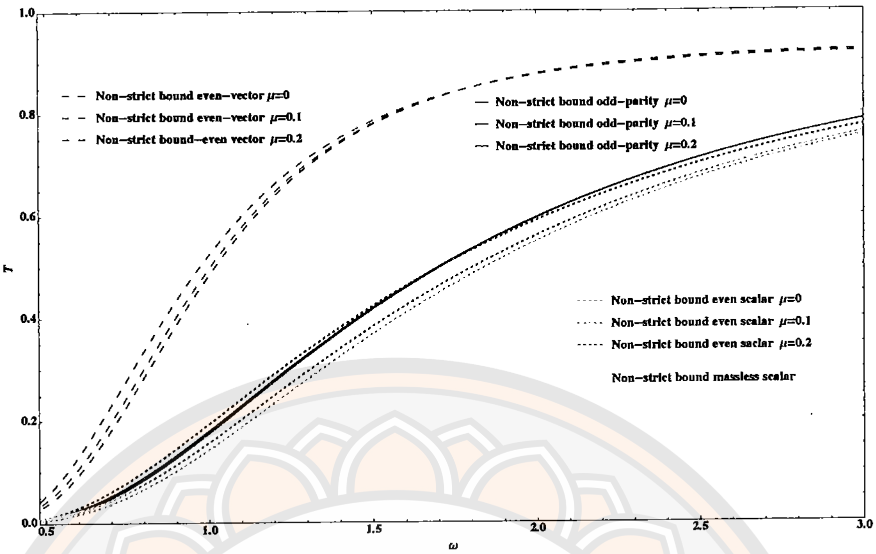

Figure 17 The compare of each mode by using rigorous non-strict bound.

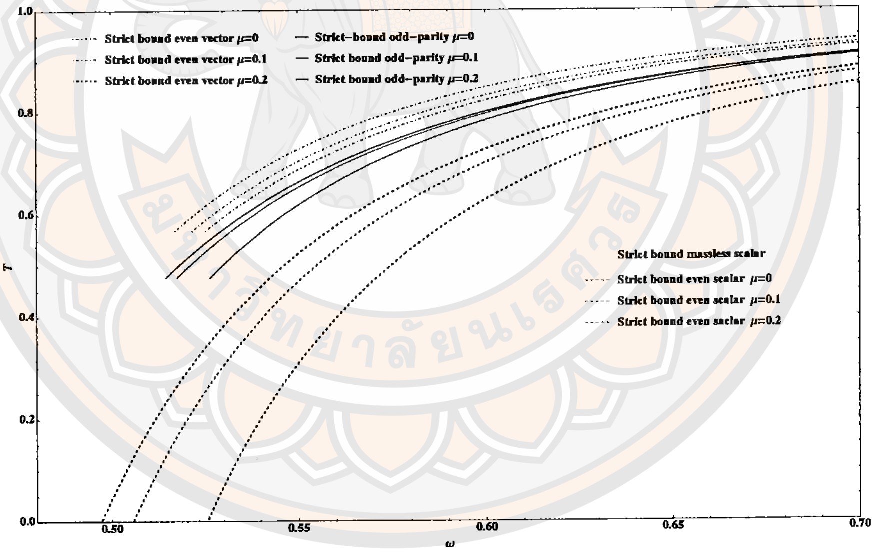

Figure 18 compares the even-parity vector and scalar modes using the strict bound with l=2 and variation of μ.

Secondly, the behavior of the even-parity scalar modes does not fit the behavior of the effective potentials when fixing "l" and "μ" increased. To specify this, one may observe that for the odd parity modes, the transmission probability decreases when the Proca mass increases, and for the even-parity vector modes, the transmission probability increases when the Proca mass increases. These phenomena fit the behaviors of the effective potentials demonstrated in the previous sections. However, for the even-parity scalar modes, the greybody factor tends to increase as the Proca mass increases. This is beyond the general expectation because the maximum of effective potential increases when "μ" increases for the even-parity scalar modes as in Fig. 5b.

Lastly, the greybody factor for the massless even-parity scalar mode shares the same spectrum (Isospectral) as that of the massless scalar field as shown in Fig. 17. Note that the even-parity scalar mode shall be a pure gauge mode in the massless limit. Nevertheless, the degenerate for the even-parity vector and odd-parity modes in the massless limit, can not be shown for the non-strict bounds.

To solve the above issue, we impose the strict bound in previous sections and the comparison for each mode is presented in Fig. 18. Again, the parameters set are given by fixing $l = 2$ and variation "μ". It is still true for the order of even-parity vector, odd parity, and even-parity scalar modes, as well as the isospectral of massless even-parity scalar mode and massless scalar perturbation. Two benefits are presented for the strict bound results. The behavior of the transmission probability for the even-parity scalar modes reflects that of the effective potential, exhibiting a decrease as the Proca mass increases. The degenerate for the even-parity vector and odd parity modes in the massless limit is also presented closely in the plot.

In summary, the rigorous bound method present a sufficient lower bound for the greybody factor based on the rigorous mathematical algebraic analysis. b The choice of the h function, guided by the asymptotic behavior of the effective potential, influences both the resulting bounds and the region of the potential that contributes most significantly to the estimation (efficient area). We present two examples, the non-strict and strict bound, in which the strict bound present better results but lost some information because the efficient area are $\omega^2 \gtrsim V_{eff}|_{max}$ [14]. The non-strict bound present a wilder lower bound and the general behaviors

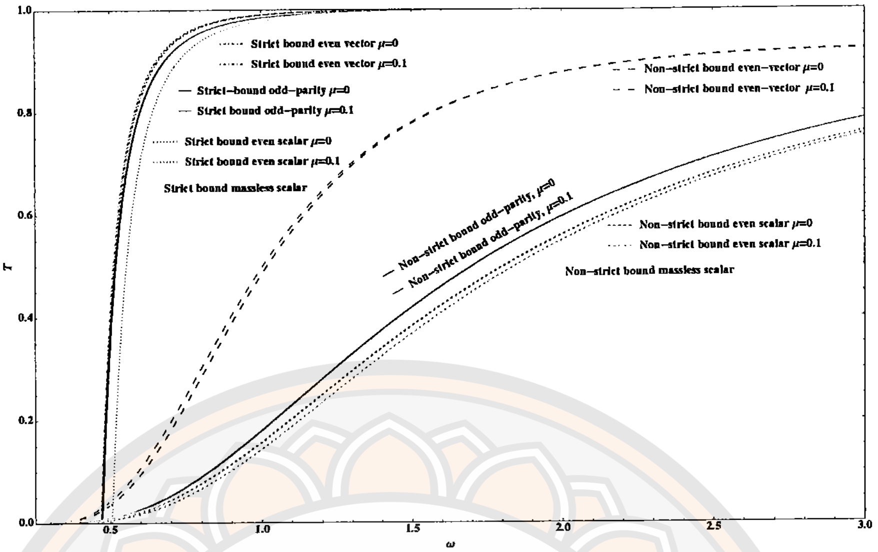

Figure 19 **Compares the strict-bound and non-strict bound with $l = 2$ and variation of μ**

are less accurate than the strict bound, but the mathematical bound is still true. Nevertheless, The non-strict bound is still the lower bound of the strict bound as presented in Fig. 19.

CHAPTER VI

WKB APPROXIMATION

In this chapter, we apply the WKB approximation to each mode of the Proca field. We start by looking at the odd-parity mode and monopole mode in Ch. 6.1, where the wave equation resembles a Schrödinger-like equation with an effective potential. Next, we move on to the even-parity mode, which splits into even-parity scalar and even-parity vector mode in Ch. 6.2, each with its unique features in the WKB framework. By comparing how the WKB method handles these modes, we gain deeper insights into how the potential barriers around a black hole affect the probability of wave transmission in Ch. 6.3.

6.1 WKB for the odd-parity mode and monopole mode

6.1.1 WKB for the odd-parity mode

For the WKB approximation, it is convenient to rewrite the radial equation in the form Eq. (3.58). In the black hole case the radial equation suitable as

$$\left(\frac{d^2}{dr_*^2}+Q\right)\Psi=0. \tag{6.1}$$

where r_* is the tortoise coordinate, $Q=\omega^2-V(\omega,\mu,r)$ and $V(\omega,\mu,r)$ is the effective potential for each case as we show in the previous chapter. For the maximum value of the effective potential V_{max}, the condition for intermediate energy can be written as $\omega^2\approx V_{max}(\omega,\mu,r_{\mathrm{max}})$, when the energy of the field is decreased to such as extend that ω^2 is close to the peak of the potential. The r_{max} is the corresponding radial value at the maximum point of the effective potential.

From the previous chapter, we show the introduction for solving the transmission amplitude with WKB approximation as

$$T = \frac{1}{1+e^{2S}}, \tag{6.2}$$

where the function $S(\omega)$ can expressed as

$$\begin{aligned} S(\omega) \;&=\; \pi k^{1/2}\left[\frac{1}{2}z_0^2 + \left(\frac{15}{64}b_3^2 - \frac{3}{16}b_4\right)z_0^4\right] \\ &\quad + \pi k^{1/2}\left[\frac{1155}{2048}b_3^4 - \frac{315}{256}b_3^2 b_4 + \frac{35}{64}b_3 b_5 - \frac{5}{32}b_6\right] z_0^6 + \pi k^{-1/2}\left[\frac{3}{16}b_4 - \frac{7}{64}b_3^2\right] \\ &\quad - \pi k^{-1/2}\left[\frac{1365}{2048}b_3^4 - \frac{525}{256}b_3^2 b_4 + \frac{85}{128}b_4^2 + \frac{95}{64}b_3 b_5 - \frac{25}{32}b_6\right] z_0^2 + \mathcal{O}(\omega). \end{aligned} \tag{6.3}$$

where $\mathcal{O}(\omega)$ are the higher order terms.

For the odd-parity mode, the wave equation takes a form analogous to the Schrödinger equation, with an effective potential governing the scattering of waves by the black hole. The general form of the Regge-Wheeler equation for odd-parity perturbations is

$$\left[\partial_{r_*}^2 + \omega^2 - f\left(\frac{l(l+1)}{r^2} + \mu^2\right)\right] u_{odd}(r) = 0, \tag{6.4}$$

where the effective potential for the odd-parity mode of the Proca field can be written as

$$V_{eff(odd)} = f\left(\frac{l(l+1)}{r^2} + \mu^2\right). \tag{6.5}$$

The WKB approximation can be applied directly to this effective potential because $V_{eff(odd)}$ is a function of r for given μ and l. First, we calculate the value of $r_{\max}$ for each combination of μ and l, where $V_{\max}$ represents a result position corresponding to the maximum of the effective potentia. The results are shown in Table 1. This $r_{\max}$ shall be used to express the components in the function $S(\omega)$, which is crucial in solving for the transmission amplitude at the peak energy.

The results are presented in Fig. 20, we fix $\mu = 0.1$ and variation of l. The transmission amplitude decreases as l increases, and the graph shifts to the right. This behavior implies that the transmission probability is lower for higher values

Table 1 Representative values of the $r_{\max}$ at which the odd-parity mode, shown for various Proca masses μ and angular momentum l.

l	μ	$r_{\max}$	l	μ	$r_{\max}$
1	0.1	3.0464	3	0.1	3.0075
1	0.15	3.1087	3	0.15	3.0171
1	0.2	3.2055	3	0.2	3.0306
1	0.25	3.3509	3	0.25	3.0484
1	0.3	3.5752	3	0.3	3.0707
2	0.1	3.0152	4	0.1	3.0045
2	0.15	3.0345	4	0.15	3.0102
2	0.2	3.0625	4	0.2	3.0182
2	0.25	3.1001	4	0.25	3.0287
2	0.3	3.1487	4	0.3	3.0416
5	0.1	3.0030	5	0.15	3.0068
5	0.2	3.0121	5	0.25	3.0190
5	0.3	3.0275			

of l, and energy must be increased to maintain significant transmission. This is consistent with the nature of the effective potential, as higher l, the maximum of the potential barrier increases, thus requiring more energy for transmission, which can be confirmed by the potential behavior in Fig. 9. Furthermore, we investigate the effect of varying the Proca mass, as shown in Fig. 21. This figure presents the greybody factor of odd-parity mode with $l = 1$ and variation μ. The trend of transmission probability decreases when the Proca mass increases. These two plots can confirm the behavior of the greybody factor in the odd-parity mode which we obtain from the rigorous bound method. The trend is similar and we will discuss this in detail by the end of the last chapter.

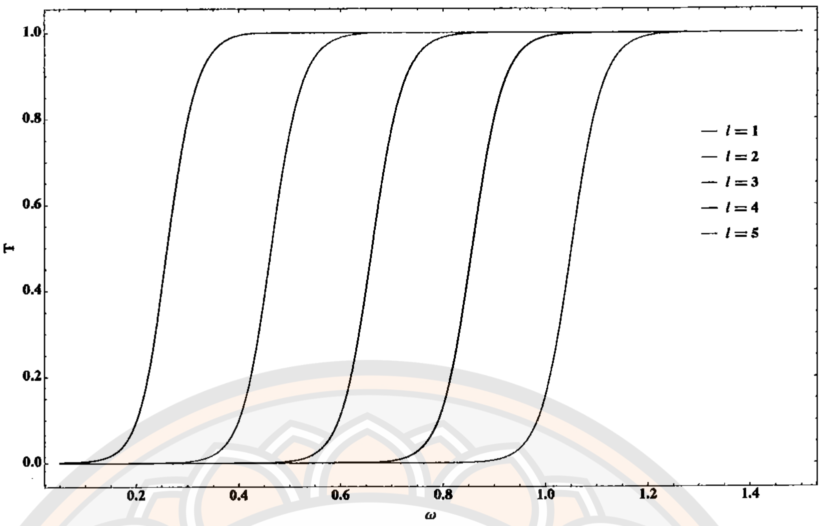

Figure 20 **The greybody factor for odd-parity with μ=0.1 and change l.**

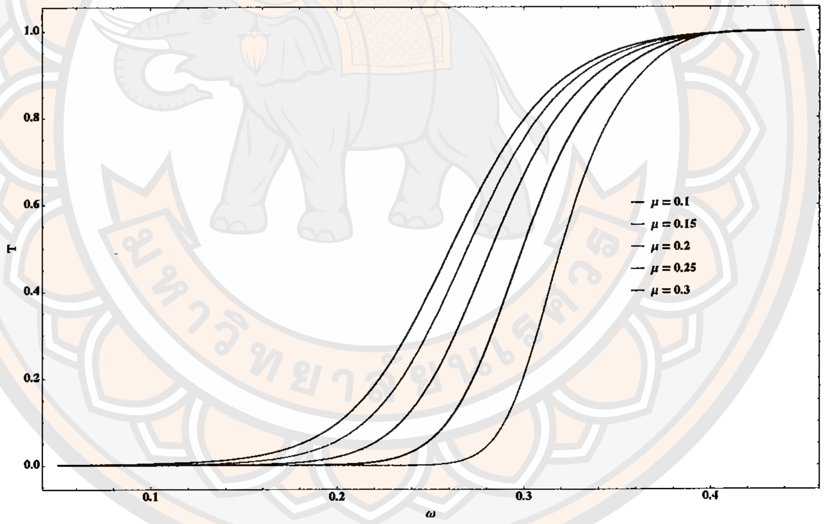

Figure 21 **The greybody factor for odd-parity with $l=1$ and variation of μ.**

6.1.2 WKB for monopole mode

For the monopole modes, as discussed in the previous chapter, we impose the necessary conditions to reduce the even-parity equation to the monopole mode. The radial equation for the monopole mode is given by

$$\left[\partial_{r_*}^2+\omega^2-f(r)\left(\frac{2\,(r-3)}{r^3}+\mu^2\right)\right]u_{lm}(r)=0. \tag{6.6}$$

Table 2 Sample values of $r_{\max}$ for the monopole mode ($l = 0$) with different values of Proca mass μ

μ	$r_{\max}$
0.025	5.20137
0.05	5.24771
0.075	5.32725
0.1	5.44386

and effective potential is expressed as

$$V_{eff(mono)} = f(r)\left(\frac{2\,(r-3)}{r^3} + \mu^2\right). \tag{6.7}$$

Next, we need to find the critical points of this potential for each value of "μ". In the case of monopole mode, the effective potential has three critical points. However, we are particularly interested in finding the first positive maximum peak of this potential and expanding around that peak. This is because the WKB approximation require us to expand around the peak corresponding to the maximum value of effective potential. The value of $r_{\max}$ for the value of $\mu = 0.025$ to $\mu = 0.1$ is shown in Table 2.

In Fig. 22, we present the shape of the effective potential for the monopole mode and show the real value of r maximum for each Proca mass. At very small r, the potential rises sharply from negative values and reaches its peak. The shape of the potential suggests that waves can be trapped between the event horizon and the potential barrier, which describes how black holes scatter incoming radiation.

In Fig. 23, we present the shape of the greybody factor in the monopole mode with $l = 1$ and variation of "μ". The shape of the greybody factor in this case is similar to other cases, as the Proca mass increases, the transmission probability decreases. This behavior is similar to the odd-parity mode. In addition, Fig. 23 demonstrates a shift in the curves as Proca mass increases, the curves shift to

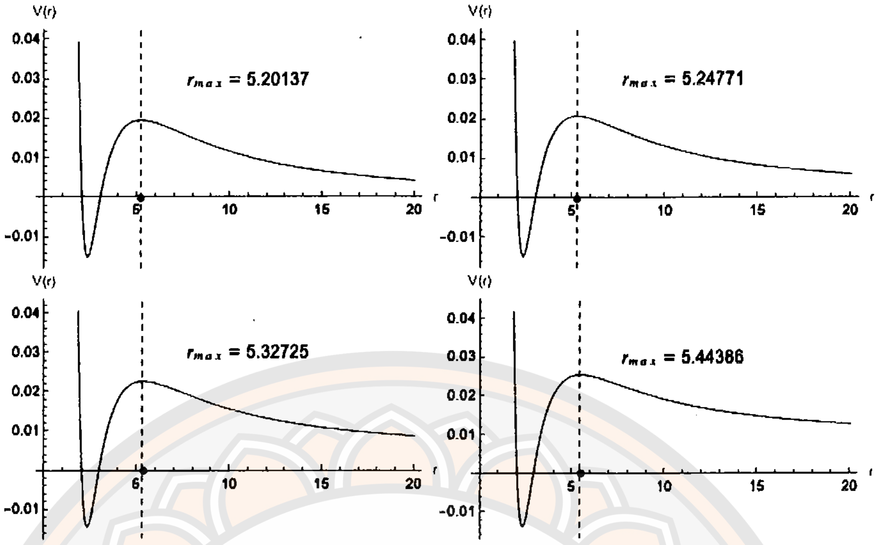

Figure 22 **The effective potential of monopole mode and show the real value of r maximum of the peak.**

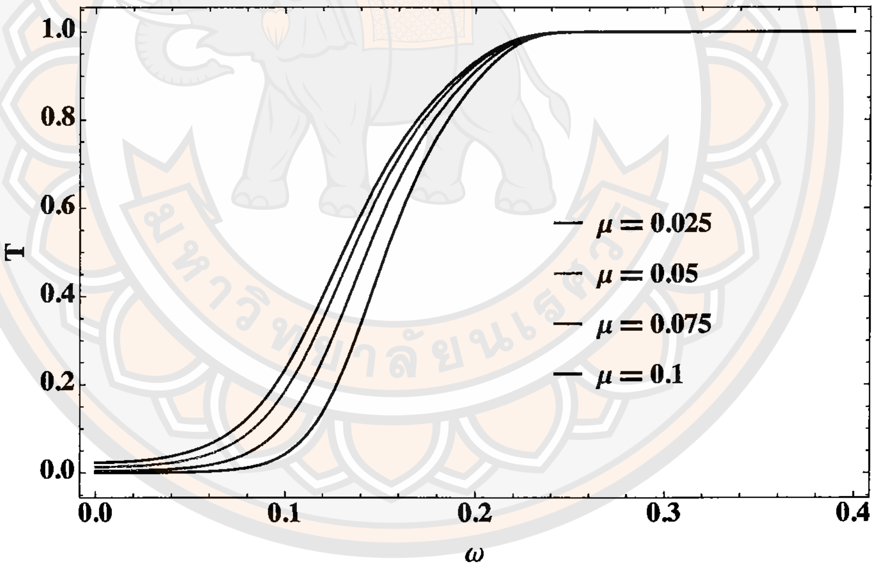

Figure 23 **The greybody factor for monopole mode as variation of μ.**

the right, meaning that higher energies are required to achieve the same level of transmission probability. This shift corresponds to the fact that increasing "μ" raises the potential height and pushes the peak location "r_{max}" outward, further reducing the transmission probability for lower-frequency waves.

6.2 WKB for the even-parity mode

For the even-parity modes, the effective potentials are functions of r and ω, for given values of μ and l. Thus, the effective potential can be expressed as a series expansion. However, since the potential includes terms involving ω that appear implicitly in the equation, it is not possible to determine the exact location of the potential peak $r_{\max}$ for a general value of ω. The potential can be written in the form

$$V(\omega,\mu,r) = V_0(r) + V_1(\omega,r) + V_2(\omega,r)\mu^2 + ... + V_n(\omega,r)\mu^n. \qquad (6.8)$$

In the same way with $r_{\max}$, can be expanded as

$$r_{\max} = r_0 + r_1\mu + r_1\mu + r_2\mu^2 + ... + r_n\mu^n \equiv r_0 + \delta, \qquad (6.9)$$

where r_0 denotes $r_{\max}$ for the massless case. We can obtain r_0 by solving the following equations

$$0 = \partial_r V(\omega,\mu,r)|_{\max}. \qquad (6.10)$$

We expand this differential equation around r_0 as

$$\begin{aligned} 0 = {} & V'(\omega,\mu,r_0) + \delta V''(\omega,\mu,r_0) + \frac{1}{2}\delta^2 V^{(3)}(\omega,\mu,r_0) + \frac{1}{6}\delta^3 V^{(4)}(\omega,\mu,r_0) \\ & + \frac{1}{24}\delta^4 V^{(5)}(\omega,\mu,r_0) + \frac{1}{120}\delta^5 V^{(6)}(\omega,\mu,r_0) + \frac{1}{720}\delta^6 V^{(7)}(\omega,\mu,r_0). \qquad (6.11) \end{aligned}$$

Note that, the primes and the superscript with the number denote the order of derivative to r. Substituting Eqs. (6.8) and (6.9) in Eq. (6.11), solving the coefficients of μ order by order as

$$\begin{aligned} 0 &= \mu\left[V_1'(\omega,r_0) + r_1 V_0''(\omega,r_0)\right], \\ 0 &= \mu^2\left[V_2'(\omega,r_0) + r_2 V_0''(\omega,r_0) + r_1 V_1''(\omega,r_0) + \frac{1}{2}r_1^2 V_0^{(3)}(\omega,r_0)\right], \\ 0 &= \mu^3\left[V_3'(\omega,r_0) + r_3 V_0''(\omega,r_0) + r_2 V_1''(\omega,r_0) + r_1 V_2''(\omega,r_0)\right. \\ & \quad \left. +\mu^3\left[r_1 r_2 V_0^{(3)}(\omega,r_0) + \frac{1}{2}r_1^2 V_1^{(3)}(\omega,r_0) + \frac{1}{6}r_1^3 V_0^{(4)}(\omega,r_0)\right]\right]. \qquad (6.12) \end{aligned}$$

Table 3 Values of r for varying magnitudes of the Proca mass μ as it appears in Eq. (6.9).

order of μ	r_i
0	2.886
1	0
2	8.44013
3	0
4	$57.3746 - \frac{17.5217}{\omega^2}$
5	0
6	$493.228 + \frac{70.0868}{\omega^4} - \frac{349.415}{\omega^2}$

It is noteworthy that r_0 can be obtained by solving the zeroth order equation in Eq. (6.11). then the other values of r can be obtained from Eq. (6.12).

6.2.1 WKB for even-parity scalar mode

In this case, we consider the potential for the even-parity scalar mode

$$V_{eff_{even-scalar}} = f\left(\frac{l(l+1)}{r^2} + \mu^2\right) + \partial_{r_*}\left(\frac{f}{rq_r}\right) + \left(\frac{f}{rq_r}\right)^2 + \frac{2f\omega\nu_-}{q_r}, \qquad (6.13)$$

where $q_r = 1 + \nu_-^2 r^2$, and ν_- are given in Eq. (4.47). The WKB technique for this mode differs significantly from the odd-parity mode. In this scenario, we need to expand the effective potential and $r_{\max}$ as demonstrated in Eqs. (6.8) and (6.9). We expand the effective and the coefficients r_i in terms of ω up to the sixth order as shown in the Table 3. Then we obtain the $r_{\max}$ as

$$\begin{aligned} r_{\max} &= 2.886 + 8.44013\mu^2 + \mu^4\left(57.3746 - \frac{17.5217}{\omega^2}\right) \\ &\quad + \mu^6\left(493.228 + \frac{70.0868}{\omega^4} - \frac{349.415}{\omega^2}\right). \end{aligned} \qquad (6.14)$$

Next, we determine the transmission probability for energies near the potential peak, using Eq. (3.72). The results are shown in Fig. 24. In this figure,

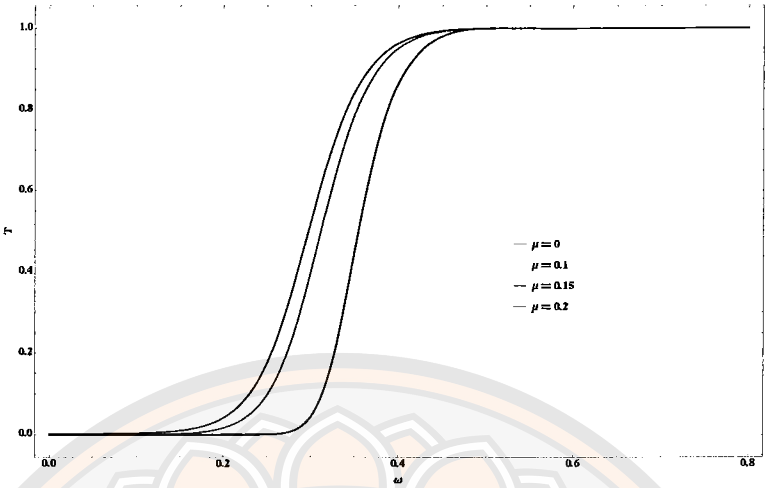

Figure 24 **The greybody factor for even-parity scalar with $l = 1$ for various Proca mass.**

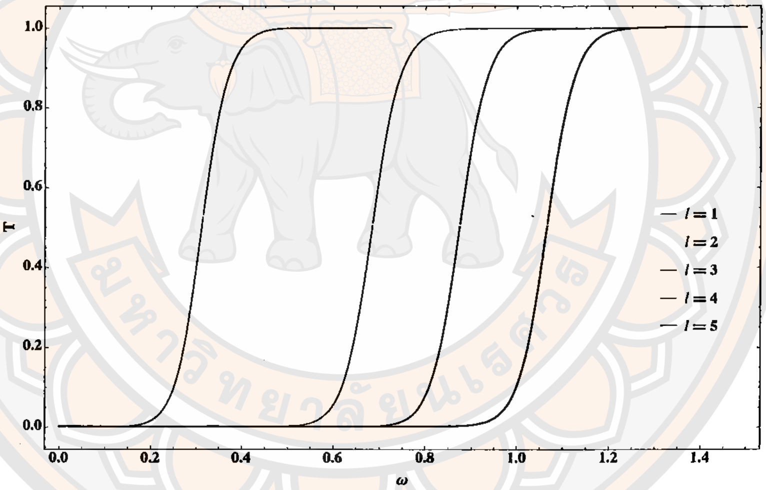

Figure 25 **The greybody factor for even-parity scalar with $\mu = 1$ for various l.**

we demonstrate the variation of Proca mass 0 to 0.2 for $l = 1$. The behavior of corresponding transmission energy ω increases as the Proca mass increases for the same transmission probability. This result confirms the effective potential shown in Fig. 6 as well as the strict bound results for even-parity scalar mode. Furthermore, we explore the effect of varying l with "$\mu = 0.1$, as illustrated in Fig. 25. As the angular momentum increases, this requires higher energy ω to tunnel through the black hole potential. This implies that the transmission probability decreases.

Table 4 **Positive real tuning points for different values of ω and Proca mass with $l = 2$.**

μ	ω	$r_{\max}$	μ	ω	$r_{\max}$
0.1	0.1	2.95017	0.2	0.1	2.97019
0.1	0.2	2.94163	0.2	0.2	2.95735
0.1	0.3	2.93497	0.2	0.3	2.94809
0.1	0.4	2.92909	0.2	0.4	2.93681
0.3	0.1	3.01913	0.4	0.1	3.11299
0.3	0.2	3.00314	0.4	0.2	3.09504
0.3	0.3	2.99199	0.4	0.3	3.08271
0.3	0.4	2.97974	0.4	0.4	3.06826
0.5	0.1	3.28644	0.5	0.2	3.26842
0.5	0.3	3.25617	0.5	0.4	3.24192

6.2.2 WKB for the even-parity vector mode

The effective potential for the even-parity vector mode, given by

$$V_{eff_{even-vector}} = f(r)\left(\frac{l(l+1)}{r^2} + \mu^2\right) + \partial_{r_*}\left(\frac{f}{rq_r}\right) + \left(\frac{f(r)}{rq_r}\right)^2 + \frac{2f(r)\omega\nu_+}{q_r}, \quad (6.15)$$

where $q_r = 1 + \nu_+^2 r^2$, and ν_+ are given in Eq. (4.47). This potential differs from others in solving the $r_{\max}$ for the maximum of effective potentials, it is because the massless case cannot be determined solely from the potential without considering ω. In other words, for the massless case, $r_{\max}$ must be solved for each specific ω value, and the WKB approximation must be applied separately for each ω. In Table 4, we provide some examples of the $r_{\max}$ for $l = 2$ across Proca mass values ranging from 0.1 to 0.5.

We present the shape of the greybody factor for the even-parity vector mode for fixing $l = 2$ and increasing the Proca mass in Fig. 26. The plot is generated from

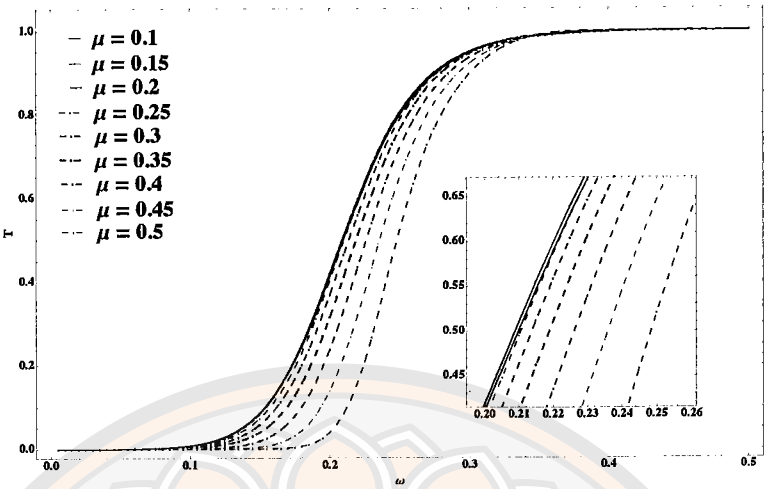

Figure 26 The greybody factor for even-parity vector mode with $\mu = 0.1$ to 0.5 with l=2.

100 data points. The data are generated by using ω from 0.005 to 0.5 and advancing in steps of 0.005. As we have shown using the rigorous bound method before, the behavior of the even-parity vector mode differs from that of the even-parity scalar and odd-parity mode. Specifically, the greybody factor for the even-parity vector mode shifts to the left as the mass of the Proca particle increases, indicating a higher transmission probability. However, when the Proca mass increases beyond a critical point, the graph shifts to the right, indicating a decreased transmission probability as the mass continues to increase beyond this point.

From Fig. 27a, we demonstrate the variation of Proca mass 0.15 to 0.22 with $l = 1$. The solid line represents the trend shifting to the left and the dashed line represents the trend shifting to the right. The critical value of μ for the shift is around 0.19 to 0.20 within the range of $T = 0.614$ to $T = 0.62$. In the Fig. 27b where l is increased to 2, and the Proca mass variation from 0.14 to 0.21. The critical value is located varries $\mu = 0.17$ and $\mu = 0.18$. From Fig. 27, we also observe that when l increases, the critical turning value of Proca mass decreases. Therefore, it is of interest to check whether, for a larger l, the critical turning value of μ still exists or not. These two plots are generated from 100 data points, covering

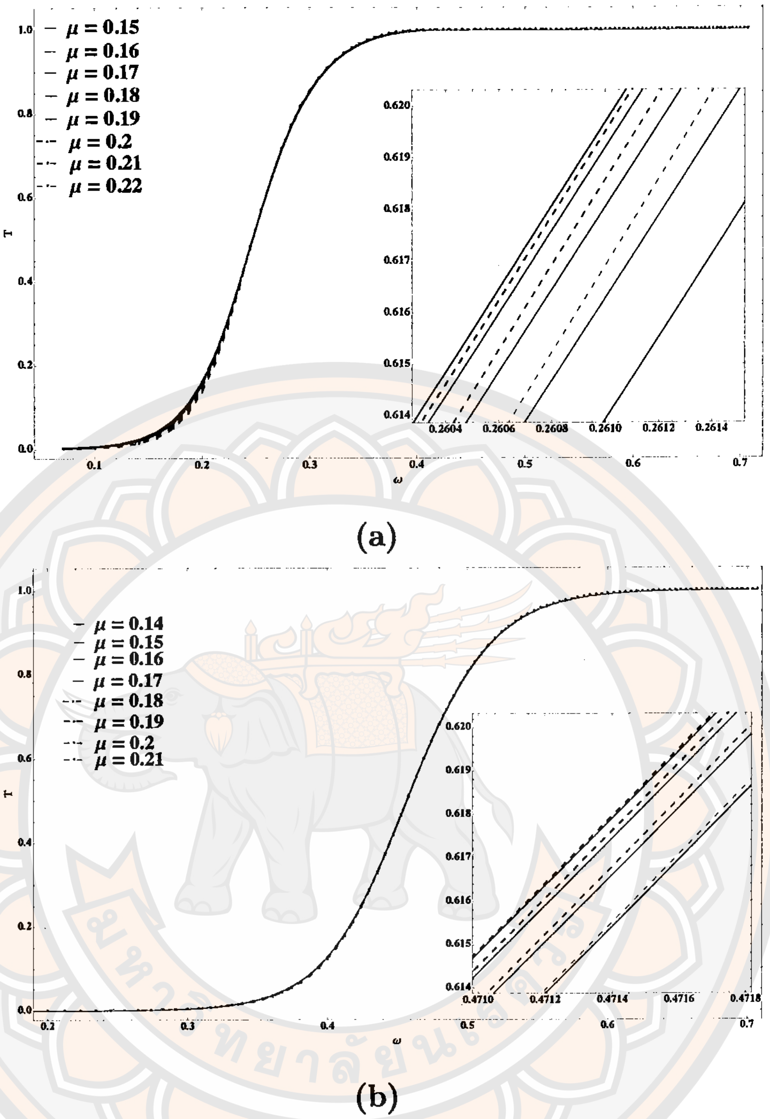

(a)

(b)

Figure 27 The WKB for greybody factor of even-parity vector mode with $l = 1$ and $l = 2$, where the graph shifts to the left as the mass increases, while the dashed lines indicate that as the mass increases, the graph shifts to the right.

the range of ω from 0.005 to 0.5 in steps of 0.005.

As such, we study the behavior of the greybody factor for the larger values of l, and the results are presented in Fig. 28. This plot is generated from 100 data points, where the covering range of ω was 0.05 to 5 with a step size of 0.05. The critical turning value of Proca mass is between $\mu = 0.16$ to $\mu = 0.17$ within the

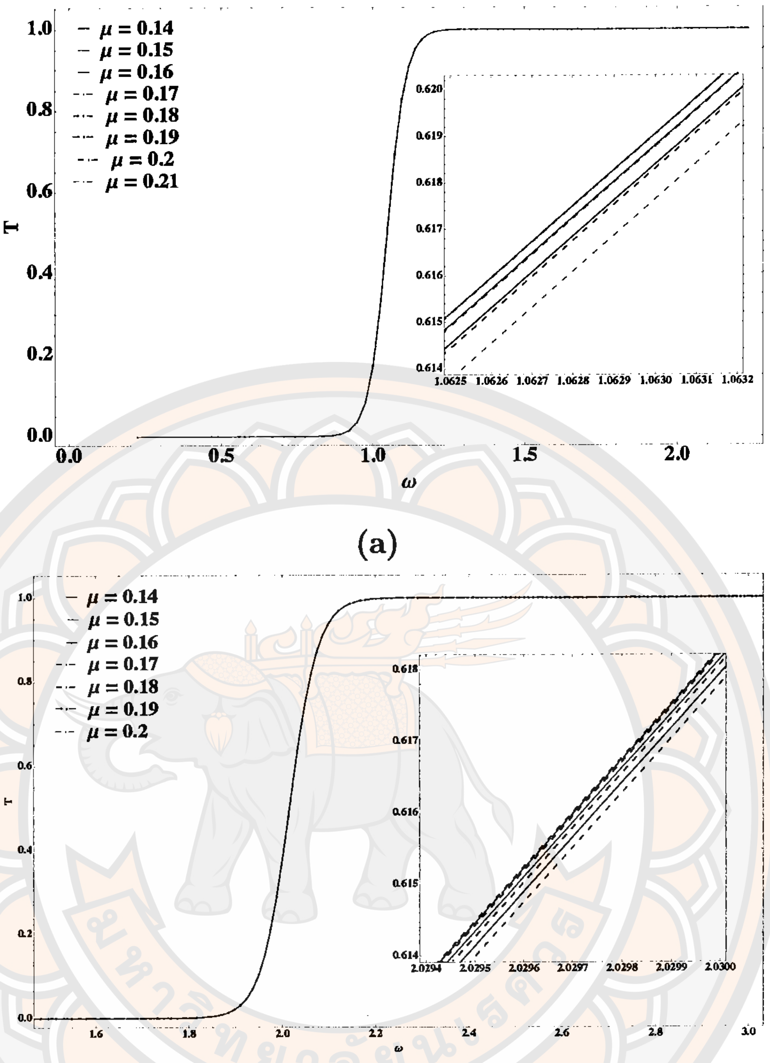

(a)

(b)

Figure 28 The WKB for greybody factor of even-parity vector mode with $l = 5$ and $l = 10$, where the graph shifts to the left as the mass increases, while the dashed lines indicate that as the mass increases, the graph shifts to the right.

range of $T = 0.614$ to $T = 0.620$ for both of the plots, where $l = 5$ for Fig. 28a and $l = 10$ for Fig. 28b. These plots are generated from 200 data points of ω, covering the range of 0.05 to 10 with a step size of 0.05. The trend of critical turning value decrease as we expecte but did not change too much unless it is still a non-vanish value until $l = 10$. Therefore, we summarize that as l gets higher, the rate of

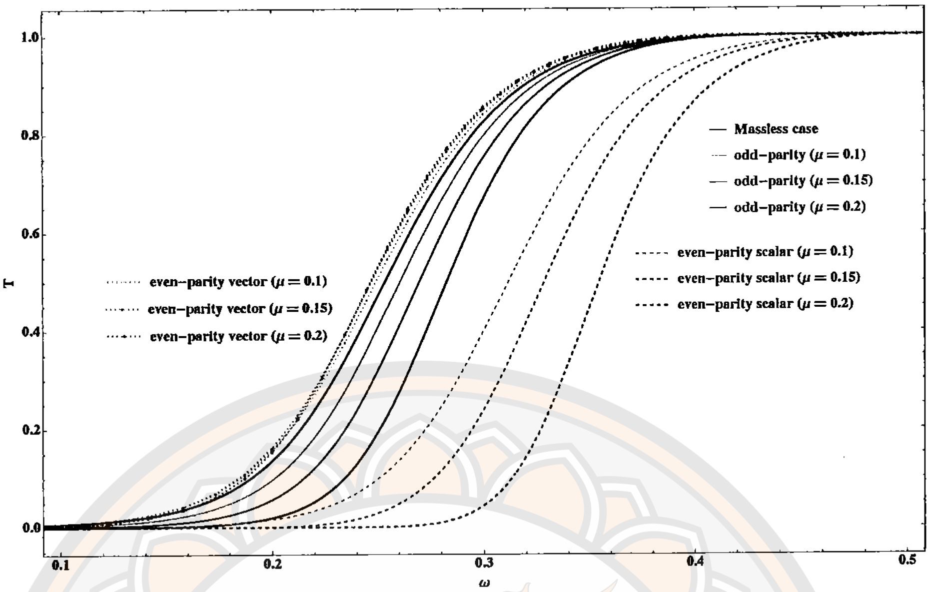

Figure 29 **Comparison of the greybody factors for various modes at $l = 1$ and varying μ.**

decrease gets slower when compared to lower values of l.

Lastly, the WKB approximation results for the even-parity vector polarization also confirm the transmission probability trends derived by using the rigorous bound method as presented in the previous chapter. Although the critical points of the Proca mass differ slightly between the two methods, the overall behavior of the greybody factor remains consistent. This discrepancy in critical points may arise due to the differing approaches used to calculate the transmission probability.

6.3 Discussion of WKB approximation

In the previous subsection, we examine the characteristics of the greybody factor for each mode. Although the shape of each mode is quite similar, they differ in the energy values at which they respond. In this subsection, we compare the characteristics and behavior of the greybody factor for odd-parity mode and even-parity mode by fixing $l = 1$ and variation "μ" with the WKB approximation.

In Fig. 29, we compare the characteristics of each mode with $l = 1$ while

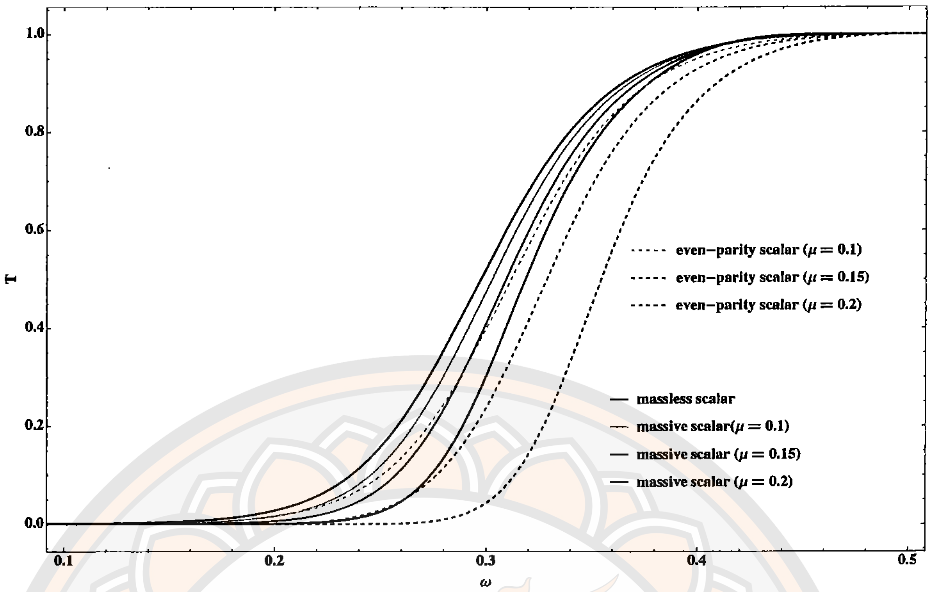

Figure 30 Compare even-parity scalar of Proca field with massive scalar with $l = 1$ and varying μ.

varying the Proca mass. The even-parity vector mode has the highest transmission probability when ”ω and “μ” are fixed. Unlike the other modes, this mode initially shifts to the left as the mass increases, but once the mass reaches a certain point, the graph starts to shift back to the right. This behavior is unique to the even-parity vector mode, as it responds unusually to the changes in mass. At first, adding mass boosts the transmission probability at lower frequencies, but after a certain threshold, further increases in mass reduce the transmission probability, shifting the curve back.

For the odd-parity mode, as shown in Fig. 29 by the solid line, the graph shifts to the right as the mass increases. When this mode approaches the massless limit, it converges to the same form as a massless vector field. In the massless limit (shown by the red line), the effective potential of the massless vector field can be expressed as

$$V_{(eff)} = f(r)l(l+1)/r^2, \tag{6.16}$$

where the degenerate of odd parity and even-parity vector mode can also be presented. Lastly, the even-parity scalar mode has the lowest transmission probability, even lower than the odd-parity mode. when this mode approaches the massless limit, as shown in Fig. 30, this mode will be isospectral with the massless scalar limit. In this context, isospectral means that the even-parity scalar mode and the massless scalar field share the same spectrum of frequencies, despite having different forms of the effective potential. In the massless limit, the effective potential for the scalar field simplifies and can be expressed as

$$V_{(eff)} = f(r)\left(\frac{l(l+l)}{r^2} + \frac{2}{r^3} + \mu^2\right). \tag{6.17}$$

In Fig. 30, we compare the even-parity scalar mode with the massive scalar field. As the mass of the particle increases, both cases shift to the right, showing distinct values as the mass changes. That is, for a given particle mass, a Proca particle with even-parity scalar polarization requires a larger energy than a massive scalar particle to contain the same transmission probability.

CHAPTER VII

DISCUSSION AND CONCLUSION

In this chapter, we will show the disscussion and the conclusion of this thesi, and sumerize the idea of the Greybody factor of the Proca field, moreover, we compare the method as we use for obtain the greybody factor for each modes.

7.1 Discussion

In the previous chapter, the radial equations for the Proca field are investigated, and the effective potential $V_{eff}(r)$ is derived. Following this, the shape of the greybody factor is computed using two methods, the rigorous bound and the WKB approximation. These two methods are suitable for analyzing different types of greybody factors as shown in the following subsection. We compare the results obtained from these two methods to understand the behavior of the Proca field in the Schwarzschild background for each mode. Notably, each mode of the Proca field exhibits distinct trends and behaviors in the greybody factor.

7.1.1 Comparison between bound and WKB

As discussed in Ch. 5 and Ch. 6, the two methods used to calculate the greybody factor of the Proca field in Schwarzschild black holes are the rigorous bound and the WKB approximation. This subsection compares the results obtained from these two methods for each mode

For the odd-parity mode, the shape of the transmission amplitude obtained from both methods with $l = 2$ is shown in Fig. 31. This figure shows the trends and behaviors of the odd-parity mode. Both methods produce similar trends, the transmission probability decreases as the Proca mass increases (shift to the left).

However, despite the overall similarity in trends, there is a difference in the results between the two methods. This discrepancy arises because the function

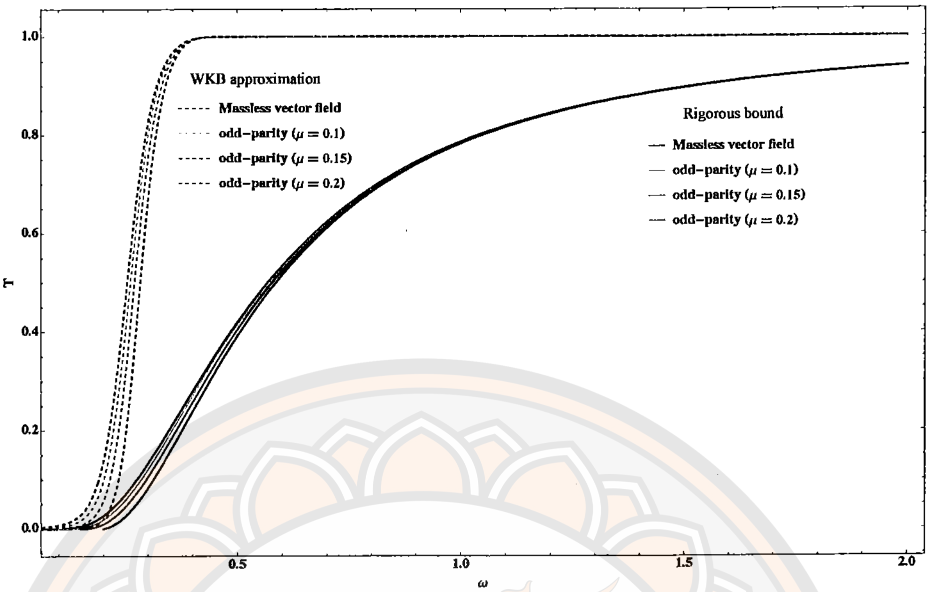

Figure 31 **A comparison between the WKB and rigorous bound for odd-parity mode when $l = 2$. The dashed lines represent the result of the WKB approximation, and the solid lines represent the result of the rigorous bound.**

"$h(r)$" in the rigorous bound method, which is defined as $h(r_*) = \sqrt{\omega^2 - f\mu^2}$. This "$h(r)$" function represents the non-strict bound, the behavior does not closely match the WKB approximation for certain energy values "ω".

Second, for the even-parity scalar mode, the comparison of the two methods is shown in Fig. 32. The greybody factor obtained using the strict bound method has a shape similar to that derived from the WKB approximation. However, the transmission amplitudes calculated by the two methods are different. We also compared the results obtained by using the non-strict bound. This bound is less accurate for rigorous bound methods in the context of even-parity scalar modes because the behavior predicted by this bound deviates significantly from both the strict bound and the WKB approximation. Therefore the choice of the $h(r)$ function used in the non-strict bound is less accurate for studying the even-parity scalar mode, as it fails to capture the consistent transmission behavior. Nevertheless, the non-strict bounds are still the lower bounds for the strict bound and WKB methods.

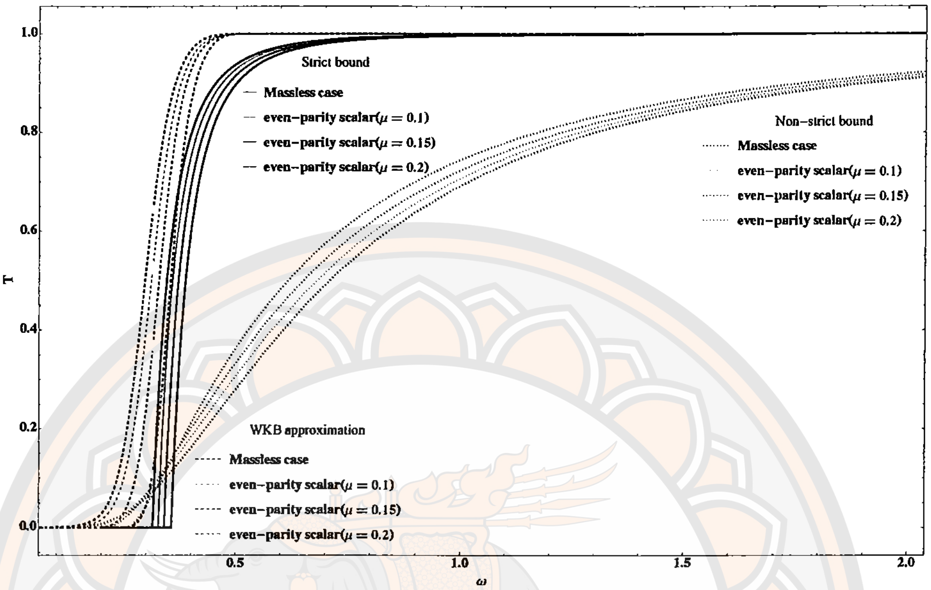

Figure 32 A comparison between the WKB and rigorous bound for even-parity scalar mode when $l = 2$. The dashed lines represent the result of the WKB approximation, the dotted lines represent the result of non-strict bound, and the solid lines represent the result of strict bound.

The final comparison focuses on the even-parity vector mode, which exhibits unique behavior in response to changes in Proca mass "μ". The Proca mass increased leading to a reduction in the transmission probability, the transmission probability shifted back. This behavior is illustrated in Fig. 33. The results from the two methods show consistent trends.

Furthermore, the turning point for the WKB approximation with l=2 is between 0.17 and 0.18, whereas the strict bound method predicts the turning point to be between 0.3 and 0.4. Although there is a difference in the exact turning points, both methods show the same overall behavior of the greybody factor, demonstrating their suitability in the characteristics of the even-parity vector mode.

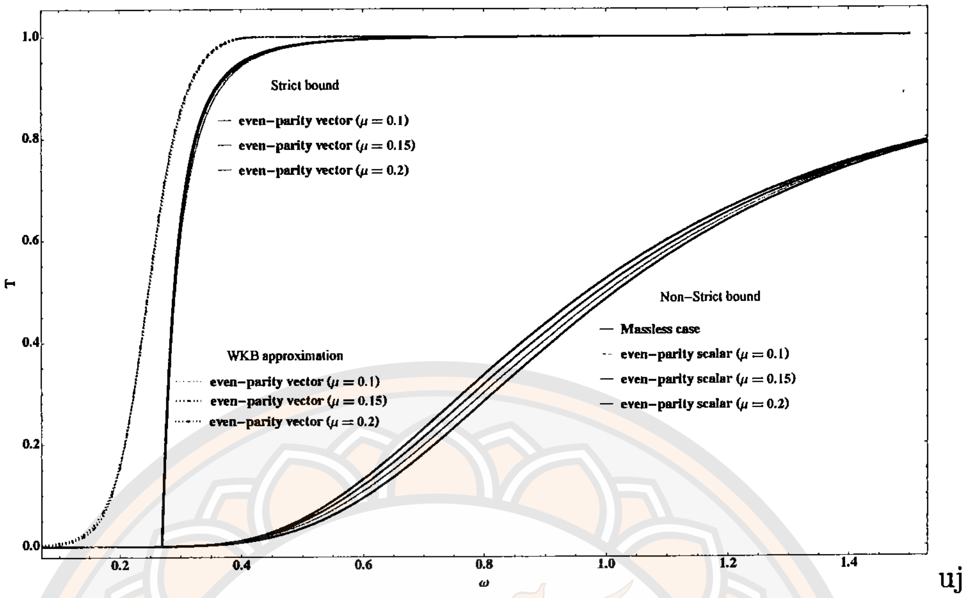

Figure 33 **a comparison between the WKB and rigorous bound for even-parity vector mode when $l = 2$. The dashed lines represent the result of the WKB approximation, and the solid lines represent the result of the rigorous bound.**

7.2 Conclusion

In this study, we investigate the perturbation of a spin-1 vector field (Proca field) in the spacetime of a Schwarzschild black hole and analyze the behavior of the greybody factor associated with the black hole. To separate the angular part of the vector potential components for Proca's field equation, we introduce a basis of four vector spherical harmonics, enabling the separation of variables in Proca's field equation into four radial equations as shown in Eqs. (4.37)-(4.40).

The solutions are represented in terms of vector spherical harmonics (VSH). These four radial equations are collectively referred to as the electric and magnetic modes. The modes of the Proca fields are categorized into odd-parity and even-parity modes. Each mode corresponds to a specific perturbative behavior.

The Proca field includes three polarization states due to its massive field nature, which describes the degrees of freedom of a massive spin-1 particle. In the spherically symmetric black hole spacetimes, these modes are further categorized into odd-parity and even-parity vector/scalar modes.

The radial equations of even-parity modes for the traditional separation method, VSH one, are coupled. However, it can be decoupled with a specific technique as presented in the main contents and supplemented by the Lorenz condition known as the monopole modes. We then focus on this decoupled equation for the special case of the monopole mode ($l = 0$, even parity), leading to the radial equation for the monopole case, as shown in Eq. (5.6).

An alternative method for separation is the Frolov-Krtous-Kubizňák-Santos (FKKS) method, which separates and decouples the equations of motion of the Proca field in Kerr-like spacetimes and further applies to the Schwarzschild black hole in the non-rotating and charge-less limit. This approach introduces a new form of radial equations, as presented in Eq. (4.62). We verified the consistency and decoupled the three radial even-parity equations into a single radial equation, as presented in Eq. (4.62), this process allowed us to identify a complete study for the Proca field in Schwarzschild black hole.

The odd-parity mode corresponds to the Regge-Wheeler-vector equation, while the even-parity scalar mode reduces to the Regge-Wheeler-scalar equation in the massless limit as discussed in Ch. 6. For the even-parity vector modes, the mathematical formula of the radial equation can not reduce to the Regge-Wheeler form in the massless limit, however, the isospectral is still confirmed to be true when we obtained the greybody factor as presented in Ch. 6.2.2.

For the behavior of the greybody factor of the Proca field, as the Proca mass increases, the transmission probability decreases. This behavior is consistent with all modes presented in this thesis, except for the even-parity vector mode, which shows an opposite trend in the small mass area. However, it is observed that when

Proca mass increases beyond a certain mass, the transmission probability shifts to the right. indicating a decrease in transmission probability. It is worth noting that all of our greybody results follow the shape of effective potential as we expected.

The resulting greybody factor from the rigorous strict bound works better than the non-strict bounds in general, which provides a result comparable to the WKB approximation. On the other hand, the non-strict bound works less accurately for either mode, especially the even-parity scalar mode. The behavior of the greybody factor from this bound differs significantly from that obtained by using the strict bound and the WKB approximation.

The WKB approximations were not in the same procedure when dealing with each mode of the Proca perturbation. For the odd parity mode, the traditional WKB procedure was natural to apply. For the even-parity scalar mode, the series expansions around $\mu \to 0$ for the effective potential and the $r_{\max}$ were required to achieve the greybody factor. For the even-parity vector mode, the standard procedure may not be applicable because the effective potential for the even-parity vector depends on both the mass "μ" and energy "ω" of the Proca field, and cannot approximate to some well-studied form in the massless limit. Therefore, in this case, we need to fix the energy "ω" to compute $r_{\max}$, then the evaluation greybody factor can be performed point by point.

Lastly, to conclude the thesis, our works sufficiently reproduce the numerical results presented in [8] through a semi-analytical treatment, and the new beneficial outcomes are mainly twofold. Firstly we found that the greybody factor for the even-parity vector polarization includes the highest transmission probability for a given energy of the Proca particles, which is even higher than the Maxwell particles (massless spin-1) in the small mass area. Secondly, the even-parity scalar polarization isospectral with the scalar perturbation in the massless limit. With a fixing and non-vanishing particle mass, the greybody factor for the Proca particle with even-parity scalar polarization includes a lower transmission probability than the massive scalar particles. These results provide insights for a further investigations into the greybody factor of the Proca field in Kerr-like or modified gravity black hole spacetimes, as well as the future possible experiments on the study of Hawking radiation.

REFERENCES

REFERENCES

1. Schwarzschild K. Über das Gravitationsfeld eines Massenpunktes nach der Einsteinschen Theorie. *Sitzungsber Königl Preuss Akad Wiss.* 1916 Jan:189–96.

2. Nordström G. On the energy of the gravitation field in Einstein's theory. *Kon Ned Akad Wet Proc Ser B Phys Sci.* 1918 Jan;20:1238–45.

3. Kerr RP. Gravitational field of a spinning mass as an example of algebraically special metrics. *Phys Rev Lett.* 1963;11:237–8.

4. Newman ET, Couch R, Chinnapared K, Exton A, Prakash A, Torrence R. Metric of a rotating, charged mass. *J Math Phys.* 1965;6:918–9.

5. Regge T, Wheeler JA. Stability of a Schwarzschild singularity. *Phys Rev.* 1957 Nov;108:1063–9.

6. Hawking SW. Particle creation by black holes. *Commun Math Phys.* 1975;43:199–220. Erratum in: *Commun Math Phys.* 1976;46:206.

7. Konoplya RA. Massive vector field perturbations in the Schwarzschild background: Stability and quasinormal spectrum. *Phys Rev D.* 2006 Jan;73(2). `https://doi.org/10.1103/PhysRevD.73.024009`

8. Herdeiro C, Sampaio MOP, Wang M. Hawking radiation for a Proca field in D dimensions. *Phys Rev D.* 2012 Jan;85:024005. `https://doi.org/10.1103/PhysRevD.85.024005`

9. Rosa JG, Dolan SR. Massive vector fields on the Schwarzschild spacetime: Quasinormal modes and bound states. *Phys Rev D.* 2012 Feb;85(4). `https://doi.org/10.1103/PhysRevD.85.044043`

10. Frolov VP, Krtouš P, Kubizňák D. Separation of variables in Maxwell equations in Plebański-Demiański spacetime. *Phys Rev D.* 2018 May;97(10). `https://doi.org/10.1103/PhysRevD.97.101701`

11. Frolov VP, Krtouš P, Kubizňák D, Santos JE. Massive vector fields in rotating black-hole spacetimes: Separability and quasinormal modes. *Phys Rev Lett.* 2018;120(23):231103.

12. Percival J, Dolan SR. Quasinormal modes of massive vector fields on the Kerr spacetime. *Phys Rev D.* 2020 Nov;102(10). `https://doi.org/10.1103/PhysRevD.102.104055`

13. Fernandes TV, Hilditch D, Lemos JPS, Cardoso V. Quasinormal modes of Proca fields in a Schwarzschild-AdS spacetime. *Phys Rev D.* 2022 Feb;105:044017. `https://doi.org/10.1103/PhysRevD.105.044017`

14. Boonserm P, Visser M. Bounding the greybody factors for Schwarzschild black holes. *Phys Rev D.* 2008 Nov;78(10). `https://doi.org/10.1103/PhysRevD.78.101502`

15. Iyer S, Will CM. Black-hole normal modes: A WKB approach. I. Foundations and application of a higher-order WKB analysis of potential-barrier scattering. *Phys Rev D.* 1987 Jun;35:3621–31. `https://doi.org/10.1103/PhysRevD.35.3621`

16. Will CM, Guinn JW. Tunneling near the peaks of potential barriers: Consequences of higher-order Wentzel-Kramers-Brillouin corrections. *Phys Rev A.* 1988 May;37:3674–9. `https://doi.org/10.1103/PhysRevA.37.3674`

17. Boonserm P, Ngampitipan T, Visser M. Bounding the greybody factors for scalar excitations of the Kerr-Newman spacetime. *J High Energy Phys.* 2014 Jan;2014.

18. Boonserm P, Phalungsongsathit S, Sansuk K, Wongjun P. Greybody factors for massive scalar field emitted from black holes in dRGT massive gravity. *Eur Phys J C.* 2023 Jul;83(7). `https://doi.org/10.1140/epjc/s10052-023-11843-x`

19. Boonserm P, Ngampitipan T, Wongjun P. Greybody factor for black string in dRGT massive gravity. *Eur Phys J C.* 2019;79(4):330.

20. Barman S. The Hawking effect and the bounds on greybody factor for higher dimensional Schwarzschild black holes. *Eur Phys J C.* 2020;80(1):50.

21. Boonserm P, Chen CH, Ngampitipan T, Wongjun P. Greybody factor for massive fermion emitted by a black hole in de Rham–Gabadadze–Tolley massive gravity theory. *Phys Rev D.* 2021 Oct;104:084054. `https://doi.org/10.1103/PhysRevD.104.084054`

22. Bunjusuwan S, Chen CH. The greybody factor for the monopole and odd-parity modes of the Proca field in the Schwarzschild black hole spacetimes. *J Phys Conf Ser.* 2023;2653(1):012022.

23. Konoplya RA, Zinhailo AF. Hawking radiation of non-Schwarzschild black holes in higher derivative gravity: A crucial role of greybody factors. *Phys Rev D.* 2019;99(10):104060.

24. Konoplya RA, Zhidenko A, Zinhailo AF. Higher order WKB formula for quasinormal modes and greybody factors: Recipes for quick and accurate calculations. *Class Quantum Grav.* 2019;36:155002.

25. Konoplya RA. Quasinormal behavior of the dimensional Schwarzschild black hole and the higher order WKB approach. *Phys Rev D.* 2003 Jul;68(2). `https://doi.org/10.1103/PhysRevD.68.024018`

26. Schrödinger E. An undulatory theory of the mechanics of atoms and molecules. *Phys Rev.* 1926 Dec;28:1049–70. `https://doi.org/10.1103/PhysRev.28.1049`

27. Cohen-Tannoudji C, Diu B, Laloë F. *Quantum mechanics.* 1st ed. New York, NY: Wiley; 1977. Trans. of: Mécanique quantique. Paris: Hermann, 1973. `https://cds.cern.ch/record/101367`

28. Visser M. Some general bounds for one-dimensional scattering. *Phys Rev A.* 1999 Jan;59:427–38. `https://doi.org/10.1103/PhysRevA.59.427`

29. Boonserm P. Rigorous bounds on transmission, reflection, and Bogoliubov coefficients. 2009. `https://arxiv.org/abs/0907.0045`

30. Hawking SW. Particle creation by black holes. *Commun Math Phys.* 1975 Aug;43(3):199–220.

31. Frolov VP, Krtouš P, Kubizňák D, Santos JE. Massive vector fields in rotating black-hole spacetimes: Separability and quasinormal modes. *Phys Rev Lett.* 2018 Jun;120(23). `https://doi.org/10.1103/PhysRevLett.120.231103`

APPENDIX

APPENDIX A REPRODUCE THE RADIAL EQUATION

In this appendix, we derive the radial equations for a Proca field in a spherically symmetric spacetime. We begin by considering the expression

A.1 For the case $\nu = r$

For the case $\nu = r$, we follow a similar process as the previous case and the first two terms become,

$$\begin{aligned}
\nabla_\mu \nabla^\mu A^r - \mu^2 A^r \;=\;& g^{tt}\Big[\partial_t^2 A^r + \partial_t({\Gamma^t}_{rr} A^t) - {\Gamma^r}_{tt}\partial_r A^r - {\Gamma^r}_{tt}{\Gamma^r}_{rr} A^r \\
& +{\Gamma^r}_{tt}\partial_t A^t + {\Gamma^r}_{tt}{\Gamma^t}_{tr} A^r\Big] \\
& +g^{rr}\Big[\partial_r^2 A^r + \partial_r(\Gamma^r_{rr} A^r) - \Gamma^r_{rr}\partial_r A^r - \Gamma^r_{rr}\Gamma^r_{rr} A^r \\
& +\Gamma^r_{rr}\partial_r A^r + \Gamma^r_{rr}\Gamma^r_{rr} A^r\Big] \\
& +g^{\theta\theta}\Big[\partial_\theta^2 A^r + \partial_\theta({\Gamma^t}_{\theta\theta} A^\theta) - {\Gamma^t}_{\theta\theta}\partial_r A^r - {\Gamma^r}_{\theta\theta}{\Gamma^r}_{rr} A^r \\
& +{\Gamma^r}_{\theta\theta}\partial_\theta A^\theta + {\Gamma^t}_{\theta\theta}{\Gamma^\theta}_{\theta t} A^t\Big] \\
& +g^{\phi\phi}\Big[\partial_\phi^2 A^t + \partial_\phi({\Gamma^t}_{\phi\phi} A^\phi) - {\Gamma^t}_{\phi\phi}\partial_r A^r - {\Gamma^\theta}_{\phi\phi}\partial_\theta A^r \\
& -{\Gamma^r}_{\phi\phi}{\Gamma^r}_{rr} A^r - {\Gamma^\theta}_{\phi\phi}{\Gamma^r}_{\theta\theta} A^\theta + {\Gamma^r}_{\phi\phi}\partial_\phi A^\phi \\
& +{\Gamma^r}_{\phi\phi}{\Gamma^\phi}_{rr} A^r + {\Gamma^r}_{\phi\phi}{\Gamma^\phi}_{\phi\theta} A^\theta - \mu^2 A^r\Big].
\end{aligned} \tag{A.1}$$

Replace the value of the Christoffel symbols and simplify the equation as written above, we obtain

$$\begin{aligned}
\nabla_\mu \nabla^\mu A^r - \mu^2 A^r \;=\;& -f'\partial_t A^t - \left(\frac{\partial_t^2}{f} - \frac{f'}{2}\partial_t + \frac{1}{2}\frac{f'^2}{f}\right) A^t \\
& + \left(f\partial_t^2 - \frac{1}{2}f'' + \frac{1}{2}f'' - \frac{1}{2}f'\partial_r\right) A^r \\
& + \left(\frac{\partial_\theta^2}{r^2} + \frac{f}{r}\partial_r - \frac{1}{2}\frac{f'}{r} - \frac{f}{r^2}\right) A^r - \frac{2}{r} f\partial_\theta A^\theta \\
& + \left(\frac{\partial_\phi^2}{r^2} + \frac{f}{r}\partial_r + \frac{cos\theta}{r^2 \sin\theta}\partial_r - \frac{f'}{2r} - \frac{f}{r^2}\right) A^t \\
& - \frac{2\cos\theta f}{r\sin\theta} A^\theta - \frac{2}{r} f\partial_\phi A^\phi - \mu^2 A^r.
\end{aligned} \tag{A.2}$$

To separate the angular part of the vector potential components, we decompose the vector potential $\left(A^{\theta}, A^{\phi}\right)$ by using Eq.(4.25),(4.26) and the spherical harmonics Eq.(4.30), we obtain

$$\begin{aligned}\nabla_{\mu}\nabla^{\mu}A^{r}-\mu^{2}A^{r} &= -f'\partial_{t}A^{t}-(\frac{\partial_{t}^{2}}{f}-\frac{f'}{2}\partial_{r}+\frac{1}{2}\frac{f'^{2}}{f}-f\partial_{1}^{2}+\frac{1}{2}f'' \\ &\quad -\frac{1}{2}\frac{f'}{f}+\frac{1}{2}f'\partial_{r}-\frac{\partial_{\theta}^{2}}{r^{2}}-\frac{f}{r}\partial_{1}+\frac{1}{2}\frac{f'}{r}+\frac{f}{r^{2}}-\frac{\partial_{3}^{2}}{r^{2}\sin^{2}\theta} \\ &\quad -\frac{f}{r}\partial_{t}-\frac{\cos\theta}{r^{2}\sin\theta}\partial_{\theta}+\frac{f'}{2r}+\frac{f}{r^{2}})A^{r}+\frac{2f}{r^{3}}u_{(3)}^{lm}Y^{lm} \\ &\quad -\mu^{2}A^{r}. \end{aligned} \tag{A.3}$$

We next consider A^{t} and A^{r} in Eq.(4.23),(4.24), together with the Ricci tensor we obtain

$$\begin{aligned}\nabla_{\mu}\nabla^{\mu}A^{r}-\mu^{2}A^{r}-R_{r}^{r}A^{r} &= -(\frac{\partial_{t}^{2}}{f}-f\partial_{r}^{2}-\frac{2f}{r}\partial_{r}+\frac{f''}{2}+\frac{f'}{r}+\frac{2f}{r^{2}})\frac{u_{(2)}^{lm}Y^{lm}}{r} \\ &\quad +\frac{f'}{rf}(\partial_{t}u_{r})Y^{lm}-\frac{l(l+1)}{r^{3}}u_{(2)}^{lm}Y^{lm}+\frac{2f}{r^{3}}u_{(3)}^{lm}Y^{Aqlm} \\ &\quad -\frac{\mu^{2}}{r}u_{(2)}^{lm}Y^{lm}-R_{r}^{r}A^{r}=0. \end{aligned} \tag{A.4}$$

We may obtain the Ricci tensor $R_{r}^{r}A^{r}$ as

$$\begin{aligned} R^{r}{}_{r}A^{r} &= g^{rr}R_{rr}A^{r} \\ &= f(-\frac{1}{f}(\frac{f''}{2}+\frac{f'}{rf}))\frac{1}{r}u_{(2)}^{lm}Y^{lm}. \end{aligned} \tag{A.5}$$

Then,

$$\begin{aligned}\nabla_{\mu}\nabla^{\mu}A^{r}-\mu^{2}A^{r}-R_{r}^{r}A^{r} &= -(\frac{\partial_{t}^{2}}{f}+\frac{f''}{2}+\frac{f'}{r}+\frac{2f}{r^{2}})\frac{1}{r}u_{(2)}^{lm}+\frac{f}{r}\partial_{r}^{2}u_{(2)}^{lm}-\frac{l(l+1)}{r^{3}}u_{(2)}^{lm} \\ &\quad +\frac{f'}{rf}(\partial_{t}u_{(1)}^{lm})+\frac{2f}{r^{3}}u_{(3)}^{lm}-\frac{\mu^{2}}{r}u_{(2)}^{lm}+f(-(\frac{f''}{2}+\frac{f'}{r})\frac{1}{r}u_{(2)}^{lm}Y^{lm} \\ &= 0. \end{aligned} \tag{A.6}$$

We simplify the equation by multiplying with rf

$$\begin{aligned} &f'(\partial_{t}u_{(1)}^{lm}))-(\partial_{t}^{2}+\frac{ff''}{2}+\frac{f'f}{r}+\frac{2f^{2}}{r^{2}})u_{(2)}^{lm}+f^{2}\partial_{r}^{2}u_{(2)}^{lm} \\ &-\frac{fl(l+1)}{r^{2}}u_{(2)}^{lm}-\frac{2f^{2}}{r^{2}}u_{(3)}^{lm}-\mu^{2}fu^{2}+(\frac{ff''}{2}+\frac{ff'}{rf})u_{(2)}^{lm}=0. \end{aligned} \tag{A.7}$$

The radial equation for $v = t$ yield

$$[-\partial_t^2 + \partial_{r*}^2 - f[\frac{l(l+1)}{r^2} + \mu^2]]u_{(2)}^{lm} + \partial_r f\,(\dot{u}_1 - u_2') - \frac{2}{r^2}f^2(u_{(2)}^{lm} - u_{(3)}^{lm}) = 0 \quad \text{(A.8)}$$

A.2 For the case $\nu = \theta$ and $\nu = \phi$

Similarly, for the angular components (A^θ) and (A^ϕ), we write

$$\begin{aligned}
\nabla_\mu\nabla^\mu A^\theta - \mu^2 A^\theta - R_\theta^\theta A^\theta &= \frac{-\partial_t^2 A^\theta}{f} + f'\partial_r A^\theta + f\partial_r^2 A^\theta + \frac{4f}{r}\partial_r A^\theta \\
&\quad + \frac{1}{r^2}\partial_\theta^2 A^\theta + \frac{\cot\theta}{r^2}\partial_\theta A^\theta + \frac{1}{r^2\sin^2\theta}\partial_\phi^2 A^\theta + \frac{2}{r^3}\partial_\theta A^r \\
&\quad - \frac{2\cot\theta}{r^3}\partial_\phi A^\phi - \frac{\cot^2\theta}{r^2}A^\theta + \frac{f'}{f}A^\theta \\
&\quad - \mu A^\theta + \frac{f}{r^2}A^\theta - R_\theta^\theta A^\theta - \mu^2 A^\theta = 0, \qquad \text{(A.9)} \\
\nabla_\mu\nabla^\mu A^\phi - \mu^2 A^\phi - R_\phi^\phi A^\phi &= -\frac{\partial_t^2 A^\phi}{f} + f'\partial_r A^\phi + \frac{f'}{f}A^\phi + f\partial_r^2 A^\phi + \frac{4f}{r}\partial_r A^\phi \\
&\quad + \frac{f}{r^2}A^\phi + \frac{\cot\theta}{r^2}\partial_\theta A^\phi + \frac{2}{r^2\sin^2\theta}\partial_\phi A^r + \frac{2\cot\theta}{r^2\sin^2\theta}\partial_\phi A^r \\
&\quad + \frac{1}{r^2}\partial_2^2 A^\phi + \frac{1}{r^3\sin^2\theta}\partial_\phi^2 A^\phi - \frac{1}{r^2}A^\phi \\
&\quad - R_\phi^\phi A^\phi - \mu^2 A^\phi + \frac{2\cot\theta}{r^2}\partial_\theta A^\phi = 0. \qquad \text{(A.10)}
\end{aligned}$$

For decompose case $\nu = \theta$ and $\nu = \phi$ we assume the combination

$$(\partial_\theta + \cot\theta) \times (\nu = \theta) + \partial_\phi(\nu = \phi) = 0. \qquad \text{(A.11)}$$

For simplicity of calculation, we divided it into four parts, where the first parts

$$\begin{aligned}
&(\partial_\theta + \cot\theta)(\frac{-\partial_t^2 A^\theta}{f} + f'\partial_r A^\theta + \frac{f'}{r}A^\theta + f\partial_r^2 A^\theta + \frac{4}{r}f\partial_r A^\theta + \frac{fA^\theta}{r^2} - \mu^2 A^\theta) \\
&+\partial_\phi(-\frac{\partial_t^2 A^\phi}{f} + f'\partial_1 A^\phi + \frac{f'}{r}A^\phi + f\partial_r^2 A^\theta + \frac{4f}{r}\partial_r A^\phi + \frac{f}{r^2}A^\phi - \mu^2 A^\phi) \\
&= \left(\frac{-\partial_t^2}{f} + f'\partial_r + f'\partial_r + \frac{f'}{r} + f\partial_r^2 + \frac{4f\partial_r}{r} + \frac{f}{r^2} - \mu^2\right)((\partial_t + \cot\theta)A^\theta + \partial_\phi A^\phi) \\
&= -\left(\frac{-\partial_\theta^2}{f} + f'\partial_r + f'\partial_r + \frac{f'}{r} + f\partial_r^2 + \frac{4f\partial_r}{r} + \frac{f}{r^2} - \mu^2\right)\frac{u_{(3)}^{lm}}{r^2}Y^{lm} \\
&= \left[\frac{-\partial_t^2}{r^2 f} + \frac{f}{r^2}\partial_r^2 + \frac{f'}{r^2}\partial_r - \frac{f'}{r^3} - \frac{f}{r^4} - \frac{\mu^2}{r^2}\right]u_{(3)}^{lm}Y^{lm}. \qquad \text{(A.12)}
\end{aligned}$$

The second part is

$$
\begin{aligned}
&(\partial_\theta + \cot\theta)\left(\frac{1}{r^2}\partial_\theta^2 + \frac{\cot\theta}{r^2}\partial_\theta + \frac{1}{r^2\sin^2\theta}\partial_\phi^2\right)A^\theta \\
&\quad +\partial_\phi\left(\frac{1}{r^2}\partial_\theta^2 + \frac{\cot\theta}{r^2}\partial_\theta + \frac{1}{r^2\sin^2\theta}\partial_\phi^2\right)A^\theta \\
&= \left(\frac{1}{r^2}\partial_\theta^2 + \frac{\cot\theta}{r^2}\partial_\theta + \frac{1}{r^2\sin^2\theta}\partial_\phi^2\right)\left[(\partial_\theta + \cot\theta)\,A^\theta + \partial_\phi A^\phi\right] \\
&\quad + \left[\frac{1}{r^2\sin^2\theta}\partial_\theta - \frac{\cot\theta}{r^2\sin^2\theta} - \frac{2\cos\theta}{r^2\sin^3\theta}\partial_\phi^2\right]A^\theta \\
&= \frac{l(l+1)}{r^4}u_{(3)}^{lm}Y^{lm} + \left[\frac{1}{r^2\sin^2\theta}\partial_\theta - \frac{\cot\theta}{r^2\sin^2\theta} - \frac{2\cos\theta}{r^2\sin^3\theta}\partial_\phi^2\right]A^\theta. \qquad \text{(A.13)}
\end{aligned}
$$

The third part is

$$
\begin{aligned}
&(\partial_\theta + \cot\theta)\left(\frac{2}{r^3}\partial_\theta A^r\right) + \partial_\phi\frac{2}{r^3\sin^2\theta}\partial_\phi A^r \\
&= \frac{2}{r^3}\left(\partial_\theta^2 + \cot\theta\partial_\theta + \frac{1}{\sin^2\theta}\partial_\phi^2\right)\left(\frac{u_2Y^{lm}}{r}\right) \\
&\qquad = \frac{2}{r^4}\left(-l(l+1)u_2Y^{lm}\right). \qquad \text{(A.14)}
\end{aligned}
$$

The fourth term is

$$
\begin{aligned}
&(\partial_\theta + \cot\theta)\Big(\tfrac{1}{r^2}\partial_\theta^2 + \tfrac{\cot\theta}{r^2}\partial_\theta + \tfrac{1}{r^2\sin^2\theta}\partial_\phi^2\Big)A^\theta \\
&\quad + \partial_\phi\Big(\tfrac{1}{r^2}\partial_\theta^2 + \tfrac{\cot\theta}{r^2}\partial_\theta + \tfrac{1}{r^2\sin^2\theta}\partial_\phi^2\Big)A^\theta \\
&\quad = \Big(\tfrac{1}{r^2}\partial_\theta^2 + \tfrac{\cot\theta}{r^2}\partial_\theta + \tfrac{1}{r^2\sin^2\theta}\partial_\phi^2\Big)\Big[(\partial_\theta + \cot\theta)A^\theta + \partial_\phi A^\phi\Big] \\
&\quad + \Big[\tfrac{1}{r^2\sin^2\theta}\partial_\theta - \tfrac{\cot\theta}{r^2\sin^2\theta} - \tfrac{2\cos\theta}{r^2\sin^3\theta}\partial_\phi^2\Big]A^\theta \\
&\quad = \tfrac{l(l+1)}{r^4}\,u_{(3)}^{lm}\,Y^{lm} + \Big[\tfrac{1}{r^2\sin^2\theta}\partial_\theta - \tfrac{\cot\theta}{r^2\sin^2\theta} - \tfrac{2\cos\theta}{r^2\sin^3\theta}\partial_\phi^2\Big]A^\theta. \qquad \text{(A.15)}
\end{aligned}
$$

We consider the fourth with the final term (Ricci tensor parts)

$$
\begin{aligned}
& (\partial_\theta + \cot\theta)\,(-R_2^2A^\theta) + \partial_\phi(-R_3^3A^\phi) \\
= \;& -\Big[(\partial_\theta + cot\theta)\left(\frac{-r' - f + 1}{r^4l(l+1)}\right) \times \left(u_{(3)}^{lm}\partial_\phi - \frac{u_{(4)}^{lm}}{\sin\theta}\partial_\phi\right)Y^{lm}\Big] \\
& -\Big[\partial_\phi\left(\frac{-rf' - f + 1}{r^4\sin^4\theta l(l+1)}\right) \times \sin^2\theta\left(u_{(3)}^{lm}\partial_\phi - u_{(4)}^{lm}\sin\theta\partial_\theta\right)Y^{lm}\Big] \\
= \;& -\left(\frac{-rf' - f + 1}{r^2l(l+1)}\right)\left(\frac{\partial_\phi^2}{r^2} + \frac{\cot\theta\partial_\theta}{r^2} + \frac{\partial_\phi^2}{r^2}\right)Y^{lm} \\
= \;& -\frac{1}{r^2}\left(\frac{rf' + f - 1}{r^2}\right)u^3Y^{lm}. \qquad \text{(A.16)}
\end{aligned}
$$

Now we sum for every parts Eq.(A.12)+Eq. (A.13)+Eq. (A.14)+Eq. (A.15)+Eq. (A.16), we obtain

$$\left[\frac{\partial_t^2}{r^2 f} - \frac{f}{r^2}\partial_r^2 - \frac{f'}{r^2}\partial_r + \frac{\mu^2}{r^2}\right] u_{(3)}^{lm} Y^{lm} + \frac{l(l+1)}{r^4} u_{(3)}^{lm} Y^{lm} - \frac{2}{r^4}\left[l(l+1)\right] u_{(2)}^{lm} Y^{lm}$$
$$\cancel{+\left[\frac{f'}{r^3} + \frac{f}{r^4} - \frac{1}{r^4}\right] u_{(3)}^{lm} Y^{lm}} \cancel{- \frac{1}{r^2}\left(\frac{rf' + f - 1}{r^2}\right) u^3 Y^{lm}} = \quad 0.$$

Finally, we may obtain

$$\left[-\partial_t^2 + \partial_{r*}^2 - f\left(\frac{l(l+1)}{r^2} + \mu^2\right)\right] u_{(3)}^{lm} + \frac{2f}{r^2} l(l+1) u_{(2)}^{lm} = 0. \qquad \text{(A.17)}$$

For the case $\nu = \phi$, it is simillar with $\nu = \theta$, we assume the combination

$$(2\cos\theta + \sin\theta\partial_\theta) \times (\nu = \phi) - \frac{1}{\sin\theta}\partial_\phi \times (\nu = \theta) = 0. \qquad \text{(A.18)}$$

For simplicity of calculation, we divided it into four parts, for first parts is

$$(2\cos\theta + \sin\theta\partial_\theta)\left(\frac{-\partial_t^2 A^\phi}{f} + f'\partial_t A^\phi + \frac{f'}{r}A^\phi + f\partial_r^\phi A^\phi + \frac{4}{r} f\partial_r A^\phi + \frac{fA^\phi}{r^2} - \mu^2 A^\phi\right)$$
$$- \left(\frac{1}{\sin\theta}\partial_\theta\right)\left(-\frac{\partial_t^2 A^\theta}{f} + f'\partial_r A^\theta + \frac{f'}{f}A^\phi + f\partial_r^2 A^\theta + \frac{4f}{r}\partial_r A^\theta + \frac{f}{r^3}A^\theta - \mu^2 A^\theta\right)$$
$$= \left(\frac{-\partial_0^2}{f} + f'\partial_r + f'\partial_r + \frac{f'}{r} + f\partial_r^2 + \frac{4f\partial_r}{r} + \frac{f}{r^2} - \mu^2\right)$$
$$\times \left((2\cos\theta + \sin\theta\partial_\phi) A^\phi - \frac{1}{\sin\theta}\partial_\phi A^\theta\right)$$
$$= \left[\frac{-\partial_0^2}{r^2 f} + \frac{f}{r^2}\partial_r^2 + \frac{f'}{r^2}\partial_r - \frac{f'}{r^3} - \frac{f}{r^4} - \frac{\mu^2}{r^2}\right] u_{(4)}^{lm} Y^{lm}, \qquad \text{(A.19)}$$

for second parts is

$$(\partial_\theta + \cot\theta)\left(\frac{1}{r^2}\partial_\theta^2 + \frac{\cot\theta}{r^2}\partial_\theta + \frac{1}{r^2\sin^2\theta}\partial_\phi^2\right) A^\theta$$
$$+ \partial_\phi\left(\frac{1}{r^2}\partial_\theta^2 + \frac{\cot\theta}{r^2}\partial_\theta + \frac{1}{r^2\sin^2\theta}\partial_\phi^2\right) A^\theta$$
$$= \left(\frac{1}{r^2}\partial_\theta^2 + \frac{\cot\theta}{r^2}\partial_\theta + \frac{1}{r^2\sin^2\theta}\partial_\theta^2\right)\left((\partial_\theta + cot\theta) A^\theta + \partial_\phi A^\phi\right)$$
$$+ \left(\frac{1}{r^2\sin^2\theta}\partial_\theta - \frac{\cot\theta}{r^2\sin^2\theta} - \frac{2\cos\theta}{r^2\sin^3\theta}\partial_\phi^2\right) A^\theta$$
$$= \frac{l(l+1)}{r^4} u_{(3)}^{lm} Y^{lm} + \left(\frac{1}{r^2\sin^2\theta}\partial_\theta - \frac{\cot\theta}{r^2\sin^2\theta} - \frac{2\cos\theta}{r^2\sin^3\theta}\partial_\phi^2\right) A^\theta.$$

(A.20)

For the third part, we consider together with Eq. (A.20)

$$
\begin{aligned}
&(2\cos\theta+\sin\theta\partial_\theta)\left(\frac{2\cot\theta}{r^2\sin^2\theta}\partial_\phi A^\theta+\frac{2\cot\theta}{r^2}\partial_\theta A^\phi-\frac{1}{r^2}A^\phi\right)\\
&+\left(\frac{1}{\sin\theta}\right)\partial_\phi\left(\frac{2\cot\theta}{r^2}\partial_\phi A^\phi+\frac{\cot^2}{r^2}\partial_\phi A^\phi+\frac{\cot^2\theta}{r^2}A^\theta\right)\\
&+\frac{1}{r^2}\left[4\cos\theta+\left(5\sin\theta-\frac{1}{\sin\theta}-\cot\theta\cos\theta\right)\partial_\theta-2\cos\theta\partial^2-\frac{2\cot\theta}{\sin\theta}\partial_\phi^2\right]A^\phi\\
&+\frac{1}{r^2}\left[\frac{1}{\sin^3\theta}\partial_\phi-\frac{2\cos\theta}{\sin^2\theta}\partial_\theta\partial_\phi\right]A^\theta-\frac{u^{lm}_{(4)}}{r^4}l(l+1)Y^{lm}\\
&=\frac{u^{lm}_{(4)}}{r^4}Y^{lm}-\frac{u^{lm}_{(4)}}{r^4}l(l+1)Y^{lm}.
\end{aligned}
\tag{A.21}
$$

For the final parts (Ricci tensor parts), it reads

$$
-(2\cos\theta+\sin\theta\partial_\theta)\left({R^\phi}_\phi A^\phi\right)+\frac{1}{\sin\theta}\partial_\phi\left({R^\theta}_\theta A^\theta\right)=\left(\frac{f'}{r^3}+\frac{f}{r^4}-\frac{1}{r^4}\right)u^{lm}_{(4)}Y^{lm}
\tag{A.22}
$$

We sum every parts Eq. (A.19)+Eq.(A.20). Thus, we obtain

$$
\begin{aligned}
&\left[\frac{-\partial_0^2}{r^2 f}+\frac{f}{r^2}\partial_r^2+\frac{f'}{r^2}\partial_r-\frac{f'}{r^3}-\frac{f}{r^4}-\frac{\mu^2}{r^2}\right]u^{lm}_{(4)}Y^{lm}+\frac{u^{lm}_{(4)}}{r^4}Y^{lm}\\
&\qquad-\frac{u^{lm}_{(4)}}{r^4}l(l+1)Y^{lm}+\left(\frac{f'}{r^3}+\frac{f}{r^4}-\frac{1}{r^4}\right)u^{lm}_{(4)}Y^{lm}=0,
\end{aligned}
\tag{A.23}
$$

This can be simplified by multiplying with $\frac{r^2 f}{Y^{lm}}$

$$
\left[-\partial_t^2+\partial_{r*}^2-f\left(\frac{l(l+1)}{r^2}+\mu^2\right)\right]u^{lm}_{(4)}=0.
\tag{A.24}
$$

Collecting all contributions, one arrives at the following radial equations for the Proca field

$$
\hat{\mathcal{D}}u^{lm}_{(1)}+f'(\dot{u}^{lm}_{(2)}-\partial_{r_*}u^{lm}_{(1)})=0,
\tag{A.25}
$$

$$
\hat{\mathcal{D}}u^{lm}_{(2)}+f'\left(\dot{u}_1-\partial_{r_*}u^{lm}_{(2)}\right)-\frac{2f^2}{r^2}\left(u^{lm}_{(2)}-u^{lm}_{(3)}\right)=0,
\tag{A.26}
$$

$$
\hat{\mathcal{D}}u^{lm}_{(3)}+\frac{2f}{r^2}l(l+1)u^{lm}_{(2)}=0,
\tag{A.27}
$$

$$
\hat{\mathcal{D}}u^{lm}_{(4)}=0.
\tag{A.28}
$$

where $\hat{\mathcal{D}}=\left[-\partial_t^2+\partial_{r_*}^2-f[\frac{l(l+1)}{r^2}+\mu^2]\right]$. These four equations are the master equations that we use to compute the greybody factor in the main context.